Thesis for the degree
Doctor of Philosophy

עבודת גמר (תזה) לתואר
דוקטור לפילוסופיה

Submitted to the Scientific Council of the
Weizmann Institute of Science
Rehovot, Israel

מוגשת למועצה של
מכון ויצמן למדע
רחובות, ישראל

By
Inbar Zohar

מאת
עבר זוהר

חישה קוונטית של סחריר מגנטי המצוי במולקולות
Quantum sensing of molecular electron spin

Advisor:
Dr. Amit Finkler

מנחה:
ד"ר עמית פינקלר

January, 2025

טבת, ה'תשפ"ה

אהובי, כל זה בזכותך, בהשראתך ומוקדש לך.

Contents

List of Figures

Abstract

The nitrogen-vacancy (NV) center in diamond has emerged as a powerful quantum sensor capable of detecting electron spins at the atomic scale. However, utilizing the NV center to sense the complex magnetic properties of molecular spin qubits (MSQs) remains a significant challenge. Moreover, integrating the MSQ and NV center into a hybrid quantum system can be an interesting quantum technology. This thesis aims to address the challenges of magnetic sensing of single MSQs by developing innovative methods to enhance the sensitivity and coherence of NV-based sensing.

The work begins with an effort focusing on the sensing of copper phthalocyanine (CuPc), a candidate MSQ, using a novel Ramsey correlation pulse sequence. This sequence offers DC sensitivity while successfully extending the NV center's coherence time beyond $T_2{}^*$ and T_2 limits, enabling the detection of dipolar coupling to CuPc electron spins.

Numerical and experimental results highlight the sequence's superiority over traditional methods like DEER, laying the groundwork for quantum sensing of single MSQs. Furthermore, some experimental results show a prolonged coherence time exploited by correlating the pulse sequence to the carbon nuclear spin's Larmor frequency, suggesting additional uses for the pulse sequence.

The thesis also investigates the use of chirped adiabatic pulses, demonstrating their ability to enhance sensitivity and contrast in electron spin sensing. These pulses outperform conventional π pulses by leveraging their broader spectral bandwidth for more efficient spin driving, showing promise for applications in quantum sensing and quantum information processing.

Finally, a Bayesian inference framework for real-time phase estimation is implemented, improving the NV center's sensitivity to DC magnetic fields using a non-single-shot read-out sensor. Simulations reveal that adaptive sensing can reduce measurement times and increase sensitivity compared to non-adaptive methods, showcasing the potential of machine learning in quantum sensing.

Together, these advancements represent significant progress toward realizing the NV center's potential as a sensor for complex systems like MSQs. By enhancing sensitivity and coherence while addressing practical challenges, this work paves the way for future applications in hybrid quantum systems, quantum communication, and beyond.

Acknowledgments

This thesis would not have been possible without the support, guidance, and encouragement of many individuals to whom I owe my deepest gratitude.

First and foremost, I would like to express my sincere gratitude to my advisor, Dr. Amit Finkler, for your unwavering guidance, insightful feedback, and mentorship throughout this journey. Your expertise, patience, and dedication have been invaluable in shaping this work and fostering my growth as a researcher.

I am profoundly grateful to my research group members, in the past and present. Your collaboration and friendship made this experience both productive and enjoyable. Your constructive critiques, brainstorming sessions, and shared determination were crucial in overcoming challenges and achieving milestones together. Thank you, Dr. Dan Yudilevich, Dr. Jitender Kumar, Leora Schein-Lubomirsky, Ariel Smooha, Woody Rosenberg, and Asad Awadallah, for your support and teamwork.

A heartfelt thanks goes to the scientific support staff of the Departments of Chemical Research Support and Physics Core Facilities, whose technical expertise and assistance were essential to the success of this research. Your commitment to maintaining smooth operations and providing resources ensured that I could focus on my work. Thank you to Alexander Kuprienko for always solving a machinery problem with creativity and dedication; Assaf Hazzan, Leonid Tunik, Sharon Garusi, Alex Yoffe, and Dr. Ora Bitton for guidance and assistance on numerous fabrication processes and cleanroom machinery; Haim Sade and Alex Jahanfard for advising on parts design and supervising its construction; Dr. Yuri Myasoedov for advising on cryogenic systems and operations; Dr. Hagai Cohen, Dr. Tatyana Bendikov, Dr. Anna Eden Kossoy, Dr. Ifat Kaplan-Ashiri, Dr. Irit Rosenhek-Goldian, and Dr. Sidney Cohen for assistance, guidance, and operating crucial measurements for the completeness of the thesis.

To the administrative staff, Terry Debesh, Victoria Ornsthein, Sigalit Levy, Reshef Azaria, Tamir Chalaf, Amir Kronenberg and Neta Singer, thank you for your efficiency and assistance in navigating the logistical and bureaucratic aspects of this journey. Your efforts behind the scenes have not gone unnoticed and are deeply appreci-

ated.

I am also immensely thankful to my collaborators, Dr. Rainer Stöhr, Physikalisches Institut, Universität Stuttgart; Dr. Ben Haylock, Dr. Muhammad Junaid Arshad, and Prof. Cristian Bonato, School of Engineering and Physics Sciences, Heriot-Watt University; Ruolan Xue, Dr. Nikola Maksimovic and Prof. Amir Yacoby, Department of Applied Physics, Harvard University; Prof. Danna Freedman and Dr. Mikey Wojnar, Department of Chemistry, MIT; Dr. Petr Cígler, Institute of Organic Chemistry and Biochemistry, Prague, for sharing their expertise, resources, time, and perspectives. Your contributions have enriched this thesis and broadened its impact.

Finally, I owe the deepest gratitude to my family. To my spouse, Nativ, thank you for your love, understanding, patience, and unwavering belief in me, I couldn't do it without you. To my parents, your constant encouragement and support have been my foundation throughout this journey. To my brothers, your advice and perspective kept me going. To all my extended family, for believing in me and caring for me. This achievement is as much yours as it is mine.

To all who have supported me in any way during this endeavor, thank you. I hope that I have not left anyone out, and if I have, I apologize for it. It is not due to a lack of gratitude but because this journey has been long and overwhelming. This thesis would not have been possible without each of you.

Declaration

I hereby declare that this thesis summarizes my own independent research. I certify that, to the best of my knowledge and belief, this work contains no material previously published or written by another person except where due reference has been made in the text.

The following is a list of contributions by other authors:

- Dr. Dan Yudilevich, Department of Chemical and Biological Physics, WIS, constructed significant parts of the low-temperature system used in the experiment reported in Section 2.3.3 in Chapter 2 and contributed significantly to the numerical simulations code used in the simulations reported in Chapter 2.
- Dr. Jitender Kumar, Department of Chemical and Biological Physics, WIS, constructed significant parts of the low-temperature system used in the experiment reported in Section 2.3.3 in Chapter 2.
- Dr. Rainer Stöhr, Physikalisches Institut, Universität Stuttgart, fabricated the diamond membrane used in all experiments reported in this thesis under Chapters 2,3, and 4.
- Dr. Ben Haylock, Dr. Muhammad Junaid Arshad, and Prof. Cristian Bonato, School of Engineering and Physics Sciences, Heriot-Watt University, conducted the numerical simulations reported in Chapter 4.
- Ruolan Xue, Dr. Nikola Maksimovic, and Prof. Amir Yacoby, Department of Applied Physics, Harvard University, constructed significant parts of the low-temperature system used in the experiment reported in Appendix C.1.
- Dr. Hagai Cohen and Dr. Tatyana Bendikov, Department of Chemical Research Support, WIS, conducted the XPS measurements reported in Appendices C.2, A.3.
- Dr. Anna Eden Kossoy, Dr. Ifat Kaplan-Ashiri, and Dr. Sidney Cohen, Department of Chemical Research Support, WIS, assisted and conducted the XRD, SEM and AFM measurements in Chapter 2 and Appendix C.1.

- Prof. Danna Freedman and Dr. Mikey Wojnar, Department of Chemistry, MIT, Supplied and synthesized the vanadium-based molecules studied in Appendix C.2.
- Dr. Petr Cígler, Institute of Organic Chemistry and Biochemistry, Prague, Purified the molecules used in Chapter 2.

List of Abbreviations

Table 1: List of abbreviations used in the text.

AC	Alternating current	NV	Nitrogen-vacancy
DC	Direct current	ODMR	Optically detected magnetic resonance
DD	Dynamical decoupling	RT	Room-temperature
DEER	Double electron-electron resonance	RWA	Rotating-wave approximation
EPR	Electron paramagnetic resonance	SNR	Signal-to-noise ratio
T_2	Transverse relaxation time	T_1	Longitudinal relaxation time
FFT	Fast Fourier transform	T_2^*	Dephasing time
MW	Microwave	qubit	Quantum bit
MSQ	Molecular spin qubit	ISC	Inter system crossing
STM	Scanning tunneling microscopy	FPGA	Field Programmable Gate Arrays
QPE	Quantum phase estimation	APE	Adaptive phase estimation
OPX	operator-X	QUA	quantum universal assembly
DR	Dynamic range	CuPc	copper phthalocyanine
ZFS	zero field splitting	H_2PC	H_2 phthalocyanine
CPW	coplanar waveguide	DAQ	data acquisition card
IF	intermediate frequency	LO	local oscillator
RF	radio frequency	AO	analog output
DO	digital output	AI	analog input

"What we observe is not nature itself, but nature exposed to our method of questioning"

Werner Heisenberg

1 Introduction

Scientific discoveries are the reasoning of observations, which, in turn, are fruitful grounds for technological developments that improve observation methods. In this thesis work, I focus on quantum sensing as a form of observation. I use different techniques to improve an existing method of magnetic sensing to allow the possibility of observing molecular spin quantum bits (qubits) as a way to study these, in turn, as potential new devices for quantum sensing and quantum computing.

This chapter covers the background and basic principles necessary to understand the open questions addressed in this research work. The chapter is divided into four sections: Section 1.1. Quantum sensing presents an introduction to magnetic sensing and quantum sensing; Section 1.2. The nitrogen-vacancy (NV) center covers a theoretical background of the NV center as a qubit and a quantum sensor, Section 1.3. Molecular spin qubits (MSQ) give an overview of the field and the potential they hold in quantum computing; and Section 1.4. Research subjects and addressed questions connect all sections to establish the focus of the remaining chapters of this work.

1.1 Quantum sensing

The Oxford English Dictionary defines the term sensing as "The action of a machine, instrument, or similar device in detecting or measuring a circumstance, entity, etc., especially in response to a physical stimulus"[1]. In a review published in 2017, quantum sensing was defined as one of three cases. The first two of these cases can be derived from the classical definition of sensing, and the third arises from the unique nature of quantum mechanics[2]:

1. Use of quantum device to measure a physical stimulus.
2. Use of a device to measure a quantum circumstance, such as quantum coherence, in response to a physical quantity.
3. Use of quantum entanglement to improve the sensitivity or precision of a measurement.

From the definition of quantum sensing, it is clear that this field aims to study, improve, and build systems based on quantum mechanics to improve sensing abilities. As such, quantum sensing has been a major field of applications that has vastly improved since the start of the second quantum revolution[3]. Of the three definitions, only the third is based on a pure quantum effect, while the other two have some quantum effects but can also be used in classical systems.

Under the above definition, many quantum systems qualify as quantum sensors, such as solid-state spins, neutral atoms, superconducting circuits, and trapped ions. In each platform, broad research is conducted to show the superiority of quantum sensing even without implementing entanglement and quantum algorithms. For example, solid-state spins have already shown applicability as magnetometers for biology[4], chemistry[5], and solid-state physics[6], and neutral atoms have exhibited application for electric field sensing in biology[4].

For a quantum system to function as a quantum sensor, it must satisfy three fundamental criteria, as outlined in the 2017 review[2]:

1. The quantum system has discrete, resolvable energy levels.
2. The system can be initialized into a known state, and the state can be read out.
3. The system can be coherently manipulated.

A system that meets all three criteria qualifies as a quantum sensor. However, an effective quantum sensor must balance coupling to its environment with maintaining

coherence. Strong coupling enhances sensitivity to the target but also exposes the sensor to greater noise, reducing its coherence time. Conversely, long coherence times are crucial for detecting weak signals from weakly coupled targets, requiring environmental shielding to minimize noise and, consequently, interaction with the target. These competing demands make designing an optimal quantum sensor a nontrivial challenge, further complicated by additional requirements such as sensor readout, initialization, and the environmental conditions necessary for the target.

1.2 The nitrogen-vacancy center

The nitrogen-vacancy center in diamond is a well-studied quantum sensor that answers all three criteria stated above. On top of that, it has the potential to balance the coherence time and coupling to the environment while being compatible with large environment settings, such as high or low temperatures.

On the coherence aspect, compared to many quantum sensors, it is operable at a wide range of environmental temperatures[7,8,9], pressures[10,11,12], and chemical environments[13]. Its coherence time can even be prolonged when using a carefully engineered implantation of the defect's nitrogen atom or growth of the diamond and surface treatments[14,15,16]. Even though it has a long coherence time, it is still a good sensor with strong coupling to the environment due to its relatively large gyromagnetic ratio as an electronic spin. This trait allows strong coupling to magnetic fields in the first order, but also, with lower strength, it can couple to electric fields in the second order, making it a good quantum sensor to a large variety of targets[17].

The rest of this section will cover the background and physics related to the NV center. This will allow a firm ground for understanding the state-of-the-art properties of the sensor and the areas that still require improvement where scientific questions can be answered.

1.2.1 The NV center - electronic and optical properties

The NV center is a defect in the diamond lattice consisting of a nitrogen atom and a vacancy substituting two carbon atoms (Figure 1.1a). The structure's electronic configuration has a non-zero electron spin where the spin energy levels realize the quantum sensor and the electronic energy levels are used for the initialization and read-out of the sensor (criterion number 2 for a quantum sensor). This section will provide the background of the electronic structure and its use to operate the system in terms of initialization and read-out.

The NV center, as a defect in diamond, can be treated as a local molecule with a symmetry of C_{3v}. It holds three unpaired electrons from three carbon atoms and two paired electrons from the nitrogen atom of the defect. Solving the system's orbital structure while addressing the defect as a point molecule gives rise to orbital hybridization, resulting in four orbitals (a_1', a_1, e_x, e_y) [18,19]. The lowest energy orbital (a_1') is situated in the valence band of the diamond and is occupied by two electrons. Two more electrons occupy the second-lowest energy orbital (a_1), and one more electron occupies one of the degenerate orbital states (e_x, e_y), all located in the gap between the valence and conductance bands of the diamond. This electronic structure forms the neutral state of the NV center with a ground-state electron spin of $S = 1/2$ [20].

Once the defect gets negatively charged with one extra electron donated from a neighboring defect, it results in two unpaired electrons with a total spin of $S = 1$ [19,21]. The negatively charged NV^- center will be the focus of this work and will be addressed simply as NV center in the remaining text.

The orbitals of the NV center that are situated in the gap (a_1, e_x, e_y) have a strong spin-orbit coupling [22] that results in the energy diagram and the resulting optical properties of the NV. The spin-orbit coupling results with four main electronic energy levels in the diamond band gap: the ground orbital-singlet spin-triplet state $(^3A_2)$, ground orbital-singlet spin-singlet state $(^1A_1)$, ground orbital-doublet spin-singlet state $(^1E_{1,2})$ and the first excited orbital-doublet spin-triplet state (^3E), see Figure 1.1b [21,18,23].

The energy relations between all electronic states are illustrated in Figure 1.1b. A gap of 1.945 eV (637 nm) separates the ground and excited spin-triplet states. The optical emission measurement of the defect reveals a broad spectrum of emission at room temperature rising from the phonons in the lattice; the zero-phonon-line indicates the energy gap between the spin-triplet states with a local maximum at 637 nm, Figure 1.1c [18,24]. To excite the defect from the occupied ground spin-triplet state $^3A_2$ to the excited spin-triplet state ^3E, a wavelength shorter than 637 nm should be used. A wavelength of 520-532 nm, in the green wavelength regime, was found to be optimal where charge ionization of the defect is minimal [25]. Upon excitation of the defect with green light, the electron is excited to the ^3E state in a spin-conserving process. After a lifetime of ~ 10 ns, the electron will decay back to the ground state $^3A_2$ also while conserving the spin state and emitting a photon with a wavelength in the red to the near-infrared range, as illustrated in the emission graph in Figure 1.1c [26].

On top of the two triplet states, two more spin-singlet states are in the band gap (Figure 1.1b). These states can be populated through an inter-system crossing process (ISC), where an electron in the excited spin-triplet state can decay to the higher-

energy spin-singlet state $^1A_1$ through an ISC process and keep decaying in energy to the lower-energy spin-singlet $^1E_{1,2}$ and back to the ground-state spin-triplet $^3A_2$ [21]. The decay rates between each of the spin-orbit states of the NV center are presented in Figure 1.1b [27,28,29].

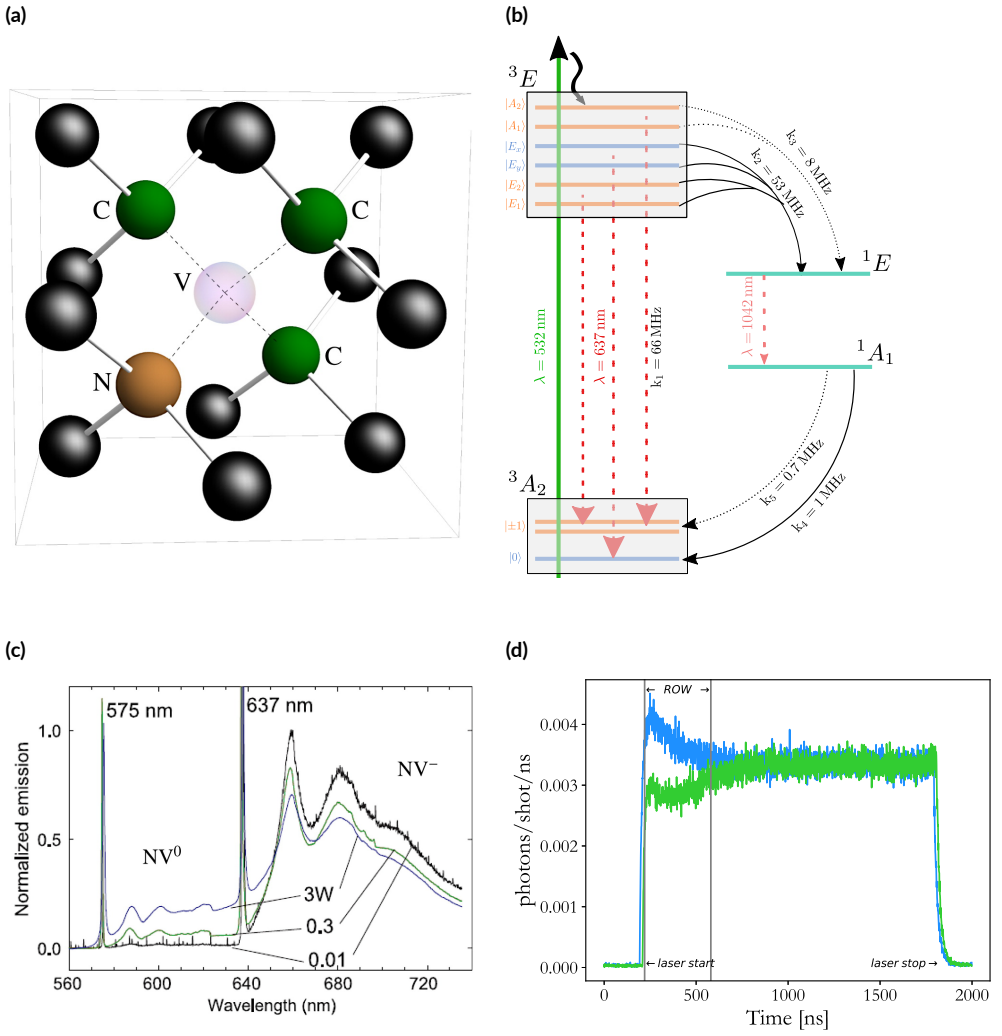

Figure 1.1: (a) Schematic illustration of an NV center in a diamond lattice where the nitrogen atom is an orange ball, carbons are black, near neighbor carbons contributing to the defect are in green, and the vacancy is transparent. The main axis of the defect is the direction connecting the nitrogen and vacancy locations. Illustration reprinted from Ref. 21 (b) Orbital structure of the NV center with spin-orbit coupling states and decay rates. (c) Emission spectrum of ensemble of NV^0 and NV^- excited with 532 nm laser at different powers. Plot reprinted from Ref. 24. (d) Photons collected per shot for the $m_s = 0$ and $m_s = -1$ states.

The ISC decay is characterized by different decay rates for different spin states ($m_s = 0$ and $m_s = \pm 1$). As illustrated in Figure 1.1b, the decay between the excited spin-triplet ^3E to the higher energy spin-singlet $^1A_1$ is more probable for spin states $m_s = \pm 1$. Additionally, the decay from the lower energy spin-singlet $^1E_{1,2}$ to the ground level spin-triplet $^3A_2$ is more likely to result in spin state $m_s = 0$. These differences form the basis for spin initialization and readout.

Spin initialization occurs under green laser illumination, where repeated ISC decay eventually leads to the accumulation of population in the $m_s = 0$ state, achieving spin initialization with a fidelity of up to 96%[21]. Readout is possible due to the lower number of red photons collected for the $m_s = \pm 1$ states following green excitation. This reduction in red photon emission arises from the higher probability of ISC decay and the extended lifetime of the electron in the spin-singlet states before returning to the ground state[26]. The longer lifetime delays photon emission, reducing the number of red photons detected for $m_s = \pm 1$ compared to $m_s = 0$ within a short time window at the onset of green excitation (denoted as the readout window (ROW) in Figure 1.1d). Figure 1.1d illustrates the difference in red photon emission over a 200 ns interval from the start of green laser excitation.

The ISC-based readout mechanism provides a non-ideal method for detecting the sensor state due to low photon collection efficiency and photon shot noise. Consequently, the readout contrast is limited by the difference in the fraction of photons collected per shot for each spin projection ($m_s = 0, -1, +1$)[21]. To accurately determine the spin state, the measurement must be repeated R times, summing all detected photons within the short ROW after excitation (Figure 1.1d).

To determine the required number of repetitions (R) for signal detection, two key sensor characteristics must be considered: the signal-to-noise ratio (SNR) and contrast (C). The SNR, defined in Equation 1.1, quantifies the difference signal per shot between spin states ($\alpha_0 - \alpha_{\pm 1}$) relative to the noise, given by the variance of each spin state ($\sqrt{\sigma_0^2 + \sigma_{\pm 1}^2}$). In a system where noise is dominated by photon shot noise the variance will be the signal per shot, $\sigma_{m_s}^2 = \alpha_{m_s}$. The noise can be reduced by a factor of $\sqrt{R}$ through repeated measurements. The contrast, defined in Equation 1.2, represents the difference between the two spin state signals. A sensor with low contrast requires more measurement repetitions to achieve sufficient contrast to overcome system noise[30].

$$\mathrm{SNR} = \frac{\alpha_0 - \alpha_{\pm 1}}{\sqrt{\sigma_0^2 + \sigma_{\pm 1}^2}} \tag{1.1}$$

$$C = \frac{\alpha_0 - \alpha_{\pm 1}}{\alpha_0 + \alpha_{\pm 1}} \tag{1.2}$$

The NV center can also be used as a single-shot read-out sensor. Two main methods that have been reported require more advanced setups to implement. The first requires a cryogenic environment where the energy levels in the excited level spin-triplet ^3E are well-defined and not perturbed by phonons. In that scenario, an on-resonance laser can excite the spin from the ground level to the excited and allow detection of the spin state upon a single measurement with fidelity of 93%[31,30].

The second method requires good coupling to a neighbor nuclear spin and good control of each of the spins, NV center electron spin, and nuclear spin. In this method, the NV center's state is imprinted on the highly-coherent nuclear spin, utilizing it as a memory, and by conditional driving, a repeated read-out of the NV center indicates the nuclear spin state, and from this, the NV center state with fidelity of 92%[30].

In the research work presented in this thesis, no single-shot read-out techniques were used. Moreover, Chapter 4 addresses the challenge of adapting algorithms designed for single-shot read-out sensors to a non-single-shot read-out framework, as is the NV center at room temperature, which is commonly used in many applications.

1.2.2 The NV center - electron spin properties as a quantum sensor

Out of the three requirements presented above for a quantum system to qualify as a quantum sensor, only the second one of initialization and read-out is established and achieved solely by the electron-spin hybridization diagram. To achieve the other two, an understanding of the ground state spin-triplet physics under static and oscillating magnetic fields is required.

The NV center electron spin has a spin of $S = 1$. A strong zero-field energy (D) caused by the diamond lattice dictates the preferred orientation of the spin in space and the eigenvalues of the system of $m_s = 0, +1, -1$. The interaction of the zero-field with the spin is through the S_z spin triplet operator squared, as noted in the spin Hamiltonian in Equation 1.3a. This interaction causes an energy gap of $D = 2.87$ GHz between the $m_s = 0$ state and the $m_s = \pm 1$ states. The direction $\hat{z}$ is along the defect axis connecting the nitrogen atom and the vacancy in the diamond lattice (see illustration in Figure 1.1a). This direction will also determine the way other vectors in space are treated in the NV center frame of reference.

The Hamiltonian in Equation 1.3a describes the NV energy under a bias magnetic field $B_z^{(0)}$ oriented along the preferred axis $\hat{z}$. This field lifts the degeneracy of the

$m_s = \pm 1$ states through Zeeman interaction, separating them by the energy of $\omega_0 = 2\gamma_{\mathrm{NV}} B_z^{(0)}$, as illustrated in Figure 1.2a where $\gamma_{\mathrm{NV}} = 28.03\,\mathrm{GHz/T}$ is the gyromagnetic ratio of an electron. Lifting the degeneracy allows working with the NV center as a two-level system once choosing one of the spin transitions- $|0\rangle \rightarrow |1\rangle$ or $|0\rangle \rightarrow |-1\rangle$.

$$\mathcal{H}_{\mathrm{Lab}} = DS_z^2 + \gamma_{\mathrm{NV}} B_z^{(0)} S_z \tag{1.3a}$$

$$\mathcal{H}_{\mathrm{Lab}} = DS_z^2 + \gamma_e B_z^{(0)} S_z + \gamma_{\mathrm{NV}} B_x^{(1)} \cos\left(\omega_{\mathrm{MW}} t + \varphi\right) S_x \tag{1.3b}$$

To manipulate the NV center for quantum sensing schemes, the spin has to be treated as a two-level system[2], and a driving field is needed to allow neglecting one of the spin states. The driving field can be a magnetic oscillating field with amplitude $B^{(1)}$, a microwave (MW) frequency ω_{MW} matching the resonance of $|0\rangle \rightarrow |-1\rangle$ or $|0\rangle \rightarrow |1\rangle$, and a phase φ as written in Equation 1.3b. Using such a field encourages us to use the rotating wave approximation (RWA), where the addressed states $m_s = 0$ and $m_s = -1$ or $m_s = 1$ are the sensing two-level system and the $m_s = 1$ or $m_s = -1$, respectively, will result as a fast-rotating term, allowing us to neglect it and ignore it for the rest of the discussion.

Therefore, the Hamiltonian, after applying the RWA, in Equation 1.4, can be approximated to a two-level system with spin $S = 1/2$ operators ($\sigma_{x/y/z}$) and $\Delta_\pm = D \pm \gamma_{\mathrm{NV}} B_z^{(0)} - \omega_{\mathrm{MW}}$ is the detuning of the driving from the chosen spin transitions. The second term in Equation 1.4 indicates the rotation of the spin around an axis defined by φ on the transverse plane of the NV center.

$$\mathcal{H}_{\mathrm{Rot}}^{\pm} = \Delta_\pm \sigma_z + \gamma_{\mathrm{NV}} B_x^{(1)} \left(\cos(\varphi)\sigma_x + \sin(\varphi)\sigma_y\right) \tag{1.4}$$

From this picture, it is clear that a bias DC magnetic field ($B_z^{(0)}$) and an on-resonance oscillating magnetic field ($B^{(1)}$) provide the other two necessary requirements for the NV center to be a quantum sensor. The DC field allows the separation of energy levels to have three well-defined states, and the oscillating field creates an effective two-level system that can be manipulated on the Bloch sphere by tuning the phase and time of the $B^{(1)}$ applied field. Combining all three requirements with the theoretical background provided about the NV center, we can discuss the practical methods used to characterize an NV center in order to coherently manipulate it and use it as a magnetic sensor.

For coherent control, we need to establish the resonance frequency of the NV center, i.e., the bias DC field ($B_z^{(0)}$), and the time dependency of the NV rotation around σ_x induced by an oscillating magnetic field, i.e., the driving field ($B^{(1)}$). To this end, I

will present the Optically Detected Magnetic Resonance (ODMR) method for $B_z^{(0)}$ detection and the Rabi oscillations measurement for $B^{(1)}$ estimation.

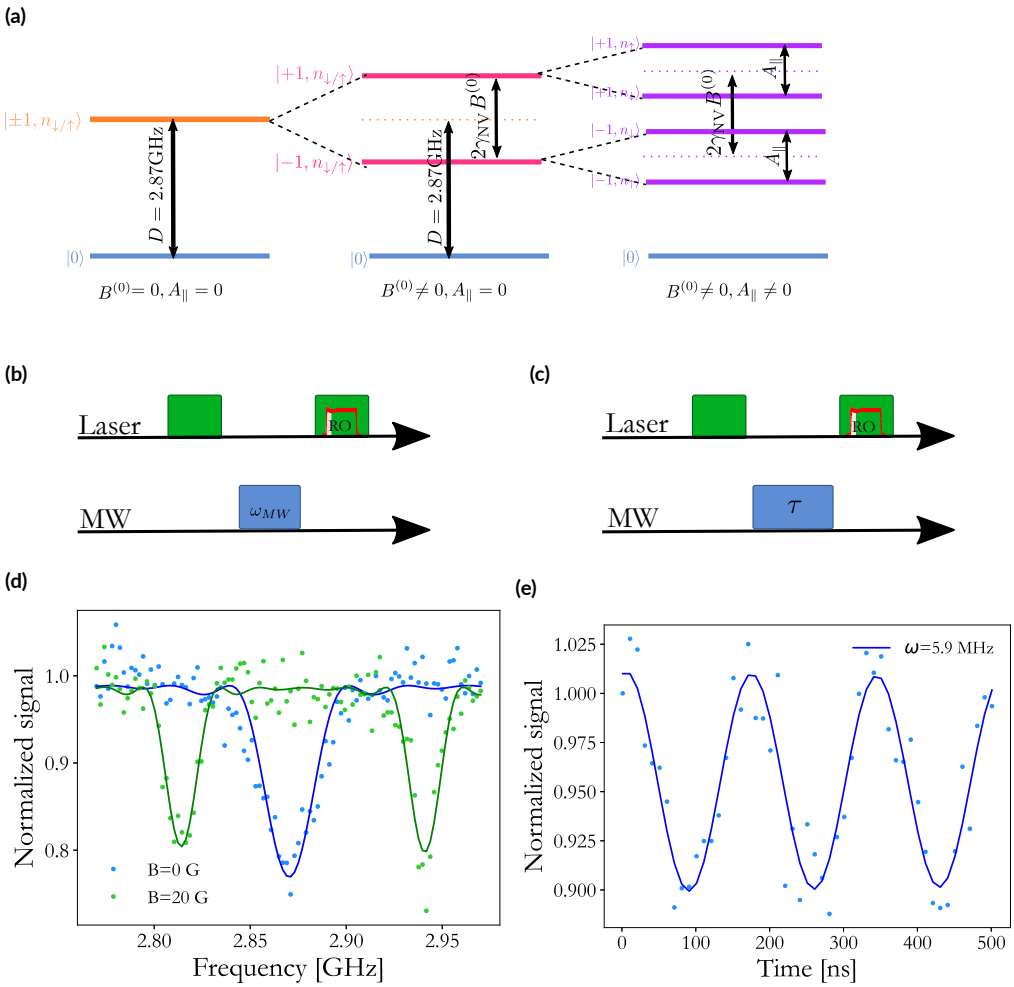

Figure 1.2: (a) NV center spin energy levels. Spin state m_s=0 (blue) shows different energy gaps from states m_s=±1 depending on the environment of the spins. On the left without magnetic bias field or hyperfine coupling (m_s=±1 orange), in the middle with a non-zero magnetic field and no hyperfine coupling (m_s=±1 pink), and on the right with non-zero magnetic field and hyperfine coupling (m_s=±1 purple). (b, c) Illustrations of a pulsed ODMR (b) and Rabi (c) sequences. Green laser pulses are used to initialize and read out the spin state. (b) Microwave π pulse (blue) with varied frequency is used to detect the resonance frequency of the sensor. (c) Microwave pulse with frequency ω_{MW} and varied time (blue) is applied to detect the driving field strength. (d) ODMR measurements of an NV center, one with no magnetic field (blue) applied with the resonance frequency of ω_{MW}=2.87 GHz and another with a magnetic field of B=20 G with two resonance frequencies of ω_{MW_1} =2.81 GHz and ω_{MW_2}=2.94 GHz. (e) Rabi measurement of an NV center with the oscillation frequency of 5.9 MHz.

The ODMR pulse sequence is illustrated in Figure 1.2b. The NV center is initialized to the $m_s = 0$ spin state with a green laser, then it is manipulated by an oscillating magnetic field with a frequency ω_{MW}. Finally, the spin state is read out with another green laser pulse while collecting red photons in the ROW. The spin is expected to rotate from the $m_s = 0$ to $m_s = -1$ (the state chosen to work with) only if the frequency of the driving field is on resonance - $\omega_{\mathrm{MW}} = \Delta_- = D - \gamma_{\mathrm{NV}} B_z^{(0)}$. Once it is rotated to $m_S = -1$ a reduction in the number of collected red photons is measured. Figure 1.2d shows two examples of ODMR measurements from an NV center with no bias field and with a bias field of 20 G.

The Rabi pulse sequence is illustrated in Figure 1.2c. The NV center is initialized to the $m_s = 0$ spin state with a green laser, then it is manipulated with an on-resonance magnetic field with amplitude $\omega_1 = \gamma_{\mathrm{NV}} B^{(1)}$ for changing durations τ. Finally, the spin state is read-out with another green laser pulse while collecting red photons in the ROW. As the driving field is applied on resonance, it is expected to rotate the spin state with an angle $\theta = \omega_1 \tau$ around the rotation axis. This behavior was modeled by Isidor Isaac Rabi, after whom the pulse sequence is named, in 1937, as presented in Equation 1.5 [32]. This model predicts the sinusoidal behavior of the spin, transduced in the NV center system to red photon fluorescence, as presented in an example measurement in Figure 1.2e. The general frequency of the oscillations for any driving frequency is $\Omega = \sqrt{(\omega_{\mathrm{MW}} - \Delta_-)^2 + \omega_1}$.

$$S(\tau) = \frac{\omega_1^2}{\Omega^2} \sin^2\left(\frac{\Omega\tau}{2}\right) \tag{1.5}$$

By extracting from a Rabi measurement the Rabi frequency Ω, one can manipulate the sensor to any state on the Bloch sphere by applying gates (MW pulses) with the correct phase and length. For example, a pulse rotating the sensor from the initialized state $|0\rangle$ by an angle of π can be done by delivering a pulse of length $\tau = \frac{2\pi}{\Omega}$ at any phase, to rotate the spin to a superposition of the two spin levels will require a $\frac{\pi}{2}$ pulses where the phase of the pulse will determine the phase between the states. Therefore, all pulses on the NV will be denoted with the expected rotation angle and phase θ_φ.

1.2.3 Utilizing the NV center as a quantum magnetometer

So far, the basic requirements for using the NV center as a quantum sensor have been established. To use the presented techniques and tools for quantum sensing, the sensor's interaction with the target needs to be established. In this work, I concentrate on magnetic interactions of the NV center with the environment, although it is also

a good sensor for other physical fields such as electric fields[33], temperature[34], pressure[35], and strain[36]. Equation 1.6 captures the NV center's magnetic interactions in the Hamiltonian.

We can divide the Hamiltonian into three main terms. The first, $\mathcal{H}_0$, consists of the ZFS Hamiltonian ($\mathcal{H}_{ZFS}$) and the Zeeman Hamiltonian caused by the bias field aligned with the NV center axis ($\mathcal{H}_{B^{(0)}}$). The second includes all external interactions ($\mathcal{H}_{int}$) through hyperfine ($\mathcal{H}_{HF}$) or dipolar ($\mathcal{H}_{dd}$) interactions. The third is any Zeeman interaction caused by an unknown external magnetic field ($\mathbf{B}$) that can also add Zeeman interaction to any spin interacting with the NV center ($\mathcal{H}_{Zeeman}$).

$$\begin{aligned}\mathcal{H}_{\text{Lab}} = &\overbrace{\underbrace{DS_z^2}_{\mathcal{H}_{ZFS}} + \underbrace{\gamma_{\text{NV}} B_z^{(0)} S_z + \gamma_N B_z^{(0)} I_z^N + \gamma_e B_z^{(0)} \sigma_z^e}_{\mathcal{H}_{B_z^{(0)}}}}^{\mathcal{H}_0} \\ &+ \overbrace{\underbrace{\mathbf{I^N A^N S}}_{\mathcal{H}_{\text{HF}}} + \underbrace{\omega_{dd}\left[3\left(\mathbf{S}\cdot\hat{\mathbf{r}}\right)\left(\boldsymbol{\sigma}^{\mathbf{e}}\cdot\hat{\mathbf{r}}\right) - \mathbf{S}\cdot\boldsymbol{\sigma}^{\mathbf{e}}\right]}_{\mathcal{H}_{\text{dd}}}}^{\mathcal{H}_{\text{int}}} \\ &+ \overbrace{\gamma_{\text{NV}}\mathbf{B}\cdot\mathbf{S} + \gamma_N \mathbf{B}\cdot\mathbf{I^N} + +\gamma_e \mathbf{B}\cdot\boldsymbol{\sigma}^{\mathbf{e}}}^{\mathcal{H}_{\text{Zeeman}}}\end{aligned} \tag{1.6}$$

The hyperfine interaction term ($\mathcal{H}_{HF}$) introduces a coupling of the NV center with another spin ($\mathbf{I^N}$) through the hyperfine matrix $\mathbf{A}^N$; the most common spins are the NV center nitrogen (^{14}N or ^{15}N) nuclear spin and carbon-13 isotopes (^{13}C) in the lattice. The dipole-dipole interaction term ($\mathcal{H}_{dd}$) establishes the interaction of the NV center with any adjacent spin where $\omega_{dd} = \frac{\mu_0 \gamma_e \gamma_{\text{NV}} \hbar}{2r^3}$ is the dipole-dipole interaction factor calculated from the gyromagnetic ratios of the interacting spins, and the distance between them cubed.

In most cases, the bias magnetic field oriented along the NV $\hat{z}$ axis, together with the strong ZFS, is larger than most perturbations of the NV center ($\mathbf{A^N} / \omega_{dd} / \gamma_{\text{NV}}\mathbf{B} \ll \left(D + \gamma_{\text{NV}} B_z^{(0)}\right)$). This defines a quantization axis to the NV center parallel to the $\hat{z}$ axis, which also defines the eigenstates and eigenvalues that can be driven with a transverse on-resonance MW field as shown in Equation 1.3b. Applying these fields allows us to invoke the RWA on the NV Hamiltonian, resulting in Equation 1.7 and neglecting the eigenstate of the NV center not on-resonance with the MW field allowing to change the NV spin operators to the Pauli operators for a two-level system.

In addition, any NV operators not on the quantization axis are rotating fast and,

therefore, negligible, resulting only in σ_z operators with Δ being the detuning of the NV center resonance frequency from the driving frequency ω_{MW}. Other spins with frequencies off-resonance of the driving field will not be affected. Terms of interaction between the NV center and other spins are also affected by the RWA, leaving terms of the $\hat{z}$ axis as resulted with the dipolar coupling term in Equation 1.7 (see Appendix B.1 for an analytical derivation). As the $\hat{z}$ axis of the NV center dictates the sensor orientation, this will also be the leading axis henceforth in this work, forcing any other vector to be treated in the NV center's frame of reference.

$$\begin{aligned}\mathcal{H}_{\mathrm{Rot}} = &\overbrace{\Delta\sigma_z^{\mathrm{NV}} + \gamma_N B_z^{(0)} I_z^N + \gamma_e B_z^{(0)} \sigma_z^e}^{\mathcal{H}_0} \\ &+ \overbrace{A_{zz}^N I_z^N \sigma_z^{\mathrm{NV}} + \omega_{dd}\left[3(\cos^2(\theta)-1\right]\sigma_z^e \sigma_z^{\mathrm{NV}}}^{\mathcal{H}_{\mathrm{int}}} \\ &+ \overbrace{\gamma^N B_z I_z^N + \gamma_e B_z \sigma_z^e}^{\mathcal{H}_{\mathrm{Zeeman}}}\end{aligned} \tag{1.7}$$

Under the simplified picture considered with the RWA, these interactions can be separated into two groups: DC and AC interactions. Each group has a range of pulse sequences aiming to filter out any noises in the system and enhance sensitivity to the target field in question. To demonstrate this, I present here the basic principles of two basic pulse sequences, one for each group. These schemes are also the foundation for most of the research discussed in this thesis and are also a good starting point for understanding many other sensing schemes used in the field today.

The first step for many of the sensing schemes is to initialize the NV center in a superposition state by applying a $\frac{\pi}{2}$ gate after green laser initialization (Equation 1.8a). The NV center, as an electron spin, interacts with external fields by precessing about them (in a classical picture). By initializing it in a superposition, that is, along an axis perpendicular to the sensor quantization axis, it will precess around fields with a component parallel to the NV center quantization axis. The precession of the spin around such a field will be evident by the phase accumulated in the superposition state, which will be proportional to the magnetic field and the sensing time (Equation 1.8b).

$$|\psi\rangle(0) = \frac{1}{\sqrt{2}}\left(|0\rangle + |1\rangle\right) \tag{1.8a}$$

$$|\psi\rangle(\tau) = \frac{1}{\sqrt{2}}\left(|0\rangle + e^{i\varphi}|1\rangle\right) = \frac{1}{\sqrt{2}}\left(|0\rangle + e^{i\gamma_{\mathrm{NV}}B\tau}|1\rangle\right) \tag{1.8b}$$

DC magnetometry

The first group of interactions is DC interactions. The third and fourth terms in the Hamiltonian (Equation 1.6) can be modeled as DC interactions where the hyperfine or dipolar coupling effectively shifts the NV center energy levels while lifting the degeneracy of the coupled spin state. For example, Figure 1.2a presents schematics of the NV center energy levels under a strong hyperfine coupling to a nuclear spin. Most strong hyperfine couplings are usually found with the nitrogen nuclear spin of the defect where the hyperfine strengths of ^{15}N to the electron spin are $A_{\parallel} = 3.03\,\mathrm{MHz}$ and $A_{\perp} = 3.65\,\mathrm{MHz}$[37] or with the nuclear spin of the carbon isotope ^{13}C where the strength of the coupling depends on the distance (and relative angle) of the nuclear isotope from the defect[38].

The pulse sequence I focus on for DC interaction sensing is Ramsey magnetometry. The pulse sequence is illustrated in Figure 1.3a, where it starts with initializing the sensor in a superposition. The spin accumulates a phase during the sensing period as described above, and finally, it is projected back on the read-out axis with a $\frac{\pi}{2}$ gate. During this scheme, any fast-rotating AC magnetic field is averaged to zero, leaving only DC static fields to dominate the accumulated phase. This pulse sequence is also the foundation of the methods reported in Chapters 2 and 4.

Figure 1.3b displays two examples of Ramsey measurement detecting the hyperfine interaction with the nitrogen nuclear spin. Both were measured from the same NV but with different ω_{MW} frequencies of the driving $B^{(1)}$ field. The signal in blue was measured with a driving frequency situated in the middle between the two eigenstates of the NV center, separated by 3 MHz due to the nitrogen hyperfine coupling, revealing two oscillating signals from two DC fields rising from the two detuned eigenstates of the sensor. The signal in purple was measured with a driving frequency that exactly matched one of the eigenstates, showing only one robust oscillating signal from the 3 MHz detuning from the second eigenstate. Both measurements indicate a decoherence time of approximately $T_2^* = 2\,\mu\mathrm{s}$.

The non-single-shot nature of the NV center obliges us to repeat such a measurement for R number of times, creating an averaging effect of noise on the signal, which translates into fast decay of coherence (discussed widely in Chapters 2 and 4). This decoherence of the Ramsey measurement is expressed as the T_2^* decay time, which is also the limiting factor of the measurement and a result of the inhomogeneous spin dephasing averaging. This time is translated to the possible strength of DC magnetic fields that can be detected $\gamma_{\mathrm{NV}} B_{\parallel} \leq \frac{1}{T_2^*}$[39].

AC MAGNETOMETRY

The second group of interactions is AC fields. AC magnetic fields can be found, for example, in the bath of nuclear spins oscillating in the Larmor frequency in the vicinity of the sensor. One basic pulse sequence for AC magnetometry is the Hahn echo[40]. The pulse sequence is illustrated in Figure 1.3c. It also starts with initializing the spin into a superposition state. However, differently from Ramsey magnetometry, there is an additional π gate located within the sensing period between the first and second $\frac{\pi}{2}$ gates. At each of the interaction periods, the sensor is accumulating a phase proportional to the interaction time $\varphi_{1/2} = \gamma_{\mathrm{NV}} B_{\parallel} \tau_{1/2}$. The phase accumulated in the first sensing period will flip a sign due to the π gate, resulting in $\varphi_{=} - \gamma_{\mathrm{NV}} B_{\parallel} \tau_1$.

Once the two sensing periods are the same - $\tau_1 = \tau_2$ these phases are the same up to a sign, causing all phases accumulated in the first period to refocus in the second period. This scheme also allows the refocus of the fast-rotating AC fields, contributing to the

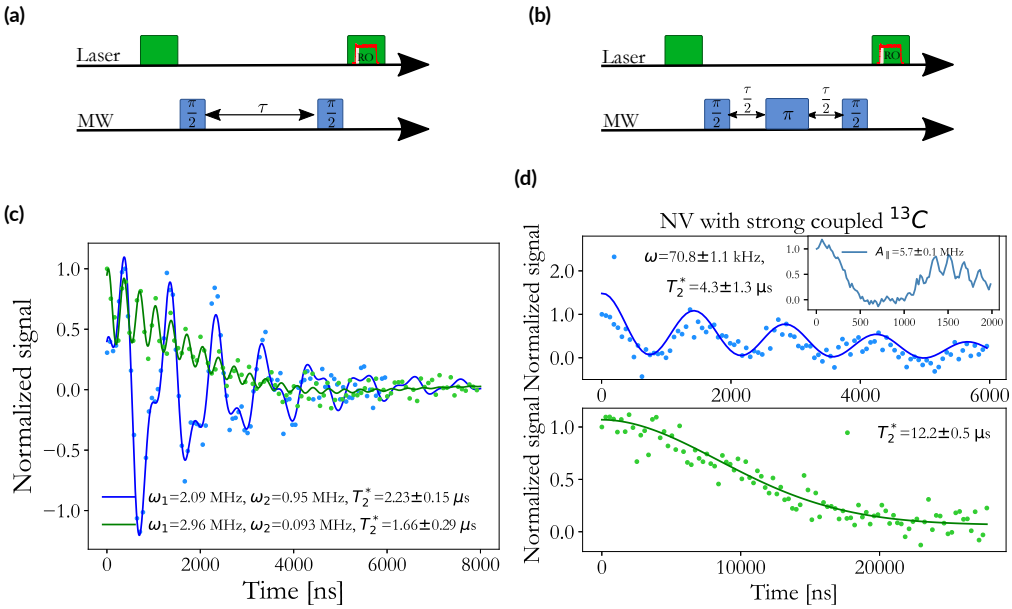

Figure 1.3: (a, b) Illustrations of the Ramsey (a) and Hahn echo (b) pulse sequences. Green laser pulses are used to initialize and read out the spin state. Microwave pulses (blue) on the NV center resonance frequency are used to manipulate the sensor state. (c) Two measured Ramsey signals with oscillations showing the detuning of the driving frequency from the eigenstates of the sensor separated by 3 MHz due to hyperfine coupling the nitrogen nuclear spin. (d) Two measured Hahn echo signals. The blue signal was measured from an NV center with a strongly coupled carbon nuclear spin with an inset of a higher time resolution measurement focused on times up to 4 μs. The purple signal was measured from an NV with no strongly coupled carbons.

fast decoherence of the Ramsey sequence. Nevertheless, an AC field, with frequency on the order of $\omega \simeq \frac{1}{2\tau_1}$ would contribute a field $B_{\|}$ on the first interaction period and exactly the opposite field $-B_{\|}$ on the second period, together these will add up to a detectable phase on the sensor that will not be refocused[39]. Yet, due to the averaging nature of the sensor, it is subjected to decay in the coherence owing to slow oscillating fields. This decoherence is denoted as the sensor's T_2 transverse decay time, which is the homogeneous dephasing of the spin. This time also limits the Hahn echo measurement to fields with frequency higher than $\omega \geq \frac{1}{T_2}$. The upper limit is established by the length of the gates applied to the sensor which depends on the coupling strength to the MW field.

Figure 1.3d shows an example of two Hahn echo measurements of two different NV centers. One NV center, in blue, shows clear collapses of coherence with a frequency of 70.8 ± 1.1 kHz matching the Larmor period of carbon atoms at the bias field of 326 G that was applied externally. On top of the collapses, the inset in Figure 1.3d presents a measurement with higher resolution in time and shows oscillations with a frequency of 5.7 ± 0.1 MHz attributed to the strong hyperfine of the sensor to a carbon nuclear spin[41,38]. The second NV center, in purple, shows no strong coupling to carbon spins and, therefore, a long decay time of 12.2 ± 1.3 µs.

The Hahn echo scheme is the first and most simple pulse sequence from a family of sequences of dynamical decoupling[42,43]. These schemes utilize a train of π gates to refocus the noise and decouple the sensor from a wide range of fields, thus prolonging the coherence time and enhancing sensitivity to the target field. Correlation spectroscopy such as Qdyne improves the spectral resolution of dynamical decoupling techniques to a sub-millihertz resolution[44]. On top of the dynamical decoupling sequences, there are more pulse sequences aiming to cover other regimes of the spectrum, such as relaxometry for fields in the GHz regime[45] and quantum mixing technique for hundreds of MHz regime[46]. These schemes will not be elaborated on in this section since they are out of the scope of this work.

1.2.4 The NV center an electron spin sensor

Sensing electron spins can provide structural and dynamic information of a wide variety of molecules and proteins. A very powerful and widely used technique for this purpose is electron paramagnetic resonance (EPR)[47]. The signal in this technique rises from averaging a magnetic signal over a large sample of the target material, and electron spins in question. Although powerful, this tool lacks the resolution to observe, for example, heterogeneity in the ensemble or time-dependent kinetics of inter-

actions[48]. To this end, sensing methods such as single NV centers in diamonds, which have atomic-size defects, are leading sensors to address the field of single-molecule sensing. This sub-section will cover the methodology used today for single electron spin sensing with NV centers and the achievements of single-molecule sensing with it.

The sensing methods described above are not suitable for electron spin sensing. Due to their large gyromagnetic ratio, electron spins exhibit a high Larmor frequency, rendering AC magnetometry methods based on dynamical decoupling impractical. However, this large gyromagnetic ratio also enhances dipolar coupling between the electron spins and other spins, allowing interaction with the NV center and the induction of a detectable DC magnetic field. This field can be measured using Ramsey magnetometry or ODMR, both of which are constrained by the sensor's dephasing time, T_2^*. Consequently, for effective detection, the interaction strength must exceed $\frac{1}{T_2^*}$, linking NV center decoherence to its proximity to the target spin. A shorter distance enhances dipolar coupling, strengthening the interaction. However, detecting an electron spin external to the diamond lattice requires positioning the NV center near the diamond surface, which increases noise and shortens the decoherence time[13,49], often limiting the detection of dipolar-coupling-induced DC fields.

Exploiting the knowledge and background formed from decades of research from the EPR community, we can adopt a method called double electron-electron resonance (DEER) pulse sequence that overcomes the limit imposed by T_2^* and enhance the sensitivity to the dipolar coupling to a target coupled electron spin[50]. In this sequence, a driving pulse on the target electron spin resonance frequency is used to effectively change the DC interaction to an AC interaction, enabling the use of AC sensing methods like Hahn echo.

The pulse sequence is illustrated in Figure 1.4a and is based on the Hahn echo pulse sequence. A driving π pulse on the target electron spin frequency ω_e (purple) is applied simultaneously with the π pulse addressing the NV center (blue). The target electrons' π pulse flips the state of the target spin, effectively flipping the dipole-dipole interaction sensed by the NV center exactly at the frequency detected by the Hahn echo interaction time, therefore accumulating a phase caused by this interaction. The flipping is possible if the target spin eigenstates are well-defined and the interaction Hamiltonian follows Equation 1.7.

Using the DEER pulse sequence while varying the interaction times, named DEER-time henceforth, can be a platform for detecting dipolar coupling. The phase accumulated on the superposition state with each interaction time is proportional to the dipolar coupling such that $|\psi\rangle = |0\rangle + e^{i\varphi}|1\rangle$ where $\varphi \simeq \omega_{dd}\tau$, with a simulation of the

DEER-time pulse sequence presented in Figure 1.4c. The DEER pulse sequence can also detect an ensemble of electrons; in this case, the phase will be a sum of all dipolar couplings, resulting in an exponential decay [51].

Another way to employ the DEER pulse sequence to sense electron spins is to fix the sensing time and apply a π pulse with varying the π pulse frequency, named DEER-

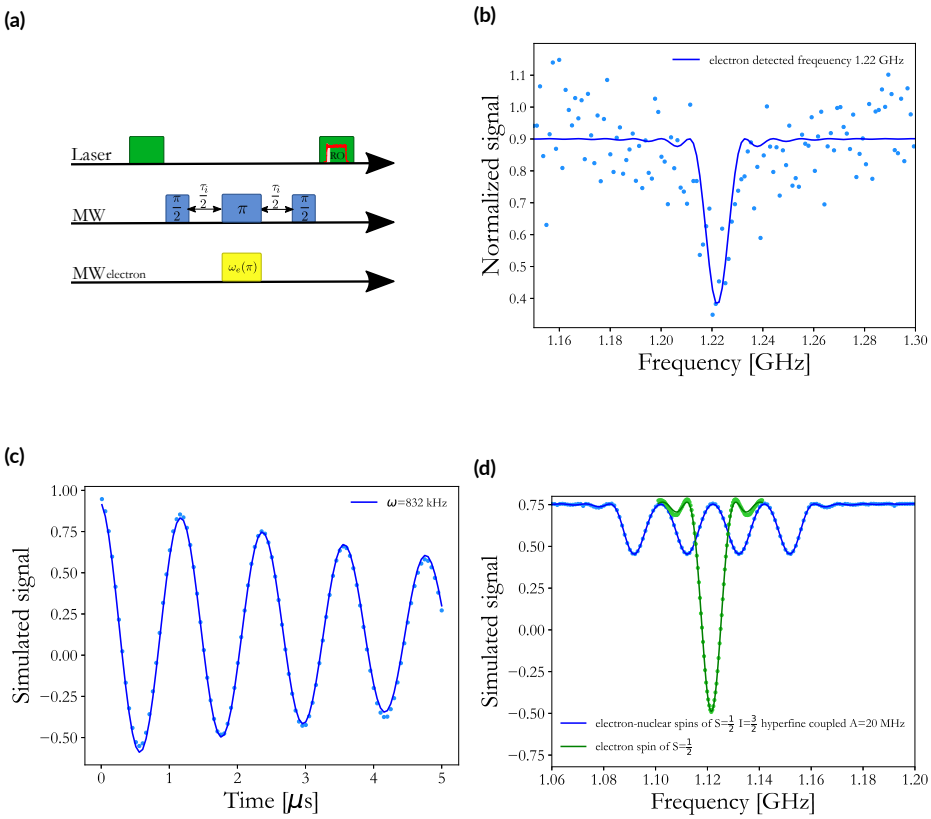

Figure 1.4: (a) Illustrations of the DEER pulse sequence. Green laser pulses are used to initialize and read out the spin state. Microwave pulses (blue) on the NV center resonance frequency are used to manipulate the sensor state, and MW pulses on the target electron resonance frequency (purple) are used to manipulate the electron state. (b) Example of an experimental signal of DEER pulse sequence on an NV sensing an ensemble of free electrons at a biased magnetic field of 480 G. (c) Simulation of a DEER-time pulse sequence where the interaction time is varied, and the driving frequency of the electron is fixed. Oscillations are at 832 kHz rising from the dipolar coupling of the NV center and the electron, which are simulated with a 5 nm distance. (d) Two simulations of a DEER frequency pulse sequence at 400 G where the evolution time is fixed to be $\tau = \frac{3}{2\omega_{dd}} = 1.8\,\mu s$ for maximum signal. The first simulation is of a free electron (green) with one resonance frequency detected, and the second is of an electron hyperfine coupled to a nuclear spin of copper with $S=\frac{3}{2}$ and hyperfine strength of A=20 MHz (blue) with four detected resonance frequency rising from the hyperfine coupling.

frequency henceforth. This approach aims to find the target electron spin's resonance frequency in the case where the frequency is not a result of only the Zeeman shift. For example, due to hyperfine coupling, different gyromagnetic ratios (effective g factor), or chemical shifts caused by the chemical environment of the electron spin. In this case, the sensing time is usually set to be the T_2 of the sensor to allow accumulating most of the phase before completely losing the signal.

Figure 1.4d shows simulations of a DEER pulse sequence for an NV center coupled to electron spin with (blue) and without (green) hyperfine coupling to a nuclear spin of $I = 3/2$. The simulation shows the reduction in signal in a case where the electron spin state is thermally distributed with all four nuclear spin states. In the simulation, the electron spin is situated 5 nm away from the sensor, making them strongly coupled. Therefore, the interaction time chosen was $n \cdot \frac{1}{2\omega_{dd}}$ to accumulate the maximal phase and acquire the maximal signal. Figure 1.4b shows an example measured signal, where the sensor is sensing an ensemble of weakly coupled electron spins. Therefore, the interaction time is set to the T_2 of the sensor to acquire as much signal as possible.

This technique for electron spin sensing was used so far with NV magnetometry for electron spin sensing within the diamond lattice[52], on the surface of the diamond[51], and in molecules situated on top of the diamond[53,54]. It has shown high practicality and applications. However, it is still not free of problems. First, it is limited by the coherence time of the sensor (T_2), as electron spins weakly coupled will not be detected if $\omega_{dd} < 1/2T_2$. Second, the relaxation time of the target electron spin (T_1) has to be longer than the measurement time, electron spins with shorter T_1 will spontaneously flip the state, and it will not be correlated with the sensor's flipping. Finally, as illustrated in Figure 1.4d, an electron spin with a complex resonance frequency structure, for example, due to hyperfine coupling, would be harder to detect in a real-life experiment holding noise sources and further complexity from the target electron system. This challenge is addressed widely in this research in chapters 2 and 3.

1.3 Molecular spin qubits

The second quantum revolution has pushed research to find more quantum systems relevant to technology and application uses. The world of chemistry has, therefore, also entered the quantum technology area by searching for quantum systems within chemical systems. Chemistry has two main advantages that can push forward quantum applications: First, it is a rich world that holds a large variety of techniques, allowing for high flexibility in constructing chemical compounds with the relevant re-

quirements for a specific quantum system. Second, it bears the potential for scaling up quantum systems for quantum information processing purposes, since molecules are identical units holding identical properties[55,56,57].

These advantages are a good motivation to search and design molecules that can fulfill all five requirements from quantum bit (qubit) to be a good candidate for quantum information processing in general and quantum technologies specifically[58]. The five requirements include some of the requirements from a quantum sensor presented in Section 1.1, such as being able to initialize and coherently manipulate the qubit. On top of these, the system should also have a long coherence time, the ability to apply a universal set of quantum gates and be scalable where each qubit can be individually addressed and measured.

The search within the world of chemistry for quantum systems is focused on a group of molecules named molecular spin qubits (MSQ). MSQs can be a large variety of molecules that hold an electronic spin[59,56]. Many MSQs consist of at least one metal ion surrounded by organic ligands. The qubit is the electron spin concentrated on the metal ion, which can have discrete resolved eigenstates upon a bias magnetic field, and these states can be addressed using a relevant MW field. Surrounding the metal ion, there are ligands that can act as a shield from noise when using spin-free atoms and designing it to fit in a spin-free environment[60,61].

This structure also allows for the increase of the qubit coherence time at temperatures above liquid helium. These two characteristics satisfy two of the addressed requirements above. The design of the molecules in such a way that they can create chemical chains or sheets of MSQs makes this system potentially possible to scale up[53,62]. Scaled-up systems, along with strong gradient fields that can make them spectrally separated by special locations, can also be individually addressed[63,64,65,52] (see also Appendix F.1). Finally, out of the five requirements, only initialization and individual read-out are left. Recent studies also focus on a group of molecules with electron energy levels similar to the NV center scheme offering optical initialization and read-out[66,67,68].

All the traits mentioned above form the great potential hidden in the rich world of molecular spin qubits as possible processing units for quantum technologies. To push the potential to a practical option, research in this field has to gain some insight into the single molecule behavior. So far, the techniques used to study these molecules include EPR[62,69], molecular break junctions[70,71], and scanning tunneling microscopy (STM)[72]. Each provides a different sensing aspect to the molecules. EPR can provide a strong magnetic signal from an ensemble of molecules. However, it is missing the

single-molecule information crucial for making them single-unit processors for quantum technology. Break junctions can also detect electric properties on the single unit regime but lack magnetic information and scalability. Finally, STM-EPR provides the single-unit magnetic aspect but still cannot be easily scaled up and cannot assist with interacting with the MSQ for manipulation purposes.

The NV center, similar to the STM-EPR method, can potentially provide the necessary resolution for single molecule sensing. However, unlike the STM-EPR, it can additionally offer an interaction channel with the MSQ, which is essential for molecules with no optical initialization and read-out. Additionally, the NV center has the potential for scaling up to some degree[73,74,75,76], offering hypothetical parallelizing of a complex system of an NV center coupled to a network of MSQs as a quantum processor[77].

1.4 Research subject and addressed questions

The hypothetical prospect of utilizing the NV center as an atomic scale magnetic sensor for MSQ and employing its advantages in a hybrid quantum system with the MSQs is still a long way from being fully realized. The NV center has proven its ability to sense external electron spins, however, published work in this field focused on electron spins without the complexity of being embedded in a molecule and sometimes strongly coupled to a nuclear spin. Therefore, the research goal is to **use the NV center as a sensor for electron spins in molecules in general and for MSQs specifically**. Achieving this goal will open the possibility of using the NV center for more complex sensing applications.

Based on the knowledge gathered for decades on the NV center as a sensor, we want to establish a methodology for using it to sense electron spins with the complexity inherited from the molecule they are part of. To this end, I aim to enhance the sensitivity and stretch the limits of the NV center while utilizing different technical methods. The methods I studied also form the subjects addressed in the study with respect to the benefit they bring to the NV center's sensing abilities:

- **Extending the NV center coherence time for MSQ sensing with correlation spectroscopy**: Study of a novel correlation spectroscopy pulse sequence designed to address complex magnetic spectrum systems while extending the coherence time of the NV center.
- **Enhance electron spin sensing with adiabatic pulses**: Study of the effect that adiabatic pulses have on the sensitivity of NV center to surface electron spins.

- **Enhance DC sensitivity with machine learning in real-time**: Study of a Bayesian inference approach for quantum phase estimation with the NV center as a non-single shot read-out sensor to enhance the sensor sensitivity to DC magnetic fields.

"An expert is a man who has made all the mistakes which can be made, in a narrow field"

Niels Bohr

2

Sensing molecular spin qubits

The main goal of this work is to use the NV center as a quantum magnetic sensor for single MSQ sensing. Although sensing of single electron spins with the NV center was previously performed [52,51,53], the goal of sensing an electron spin inside a molecule holds several challenges. This chapter focuses on the effort invested in overcoming these challenges and pushing the NV center sensing abilities closer to the desired goal of sensing MSQ and potentially also forming a hybrid system of NV center and MSQs.

MSQs exist in various forms, and given that the primary motivation of this work is the sensing capabilities of the NV center, we focused our study on two potential MSQs. The first, copper phthalocyanine (CuPc)[62], served as the target molecule for both the numerical and experimental research presented in this chapter. The theoretical background of CuPc and the rationale for selecting it will be discussed in Section 2.1. The second MSQ, synthesized by Prof. Danna Freedman's group at the Massachusetts Institute of Technology (MIT)[61], consists of a vanadium metal center surrounded by sulfur-based ligands. While promising in some aspects, this molecule posed challenges when applied to the diamond surface. Consequently, it was not the primary focus of this chapter. The background and efforts related to this MSQ are

detailed in Appendix C.2.

Focusing on CuPc as the target MSQ, I introduce a novel pulse sequence in Section 2.2, which includes an adiabatic microwave pulse to manipulate the MSQ spin and a correlation scheme designed to enhance the NV center's coherence. In Section 2.3, I present the experimental and numerical results of the pulse sequence, structured into three subsections. The first (Subsection 2.3.1) presents numerical simulations that outline the potential applications of the proposed approach. The second (Subsection 2.3.2) provides an experimental proof of concept. The third (Subsection 2.3.3) details experimental results obtained from an optimized sample, while additional preliminary samples are discussed in Appendix C.1. Finally, I conclude the chapter by summarizing the key achievements of this work and highlighting open challenges that require further investigation.

2.1 Background

To use the NV center as a quantum sensor for the electron spin in an MSQ, we begin with the DEER pulse sequence, introduced in Subsection 1.2.4, a standard method for electron spin sensing. For this method to yield a detectable signal, the dipole-dipole interaction between the sensor and the target spin must be sufficiently strong, satisfying the condition $\omega_{dd} \geq \frac{1}{T_2}$. The interaction strength (ω_{dd}) primarily depends on the distance between the spins. Therefore, to sense electron spins external to the diamond lattice—specifically, spins embedded in molecules—the target spins must be positioned on the diamond surface, while the NV centers must be as close to the surface as possible. This necessitates the use of shallow-implanted NV centers (see Appendix A.3). Consequently, the diamond surface becomes a crucial parameter, influencing key considerations for selecting suitable MSQs and determining the necessary surface treatments for the diamond.

Beyond surface considerations, two additional essential requirements must be met for a viable MSQ. First, the MSQ should exhibit long coherence (T_2) and relaxation (T_1) times, which are critical for quantum sensing and processing. Reported relaxation times in the literature provided an initial basis for selection. However, it is important to note that most molecules experience a reduction in relaxation and coherence times when placed in environments with a high density of electron spins—including MSQs themselves. This constraint necessitates choosing MSQs in a way that allows control over their surface density on the diamond.

Second, the molecular structure and hyperfine interactions significantly influence

the target's magnetic spectrum. The MSQs considered in this work contain a metal atom with a high nuclear spin, which interacts with the target electron spin via hyperfine coupling. This interaction modifies the magnetic spectrum of the electron spin and, if $A^N \geq \gamma_e B^{(0)}$, also alters its quantization axis. In such cases, it is crucial to select molecules whose preferred orientation on the diamond surface can be controlled, as illustrated in Figure 2.1b. This control minimizes variations in the alignment of the MSQ's quantization axis relative to that of the NV center, ensuring more consistent and predictable measurements.

2.1.1 Copper phthalocyanine

Considering the above requirements, the MSQs selected for this study were copper phthalocyanine (CuPc) with the molecular formula $C_{32}H_{16}CuN_8$[62] (Figure 2.1a) and vanadium-based complexes $V[C_8S_8]_3$ and $VO[C_8S_8]_2$, synthesized by Prof. Danna Freedman's group[61]. This chapter focuses on CuPc, as it best met some selected criteria, while efforts on vanadium-based complexes are detailed in Appendix C.2.

CuPc is well-studied, with research reported on its layer formation[78,79], annealing effects[80,81,82], purification[83], optical properties[84], and magnetic characteristics[62,85]. These studies confirm that CuPc meets most of the key requirements, detailed below:

1. **Magnetic properties**
   (a) Decoherence time (T_2) of microseconds at cryogenic temperatures[62].
   (b) Relaxation time (T_1) in the millisecond range when deposited at low density and low temperature[62] (Figure 2.1c).
2. **Controlled surface deposition**
   (a) Depositable via molecular evaporation, allowing high control over layer formation[86,87].
   (b) Planar structure promotes alignment with a 54.7° angle relative to the NV center, reducing orientation uncertainty[88] (Figure 2.1b).
   (c) Controlled concentration achievable by co-depositing H_2 phthalocyanine (H_2Pc), ensuring a low electron spin density[89,62,90] (Figure 2.1a).
3. **Potential hybrid NV center–MSQ quantum device**
   CuPc's compatibility with molecular evaporation facilitates its use in quantum networks, where NV centers act as initialization and readout qubits while MSQs function as processors.

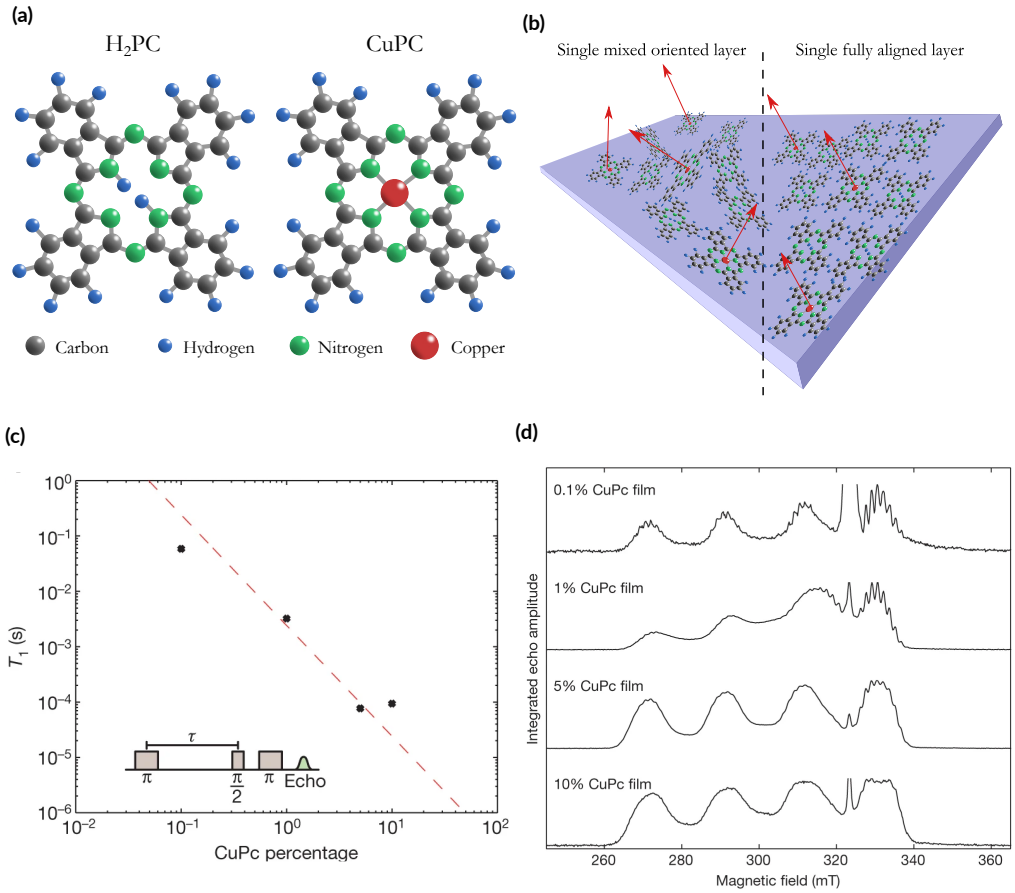

Figure 2.1: (a) Illustrations of a CuPc (left) and H_2Pc (right) molecule. (b) Schematic representation of CuPc and H_2Pc molecular layers on a diamond surface, shown without (left) and with (right) a preferred orientation, where the latter are aligned flat on the surface. Red arrows indicate the electron spin quantization axis in the absence of a magnetic field. (c) EPR measurements of CuPc relaxation time (T_1) at varying concentrations.(d) EPR magnetic resonance spectra of CuPc at different concentrations. Panels (c) and (d) are reprinted from Ref.62.

The magnetic spectrum of CuPc, measured via EPR, reveals four main resonance frequencies[62] (Figure 2.1d). At lower CuPc concentrations, additional resonances appear, attributed to the electron spin Hamiltonian (Equation 2.1). The electron spin exhibits strong hyperfine coupling to the $I^{\mathrm{Cu}} = 3/2$ copper nuclear spin, with reported values of $A^{\mathrm{Cu}}_{zz} = -648\,\mathrm{MHz}$ and $A^{\mathrm{Cu}}_{xx/yy} = -83\,\mathrm{MHz}$, which generate the four primary resonance peaks. Additional resonances arise from hyperfine interactions with four neighboring $I^N_i = 1$ nitrogen nuclei ($A^N_{xx} = 57\,\mathrm{MHz}$, $A^N_{zz/yy} = 45\,\mathrm{MHz}$).

$$\mathcal{H}_{\mathrm{CuPc}} = \gamma_e \mathbf{B}^{(0)} \boldsymbol{\sigma}^{\mathbf{e}} + \mathbf{I}^{\mathrm{Cu}} A^{\mathrm{Cu}} \boldsymbol{\sigma}^{\mathbf{e}} + \sum_{i=1}^{4} \mathbf{I}_{\mathbf{i}}^{\mathbf{N}} A_i^N \boldsymbol{\sigma}^{\mathbf{e}} \tag{2.1}$$

The hyperfine coupling along the molecule's $\hat{z}_{\mathrm{CuPc}}$ axis, perpendicular to the molecular plane, dictates its quantization axis and eigenstates. This axis does not necessarily align with the NV center's $\hat{z}$ axis. However, when an external magnetic field $B_z^{(0)}$ is applied parallel to the NV center's $\hat{z}$ axis (Figure 2.2d), the molecule's quantization axis

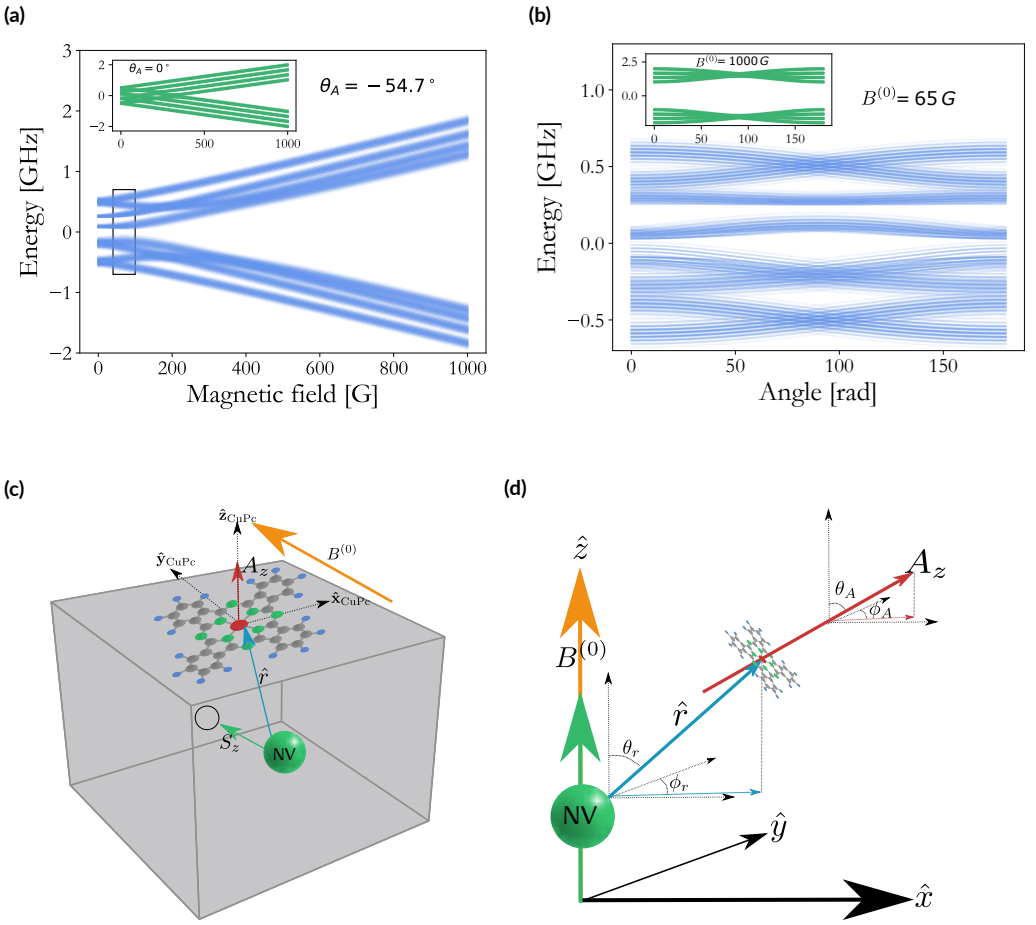

Figure 2.2: (a) Energy diagram of the electron spin of a CuPc molecule as it is changing with the magnetic field strength and with a θ_A=54.7° angle between the molecule $\hat{z}$ axis and the magnetic field direction. The inset shows the energy diagram of the molecule under an aligned magnetic field. (b) Energy diagram of CuPc molecule under a bias magnetic field of 65 G and at different angles between the magnetic field and the molecule $\hat{z}$ axis. The inset shows the energy diagram at a magnetic field of 1000 G. (c) Illustration of the NV center and the CuPc molecule axes as they oriented in the lab frame. (d) The molecule axes system and the vector connecting the NV center and the molecule ($\vec{r}$) rotated to the NV center axes system.

shifts based on field strength ($\mathbf{A}$, $B_z^{(0)}$) and relative angles (θ_A, φ_A) (Figures 2.2c, 2.2d).

Due to CuPc's symmetry in the $\hat{x}_{\text{CuPc}}$ and $\hat{y}_{\text{CuPc}}$ axes, the polar angle φ_A does not affect the electron spin eigenvalues, while the tilt angle θ_A does. When $\theta_A = 0$, the states align with the system's $\hat{z}$ axis, and energy changes follow the Zeeman effect (Figure 2.2a). For $\theta_A \neq 0$, eigenstates and eigenvalues vary across different bias field regimes. When hyperfine coupling dominates ($\gamma_e B^{(0)} \ll A_{zz}$), the electron spin exhibits a $\sim$ 648 MHz energy split (Figure 2.2b). When the Zeeman term dominates ($\gamma_e B^{(0)} \gg A_{zz}$), eigenvalues center around the Zeeman energy, with hyperfine effects determined by the projected hyperfine matrix (inset, Figure 2.2b).

NV centers in diamond are oriented at 54.7° to the surface normal[88]. CuPc, a planar molecule, is expected to form parallel layers on smooth surfaces[91], aligning its $\hat{z}_{\text{CuPc}}$ axis perpendicular to the diamond surface (confirmed in Section 2.2). This results in a system with $\theta_A = 54.7°$ between the molecule's hyperfine axis and the NV center's $\hat{z}$ axis, as shown in Figure 2.2c. In the rotating NV frame (Figure 2.2d), this orientation, along with the molecule's relative position ($\hat{r}$,θ_r, φ_r), determines the system's behavior.

2.1.2 Challenges in sensing MSQs

With the dipole-dipole interaction between the NV center and the CuPc electron spin in focus, we explore the possibilities offered by the DEER pulse sequence discussed in Subsection 1.2.4. This pulse sequence isolates electron spins interacting with the NV center while minimizing noise by employing the Hahn echo pulse sequence, combined with a synchronized MW pulse on the target spin. This MW pulse acts as a selective probe.

One approach is to fix the time between the MW pulses on the NV center ($\tau/2$) to the T_2 of the sensor while sweeping the frequency of the MW pulse (ω_e) applied to the target electron spin to locate its resonance frequency (Figure 1.4d). Alternatively, the frequency of the MW pulse can be set to the resonance frequency of the target spin while sweeping the time between the NV pulses ($\tau/2$) to extract the dipole-dipole coupling strength (ω_{dd}).

Both methods assume the target electron spin has only two energy levels, allowing manipulation with a single MW frequency. However, in MSQs with metal atoms, the electron spin is typically strongly coupled to the metal's nuclear spin—copper in the case of CuPc—causing a breakdown of this simple two-level picture. In thermal equilibrium, the electron spin state distributes among multiple states, making it impossible to define a single frequency for flipping its state. This complicates both approaches, making them impractical in cases involving multiple eigenstates.

In the first approach, a signal is only detected when the MW frequency matches one of the electron spin transitions. Under hyperfine coupling, the spin can occupy multiple states with probabilities dictated by the Boltzmann distribution. Under moderate temperature and magnetic field conditions, this distribution is approximately uniform, reducing the contrast of each detected resonance frequency. The reduction factor is proportional to the inverse of the number of frequencies in a uniform distribution (Figure 1.4d shows a simulation of this case). Since a detectable signal must exceed system noise, a reduction in signal requires an equivalent reduction in noise. Noise decreases with the square root of the number of repetitions, such that $\langle SNR \rangle = \sqrt{N} \cdot SNR$, where SNR is defined in Equation 1.1. If each resonance frequency's signal is reduced by a factor of P, the number of repetitions must increase to $N = P^2$.

Naively, we can assume the CuPc electron spin interacts only with the copper nuclear spin, splitting the energy levels into eight states and producing four electron spin resonance frequencies, meaning $P = 4$. This results in a 16-fold increase in measurement repetitions to achieve the same signal-to-noise ratio. However, additional hyperfine interactions with four nitrogen atoms further split the energy levels, leading to a total of 648 states, causing an exponential increase in measurement repetitions. Longer measurement times introduce additional noise from experimental drifts, making this method impractical.

Beyond signal reduction, hyperfine coupling also alters the spin's quantization axis. A tilted quantization axis complicates the analytical solution, but it is clear that if the quantization axis tilts, the MW driving field should also be adjusted accordingly. In cases where the electron spin is aligned with the NV center, they share the same MW field direction ($\mathbf{B}^{(1)}$). Consequently, Rabi oscillations detected on the NV center directly indicate the MW pulse interaction strength with the target spin, allowing determination of the π pulse duration. However, a tilted quantization axis modifies the MW interaction strength, complicating the application of an ideal π pulse.

Furthermore, the tilted axis give rise to superposition eigenstates, making them linear combinations of the untilted eigenstates. For a simple system involving an electron spin and a copper nuclear spin, the untilted states are $|m_s, m_I^{\mathrm{Cu}}\rangle$, where $m_s = \pm 1/2$ and $m_I^{\mathrm{Cu}} = \pm 3/2 / \pm 1/2$. The resulting superposition reduces the signal further, as a spin-flip may not fully switch the electron spin state but rather alter partial populations. Consequently, the DEER sequence detects only partial spin flips, further weakening the signal.

These effects are illustrated in the simulated DEER frequency sequence results shown

in Figure 2.3. The simulation models a system with a single NV center and an electron spin located 5 nm away, coupled to a nuclear spin of $I = 3/2$ with the CuPc coupling matrix. MW pulses are aligned with the transverse axis of the NV center, while the electron spin's quantization axis shifts according to the hyperfine coupling angle and magnetic field magnitude. The figure displays three cases with magnetic fields of 65 G, 700 G, and 4000 G. The black dashed line highlights four clear resonance frequencies from hyperfine coupling in all three cases as the bias field is aligned with the molecule hyperfine axis. For a small tilt angle (10°), the four resonance frequencies remain distinct across all field strengths, indicating minimal impact on the quantization axis. However, for a tilt angle of 54.7°, expected for CuPc on the diamond surface, the spectrum at 65 G is distorted. At high magnetic fields where $\gamma B^{(0)} \gg A$, the quantization axis remains aligned with the NV axis, preserving the resonance structure.

For the second approach, where the MW pulse frequency is fixed and the interaction time is swept, a resonance frequency of the target electron spin must be selected. Since multiple resonances exist, working with a single frequency reduces the signal by a factor of P. An alternative is to apply an adiabatic pulse, where the MW frequency is swept during the pulse, covering a broader spectral range (see Chapter 3). However, for an adequately broad pulse, the duration must be at least several microseconds (detailed calculations in Section 2.2). As the DEER sequence is constrained by the NV center's

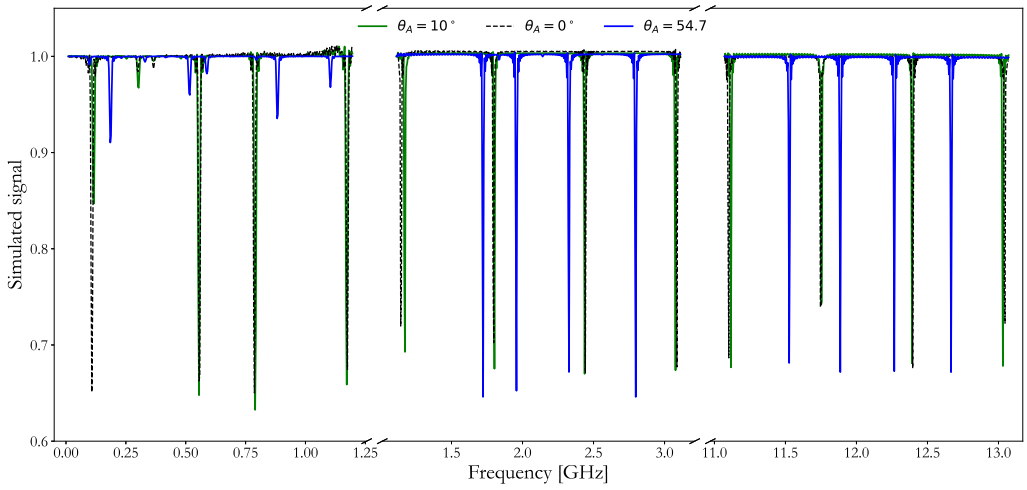

Figure 2.3: Simulated DEER frequency spectrum of an electron spin coupled to a copper nuclear spin with the hyperfine coupling matrix of the CuPc molecule as reported by Warner et al.[62]. The DEER spectrum was simulated at three different bias magnetic fields of 65 G (left), 700 G (middle), and 4000 G (right) and with three different angles between the magnetic field and the molecule $\hat{z}$ axis of 0° degrees (dashed black), 10° degrees (green) and 54.7° degrees (blue), as expected when the molecules are assembled flat on the diamond surface.

T_2, which is also on the order of microseconds, this method cannot be implemented effectively within the sequence.

These considerations show that the standard DEER pulse sequence is not well-

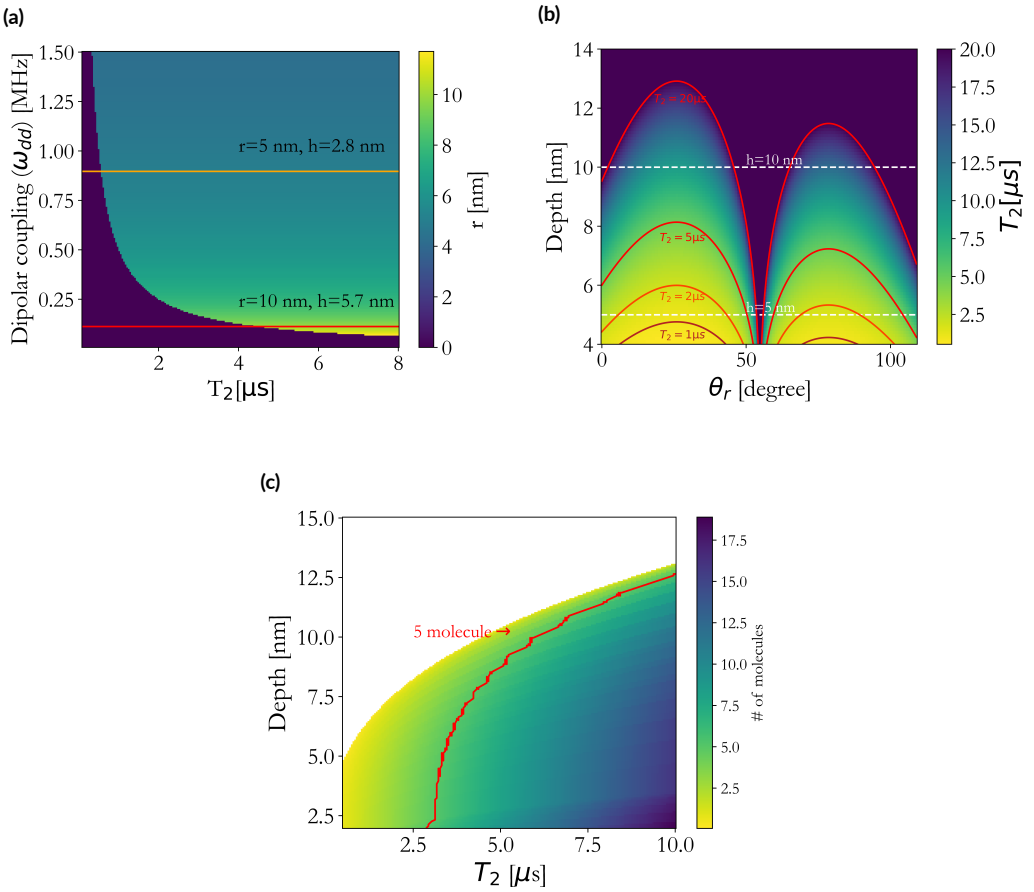

Figure 2.4: (a) 2D map of the maximal possible depth of the sensor that can detect an electron spin on the surface. The map calculates the depth for a range of the sensor coherence time T_2 and the dipolar coupling between the two, assuming the maximal frequency is given with $\theta_r = 0$. The red line indicates the depth of 5.7 nm where minimal coherence time of $\sim$ 5 µs is required, and the orange line indicates the depth of 2.8 nm. (b) 2D map of the minimal coherence time needed to detect an electron spin for a range of the NV center possible depth and the angle of the electron spin on the surface with respect to the NV center location (θ_r). The red lines indicate the coherence times of 1, 2, 5, and 20 µs where it can be realized that the sensing dome on the surface for an NV center at 10 nm and 5 µs is up to an angle of $\theta_r \sim 15^\circ$. (c) 2D map of the number of molecules with electron spin expected inside the sensing dome of the NV center for 10 % CuPc molecules and a 10 nm thick layer. The map calculates the number of molecules for a range of NV center depths and coherence times. A red line indicates the minimal depth and coherence time needed for at least five molecules in the hemisphere.

suited for this system. This challenge is addressed in the remainder of this chapter, where we propose a novel approach that enhances NV center sensitivity to complex spin systems like this one.

One more challenge that we address in this work is the trade-off between the NV center's coherence time (T_2) and the dipolar coupling strength (ω_{dd}), both influenced by the NV depth within the diamond. Dipolar coupling increases as the NV center moves closer to the surface, necessitating a shallow depth. However, shallower NV centers are more susceptible to surface noise, reducing their coherence time[92,13]. To illustrate this trade-off, Figure 2.4a presents a 2D map of the sensor's maximal depth for various dipolar coupling strengths and coherence times. The plot assumes the target spin is situated on the vector $\vec{r}$ which is of size $|r|$ from the sensor and on the same direction as the bias magnetic field in the system, meaning the depth (h) of the NV is $h = |r|cos(54.7$. The distance $|r|$ determines the maximal detectable dipolar frequency from surface spins at this depth. The figure highlights that lower dipolar frequencies correspond to deeper sensors, requiring longer coherence times. For instance, a 5.7 nm depth requires a coherence time of at least 4.38 µs, whereas a 2.8 nm depth necessitates 0.57 µs.

Figure 2.4b further explores this parameter space by mapping coherence time requirements for different sensor depths and angles (θ_r) of target spins on the surface. The depth and angle determine a hemisphere with radius r, which in turn defines the dipolar coupling strength and the minimal coherence time needed for detection. Red lines indicate coherence times of one, two, five, and twenty µs, outlining the feasible sensing range. For example, an NV center with a 1 µs coherence time cannot detect surface spins if deeper than 6 nm and is limited to a narrow sensing hemisphere at 5 nm depth.

This analysis emphasizes the narrow parameter space for detecting electron spins on the diamond surface. However, achieving this goal is possible by carefully optimizing experimental conditions. Another significant source of noise affecting T_2 is the ^{13}C nuclear spin bath within the diamond lattice, which remains similar for both shallow and deep NV centers. In this chapter, we introduce a novel technique to mitigate this noise source and extend the effective sensing volume.

2.2 Methods

Under the constraints and challenges presented above, we have carefully constructed an experiment that places CuPc under the spotlight. The experiment included sample

preparation consisting of well-characterized surface treatment, molecule deposition, surface analysis, and a carefully constructed pulse sequence for targeted magnetic sensing. Each part aims to address some of the challenges and criteria detailed above.

2.2.1 Sample preparation

Single-crystal diamond samples with shallow NV centers at average depths of 5 nm and 10 nm were used (for details on sample preparation, see Appendix A.3). To prolong the coherence time of these NV centers, all samples underwent a tri-acid boiling and oxygen annealing process [16]. The effectiveness of these treatments was optimized using X-ray photoelectron spectroscopy (XPS) and validated through Hahn echo measurements, as described in Appendix A.3.

CuPc and H_2Pc molecules were co-evaporated onto the cleaned diamond surfaces. To control the CuPc concentration, I first calibrated the evaporation rate of each molecule separately, using atomic force microscopy (AFM) scans to measure the layer thickness under different deposition conditions (Appendix A.3). The CuPc concentration in the evaporated layer is a crucial parameter, as it directly impacts both the coherence time of the NV sensor (T_2) and the relaxation time of the target spins (T_1)[62], both of which are essential for effective DEER sensing. Additionally, it determines the number of spins within the NV center's sensing volume. A lower CuPc concentration extends both T_1 and T_2 but decreases the likelihood of detecting a spin, while a higher concentration shortens T_1, making detection more challenging.

Considering these factors, we targeted a CuPc concentration of 10 % within the molecular layer. At this concentration, the T_1 of the molecular spins has been reported to be on the order of tens of µs (see Figure 2.1c). While a lower concentration could extend the relaxation time by three orders of magnitude, it would also reduce the probability of detecting any molecular spins. To estimate this probability, I calculated the expected number of spins within the NV center's sensing volume. This estimation was based on the hemispherical sensing region (Figure 2.4b), the molecular density of phthalocyanine, and the thickness of a 30 nm evaporated layer. Figure 2.4c shows the expected number of molecules at a 10 % CuPc concentration for various NV depths and coherence times (for full calculations, see Appendix B.2).

For a 5 nm deep NV center, a T_2 shorter than 2.5 µs results in fewer than five detectable spins on average. For a 10 nm deep NV center, a longer T_2 of approximately 7.5 µs is required. This analysis shows that a lower CuPc concentration of 1 % would render detection nearly impossible, while a higher concentration would reduce T_1, again preventing detection. The chosen 10 % concentration thus represents a narrow

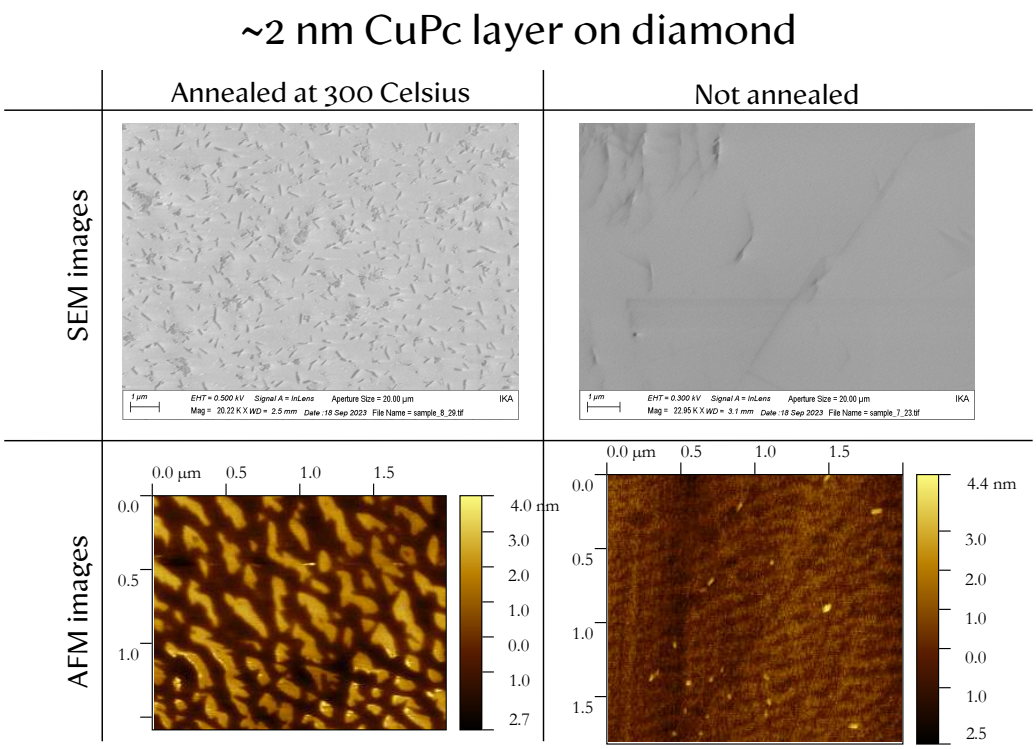

Figure 2.5: SEM and AFM images of a 2 nm thick layer of CuPc on the diamond surface. On the left, images were taken for a sample annealed at 300° degrees Celsius. On the right, images taken from a sample are not annealed.

but optimal window for magnetic sensing of molecular spins.

Beyond CuPc concentration, molecular orientation on the surface significantly impacts the expected magnetic spectrum variations. Previous studies have reported a phase transition in phthalocyanine layers upon annealing, leading to improved crystallinity[82]. To investigate this effect, two diamond samples with thick CuPc layers were prepared—one annealed at 300°C for one hour and one left unannealed. Surface characterization was performed using multiple techniques: AFM imaging, assisted by Dr. Sidney Cohen; SEM imaging, conducted by Dr. Ifat Kaplan-Ashiri; and X-ray diffraction (XRD) analysis by Dr. Anna Eden Kossoy to estimate molecular orientation.

AFM and SEM scans confirmed that annealing promotes crystal formation, leading to reduced surface coverage (Figure 2.5). Regardless, both annealed and non-annealed layers exhibited good alignment with the diamond surface (see Appendix A.3, with an estimated molecular tilt angle of $\theta_A \simeq 54.7°$ relative to the NV center axis. No single preferred angle was observed for the transverse orientation (φ_A), which was uniformly distributed. Given the molecule's high symmetry along the transverse axis, φ_A has min-

imal influence on the predicted eigenstates and energy levels of the target electron spin. These findings indicate that annealing is not a necessary step for achieving the desired molecular alignment on the surface.

2.2.2 Magnetic sensing

The DEER pulse sequence was employed as a guiding principle for sensing external electron spins while considering the aforementioned limitations. The primary challenge with the DEER pulse sequence is the narrow bandwidth of the microwave (MW) pulse used to target the spin and the limited time window within the sensor's T_2 to apply this pulse. Additionally, if the target spin's T_1 is shorter than the full sequence duration, it can further limit DEER effectiveness. However, using a low concentration of approximately $\sim 10\,\%$ allows for sequence durations extending to tens of microseconds, typically exceeding the sensor's T_2.

To overcome the narrow bandwidth of the MW pulse, we consider employing an adiabatic, also called chirp, pulse. The physics of adiabatic passage is thoroughly discussed in Chapter 3. In this section, I analyze the necessary chirped pulse parameters required to enhance the MW pulse's effect on the target spin. For a complete spin flip, the MW pulse must cover all possible resonance frequencies and sweep through them adiabatically, ensuring spin-state inversion from any initial eigenstate.

The resonance frequency range can span up to hundreds of MHz, particularly when accounting for the expected spin angle of $\theta_A = 54.7°$. Due to hardware constraints, we aim for a maximum frequency sweep width of 600 MHz. To evaluate the effectiveness of such a broad pulse, we compute the possible adiabaticity factors (Q) as they vary with pulse duration and frequency width (Equation 3.1a in Chapter 3). Figure 2.6a presents a map of the possible Q factors for a sensor with a 1 MHz Rabi frequency, consistent with the experiment in Subsection 2.3.3. The results indicate that achieving an adiabatic pulse width of 600 MHz necessitates a pulse duration of at least 4 µs. For most shallow NV centers, this duration exceeds their coherence time. Thus, I propose a modified approach: 'splitting' the DEER pulse sequence.

To apply the chirp pulse on the target spin without 'losing' sensor coherence, the sensor must be aligned along the $\hat{z}$ axis, where it primarily undergoes longitudinal T_1 relaxation, which is typically longer. However, along the $\hat{z}$ axis, the sensor is less sensitive to dipolar coupling with the target spin. Therefore, I propose a hybrid sequence incorporating both scenarios at different stages. The proposed sequence, illustrated in Figure 2.6b, begins like standard NV center sensing sequences, with an initialization green laser pulse followed by a $\pi/2$ pulse to place the sensor in a superposition state on

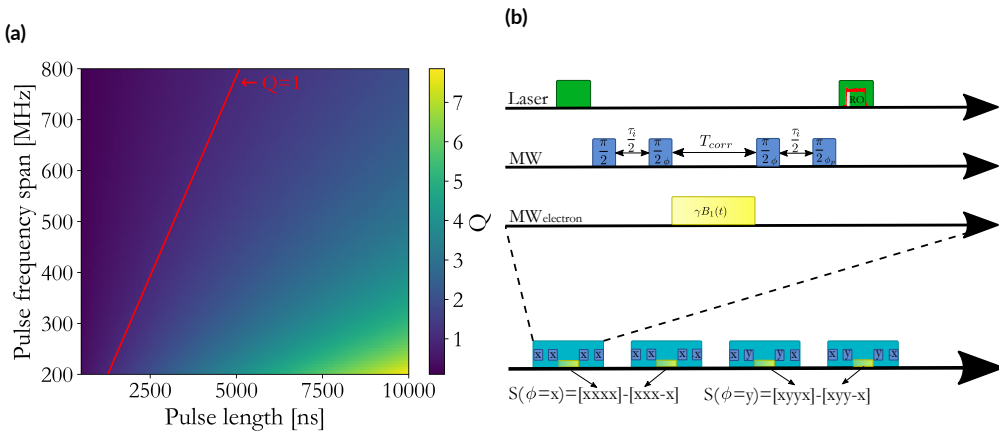

Figure 2.6: (a) 2D map of the adiabaticity factor of a chirp pulse for a range of pulse length and frequency span. (b) Illustrations of the Ramsey correlation pulse sequence (top). Green laser pulses are used to initialize and read out the spin state. Microwave pulses (blue) on the NV center resonance frequency are used to manipulate the sensor state, and a chirp MW pulse on the target electron resonance frequencies (yellow) is used to manipulate the electron state. The sequence is applied with four compositions of the MW pulse's phases illustrated at the bottom.

the Bloch sphere's transverse plane.

After initialization, the first sensing period of duration $\frac{\tau}{2}$ allows for DC magnetic field phase accumulation, denoted Φ_1. This phase accumulation concludes with the first $\frac{\pi}{2}_{\varphi}$ pulse (the second overall), which projects the sensor back onto the $\hat{z}$ axis, initiating the correlation period. The phase of this pulse φ is crucial for isolating interactions correlated with the sensor's coherence time, as elaborated later.

During the correlation period, indicated as T_{Corr}, the sensor, now aligned with $\hat{z}$, is insensitive to the target spin's interaction and unaffected by T_2 decoherence but relaxes with T_1. This period accommodates the long chirp pulse. The correlation period concludes with the second $\pi/2_{\varphi}$ pulse (third overall), transitioning the sequence into the second sensing period. As in the first sensing period, this second one lasts $\frac{\tau}{2}$, accumulating a phase proportional to the DC magnetic field, Φ_2. The final $\pi/2_{\mathrm{ro}}$ pulse projects the sensor back to the $\hat{z}$ axis for readout. This sequence, previously reported in EPR literature[93,94], was suggested theoretically for nuclear spin correlation[95]; however, it has never been experimentally applied with NV centers and was never utilized for electron spin sensing.

The two sensing periods function as Ramsey pulse sequences, making their accumulated phases proportional to the net DC magnetic field acting on the sensor. The DC field components include dipolar coupling to the target spin (ω_{dd}), MW detun-

ing (ΔB), hyperfine coupling (A^N), and slowly fluctuating noise (δB) (Equation 2.2a). Ideally, the accumulated phases in both periods should be identical ($\Phi_1 = \Phi_2$).

$$\Phi_1(\tau) = (\gamma \Delta B + \omega_{dd} + A^N + \gamma \delta B)\frac{\tau}{2} \tag{2.2a}$$

$$\begin{aligned} S(\tau, T_{\text{Corr}} = T_{Fix}) &= S(\varphi = x) - S(\varphi = y) \\ &= \cos(\Phi_1)\cos(\Phi_2) - (-\sin(\Phi_1)\sin(\Phi_2)) \\ &= \begin{array}{l} \frac{1}{2}\left[\cos(\Phi_1 + \Phi_2) + \cos(\Phi_1 - \Phi_2)\right] \\ +\frac{1}{2}\left[-\cos(\Phi_1 + \Phi_2) + \cos(\Phi_1 - \Phi_2)\right] \end{array} \\ &\simeq \text{Amp} \cdot \cos(\Phi_1 - \Phi_2) \end{aligned} \tag{2.2b}$$

If the DC interaction remains unchanged between sensing periods, phase subtraction results in zero. However, if magnetic fields change between periods, they persist upon subtraction. Specifically, an MW pulse flipping the target spin also flips its dipolar interaction with the sensor. Thus, all other phase terms cancel, leaving only the dipolar interaction component, expressed as $S(\tau, T_{\text{Corr}} = T_{\text{Fix}}) = A\cos(\omega_{dd}\tau)$. The extended correlation period accommodates a sufficiently wide chirp pulse, ensuring its impact is perfectly correlated between sensing periods.

Interestingly, the NV center's coherence time surpasses its T_2^* despite using Ramsey sensing periods. Ramsey coherence decay (T_2^*) arises from averaging phase accumulation over measurements. If the field is DC, phase accumulation remains consistent across iterations, producing oscillations. If the field fluctuates faster than measurement time, phase accumulation varies per iteration, contributing to signal averaging decay modeled by a Gaussian noise distribution (Equation 2.3). Intuitively, a longer interaction times amplify variance of the noise, thus accelerating decay.

$$S = \int e^{-\alpha(\delta B)^2}\cos(\gamma \delta B t) d\delta B = e^{-\frac{t^2}{4\alpha}} \tag{2.3}$$

While Ramsey decay stems from averaging, Hahn echo extends coherence by refocusing accumulated phase fluctuations. A similar effect occurs in the Ramsey correlation sequence for noise that fluctuates slower than a single iteration: noise-induced phase accumulation in the first period ($\Phi_1(\text{noise}) = \gamma \delta B \frac{\tau}{2}$) cancels with that of the second ($\Phi_2(\text{noise}) = \Phi_1(\text{noise})$) for the cosine component of subtracted phases (Appendix B.3)[95].

Noise fluctuating within T_{Corr} is denoted δB_{Corr}, while faster noise is δb. Evaluating their effects in Equation 2.2b shows correlated noise contributes only to summed

phases, while uncorrelated noise affects both terms. Since correlated noise is iteration-specific, it remains uncorrelated between x/y phase shifts, resulting in a noise-induced phase in the added phases term. Combining Equations 2.2b and 2.3, we derive the final expected signal (Equation 2.4a, full derivation in Appendix B.4).

$$\begin{aligned} S(\tau) &= \int e^{-\alpha_1(\delta b)^2} \left[S(\varphi = x) - S(\varphi = y)\right] d\delta b \\ &\simeq e^{-\frac{\tau^2}{4\alpha_1}} \cos(\omega_{dd}) \end{aligned} \tag{2.4a}$$

$$\begin{aligned} S(\tau) &= \int e^{-\alpha_2(\delta b + \delta B_{\text{Corr}})^2} \left[S(\varphi = x) + S(\varphi = y)\right] d(\delta b + \delta B_{\text{Corr}}) \\ &\simeq e^{-\frac{\tau^2}{\alpha_2}} \cos(\gamma B^{(0)} + A^N) \end{aligned} \tag{2.4b}$$

While the subtracted signal still decays due to uncorrelated noise between iterations, the decay is slower than a standard Ramsey signal (Equation 2.3), as correlation removes specific noise sources, which still affects the added signal. This enhanced coherence extends the detection window for the MSQ signal, as explored in Subsection 2.3.3.

2.3 Results

Based on the suggested pulse sequence, I have carried out a number of experiments, starting with simulations mimicking an NV center sensing a CuPc and a proof of concept using a room temperature measurement with an NV center coupled to an electron spin in the diamond lattice, and Finally with cryogenic measurements with shallow NV centers aiming to sense a thin layer of 10 % CuPc in a $\sim$ 30 nm thick H_2Pc layer. The results revealed the superiority of the method and some counterintuitive enhancement effects that will be discussed in Section 2.3.3.

2.3.1 Numerical simulations

Before experimentally applying the pulse sequence on an NV center, I conducted numerical simulations using the Python package QuTiP[96], which is designed for solving the time evolution of quantum systems. The first simulations focused on modeling an NV center (an electron spin with hyperfine coupling to a nitrogen nuclear spin) and a free electron spin positioned 5 nm away from the NV center. These simulations were employed to demonstrate the capability of the technique to distinguish between DC

magnetic fields, which are not induced by dipolar coupling to electrons, and electron spin dipolar coupling.

The time-domain simulation results are presented in Figure 2.7a, where two signals are plotted, corresponding to the two different phases ($\varphi = x/y$) with a readout phase of $\varphi_{\text{ro}} = x$. Subtracting the signals corresponding to different φ phases yields an oscillatory signal with a frequency of $\omega_{dd} = 828\,\text{kHz}$, as extracted from a fast Fourier transform (Figure 2.7b). This frequency aligns with the expected dipolar coupling signature of an electron spin located 5 nm away. Conversely, summing the signals from different φ phases results in another oscillatory signal with a frequency of $A^N = 3\,\text{MHz}$, which corresponds to the hyperfine coupling of the NV center to the nitrogen nuclear spin. This signal is also detected via Ramsey correlation since it originates from a DC magnetic field. These simulation results validate the theoretical framework discussed earlier and confirm the potential of the pulse sequence to detect dipolar coupling.

To further assess the method, I simulated the pulse sequence on a system with parameters mimicking those of CuPc. In this simulation, I modeled the NV center as an electron spin without the nitrogen nuclear spin to simplify computations. The CuPc molecule was represented as an electron spin coupled to a copper nuclear spin ($I = 3/2$) with the g factor and hyperfine coupling values reported by Warner et al.[62]. The strong hyperfine interaction necessitated the use of a broadband chirp pulse to fully invert the electron spin state. When the chirp pulse was optimized to cover all electron spin res-

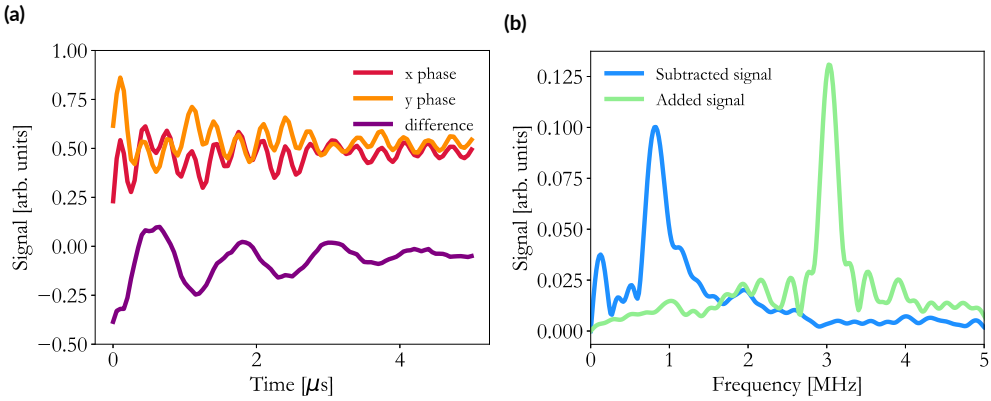

Figure 2.7: Simulation of the Ramsey correlation pulse sequence for a system of an NV center coupled to a 5 nm away electron spin. (a) Simulated $\varphi = x$ (red) and $\varphi = y$ (orange) signal of the Ramsey correlation sequence. Purple curve of the difference between the two signals. (b) A fast Fourier transform of the subtracted (blue) $\varphi = x$ and $\varphi = y$ simulated signals and summed (green) signal.

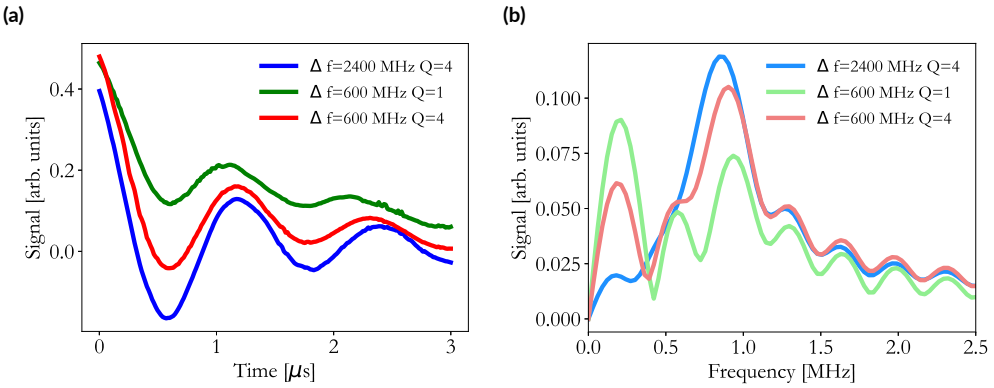

Figure 2.8: Simulation of the Ramsey correlation pulse sequence for a system of an NV center coupled to a 5 nm away electron spin coupled to a copper nuclear spin with hyperfine coupling of the CuPc molecule. (a) Subtracted Ramsey correlation signal for different simulated chirp pulses with different adiabaticity factors and span. (b) Fast Fourier transform of the simulated signals of (a).

onance frequencies (with a width of $\Delta F = 2.4\,\text{GHz}$ and $Q = 4$), a strong signal was obtained, as shown in Figure 2.8a. However, reducing either the frequency span or the adiabaticity factor led to a diminished dipolar coupling signal, as well as a weaker signal extracted via fast Fourier transform (Figure 2.8b).

These results underscore the necessity of using a sufficiently broad chirp pulse to encompass as many resonance frequencies as possible while maximizing adiabaticity. In practical applications, however, the achievable chirp pulse bandwidth and adiabaticity are constrained by the sensor and target electron spin's relaxation times, which were assumed to be on the order of tens of milliseconds in the simulation but are typically shorter in reality. Additionally, the simulation does not account for the complexity introduced by the nitrogen nuclear spins in the CuPc molecule. Consequently, in experimental conditions, the signal is expected to be further reduced due to the superposition of states arising from the misalignment of the molecular axis relative to the external magnetic field.

2.3.2 Room temperature proof of concept

To demonstrate the effectiveness of the proposed pulse sequence, I applied it to eight NV centers at room temperature. These NV centers were created through nitrogen ion implantation at an average depth of 10 nm in a single-crystal diamond (see Appendix A.3). Their coherence times ranged from 1 µs to 30 µs. A bias magnetic field of 350-450 G was applied. To evaluate the pulse's impact on free electron spins, I com-

pared results from Ramsey correlation measurements with standard DEER time measurements for each NV center.

Both detection methods aimed to identify electron spins in proximity to the sensor. In the DEER sequence, a MW π pulse addressed the electron spins, whereas the Ramsey correlation sequence employed a MW chirped pulse. Each scan was performed twice: first, with a MW pulse centered around the expected resonance frequency of an electron spin, calculated using the free electron gyromagnetic ratio and the NV center's ODMR-derived bias magnetic field; second, with no MW pulse during the corresponding time window. For clarity, scans with the MW pulse are referred to as 'on' pulses, and those without as 'off' pulses. The Ramsey correlation 'on' sequence used a MW chirp pulse with and a duration of 4 µs, resulting in a 25 MHz frequency span.

Seven out of the eight NV centers exhibited no oscillations, suggesting weak coupling to electron spins. However, weakly coupled electron spins are still expected within the lattice and on the surface. Therefore, a change in decay rates between the 'on' and 'off' cases was anticipated[51]. All datasets were fitted to an exponential decay function of the form $A \cdot \exp\left[-\left(\frac{\tau}{2T_d}\right)^2\right]$. The fitted decay time (T_d) was extracted, and the percentage change between 'on' and 'off' sequences was calculated as: $\Delta T_d[\%] = \frac{T_{d_{\text{off}}} - T_{d_{\text{on}}}}{T_{d_{\text{on}}}} 100$.

I compared the percentage change in decay time between the DEER and Ramsey correlation sequences in Figure 2.9a. The Ramsey correlation measurements (blue bars) consistently showed shorter decay times in all but one NV center when the MW pulse was 'on', indicating effective detection of NV center interactions with distant electron spins. In contrast, the DEER time measurements showed inconsistent results, with a pronounced reduction in decay time observed in only two NV centers. This does not necessarily imply that the DEER sequence is ineffective in detecting electron spins; rather, the π pulse used may be less effective in flipping electron spins compared to a chirped pulse.

The enhancement provided by a chirped pulse in a DEER sequence is explored separately in Chapter 3. For this chapter (2), I aim to demonstrate that the Ramsey correlation sequence can detect electron spins and measure dipolar coupling to a nearby electron spin. The distinction between a chirp pulse and a π pulse is irrelevant here (will be discussed in Chapter 3), as the chirp pulse is essential for addressing electron spins in the MSQ with a broad resonance spectrum.

Additionally, I analyzed an NV center exhibiting strong coupling to an electron spin in the diamond lattice, producing oscillations in the Ramsey correlation mea-

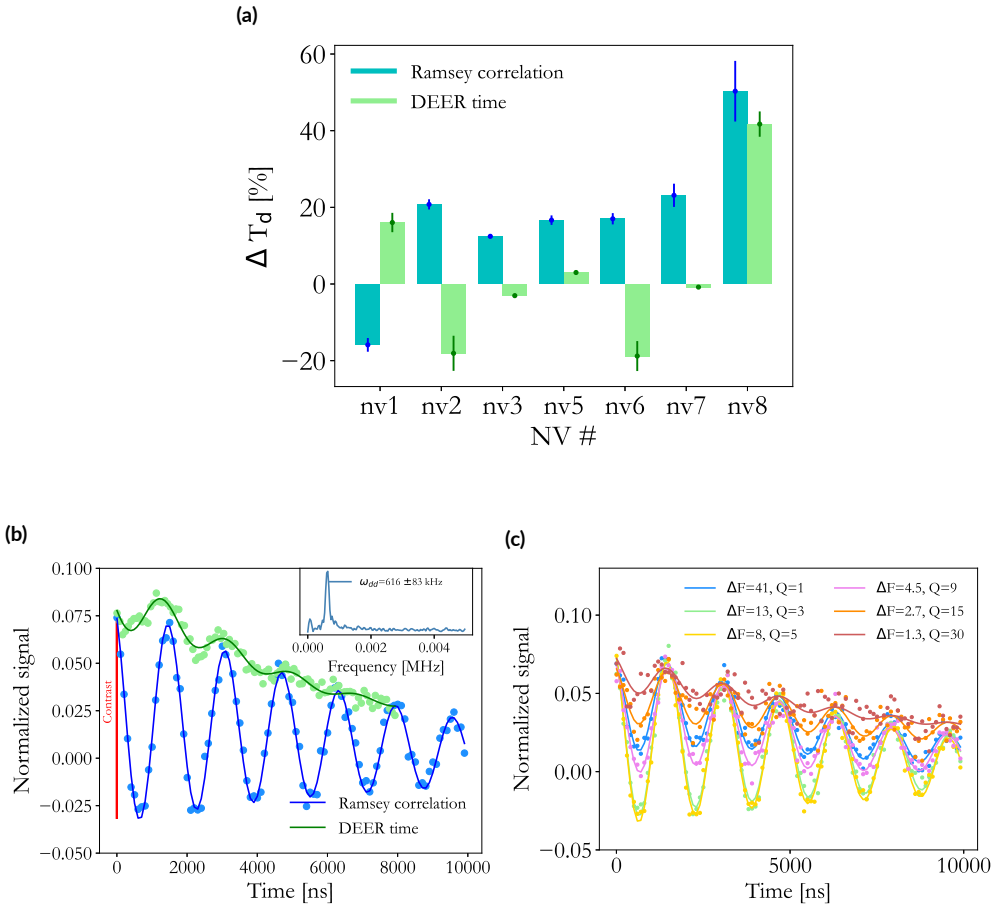

Figure 2.9: (a) Percent change of coherence time for eight NV centers between 'on' and 'off' pulses for the Ramsey correlation sequence (blue) and a DEER-time sequence (green). (b) Ramsey correlation signal (blue) and DEER time signal (green), both taken with a 2 µs long chirp pulse with Q=5, as detected from an NV center with a strong coupling to an electron spin. The inset shows the fast Fourier transform of the Ramsey correlation signal. (c) Ramsey correlation signals with a fixed duration of 2 µs chirp pulse and different adiabaticities as detected from the same NV-electron system reported in panel (b).

surement. A Ramsey correlation measurement with $Q = 5$ and a 2 µs pulse centered at 1.311 GHz under a 470 G magnetic field is shown in Figure 2.9b. The observed oscillations correspond to a dipolar coupling frequency of $\omega_{dd} = 616 \pm 1$ kHz, providing initial validation of the Ramsey correlation sequence for dipolar coupling sensing.

To compare the performance of Ramsey correlation with a DEER-time sequence, I applied a DEER sequence using a 2 µs pulse with adiabaticity of $Q = 5$ instead of a π pulse. The chirped pulse parameters yielded oscillations with a high contrast of

$C = 6\,\%$ of the normalized signal in the Ramsey correlation sequence (see Figure 2.9b for contrast definition). However, the DEER-time sequence produced oscillations at $\omega_{dd} = 0.6\,\mathrm{MHz}$ with a significantly lower contrast of $C = 1.4\,\%$ of the normalized signal (Figure 2.9b).

Given these findings, I further investigated the effect of chirp parameters on the Ramsey correlation signal. Figure 2.9c presents Ramsey correlation signals for a fixed pulse duration ($T_p = 2\,\mu\mathrm{s}$) with varying adiabaticity factors (Q). The highest dipolar coupling oscillation contrast, $C = 5.9 \pm 0.1\,\%$, was achieved with $Q = 5$. As Q was decreased (green and blue curves), the contrast also decreased, with $C = 3.2 \pm 0.1\,\%$ for $Q = 1$. This reduction was expected, as lower adiabaticity reduces pulse effectiveness.

Intuitively, increasing the adiabaticity factor should enhance contrast. However, as shown in Figure 2.9c, contrast decreased at higher values (pink, orange, and red curves). This effect arises because higher values reduce the total pulse span, thereby decreasing its effective range and spin-flipping efficiency.

The observed enhancement in Ramsey correlation measurements may stem from two factors, though further experiments are needed for confirmation. First, in the DEER sequence, the chirped pulse is applied while the NV center is in a superposition state, making it more sensitive to magnetic fields. Consequently, the pulse may introduce noise, reducing sensitivity to coherent effects. To test this, similar pulses could be applied during both sensing periods of the Ramsey correlation sequence but at off-resonance frequencies. If the pulse interacts with the NV center as noise, it should also degrade the Ramsey correlation signal.

Second, noise sources correlated with the Ramsey correlation timescale may have less impact on its signal, thereby extending coherence time (see Section 2.6). Reducing certain noise sources could enhance sensor sensitivity for detecting weak magnetic fields. For instance, ^{13}C atoms in the lattice precess at the Larmor frequency, which could introduce noise unless it is correlated with the two sensing periods, leading to refocusing. This hypothesis is supported by low-temperature system measurements, elaborated in Subsection 2.3.3. Nevertheless, further experiments are necessary to explore the effect of modifying the Ramsey correlation sequence's correlation time.

2.3.3 Results from measurements at cryogenic temperatures

The goal of this research was to use the NV center to sense MSQs. For this purpose, I utilized a diamond single crystal sample with nitrogen atoms implanted to an average depth of 5 nm (see Appendix A.3). The sample was cleaned using tri-acid boiling before undergoing oxygen annealing, and it was placed inside an ultra-high vacuum

chamber immediately after the cleaning process. CuPc molecules were co-evaporated with H_2Pc molecules, resulting in a 10 % concentration of spin-containing molecules within a $\sim$ 30 nm thick molecular layer. The sample was then scanned at a temperature of 5 K to ensure the long relaxation time (T_1) of the CuPc electron spin, and it was maintained under ultra-high vacuum conditions to ensure stability and reduce molecular diffusion. The low-temperature confocal setup provides a narrow range of magnetic fields (see Appendix A.1). Consequently, scans were performed with a bias magnetic field of 64.3 ± 0.1 G. In total, five NV centers were scanned, one of which exhibited a number of interesting effects that will be introduced and analyzed in this section.

The expected magnetic resonance spectrum of the CuPc electron spin at a $\sim$ 65 G magnetic field is shown in Figure 2.2a. Based on this spectrum, I chose to use chirp pulses centered around 600 MHz to address the CuPc electron spin, and a pulse centered around 1600 MHz for off-resonance driving in control measurements. A comparison of a Ramsey correlation measurement, one on-resonance and one off-resonance, is plotted in Figure 2.10a.

This result reveals two notable features. First, the off-resonance signal shows a coherence time of $T_2 = 5.5 \pm 1.3$ µs, which is longer than the T_2 of the sensor ($T_2 = 3.6 \pm 0.1$ µs). Second, the on-resonance data exhibit a faster decay rate of $T_2 = 4.2 \pm 0.5$ µs, shorter than the off-resonance decay. Similar to the room-temperature results, this suggests that the electron spin of the molecule was addressed and flipped. Assuming that the NV center is probably coupled to a single MSQ, as suggested by the analysis in Figure 2.4c, the signal from the on-resonance sequence behaves like a decaying sine function.

To extract the dipolar coupling between the NV center and the MSQ electron spin, I simultaneously fitted the on- and off-resonance signals with an exponential decay for the off-resonance signal and an exponential decaying sine with the same decay time for the on-resonance signal. The fitted decay time was $T_2 = 4.8 \pm 0.5$ µs, and the dipolar coupling was $\omega_{dd} = 365.5 \pm 7.6$ kHz. However, since the chirp pulse does not cover the full spectrum of the molecule, it may reduce the contrast, which is already low, and potentially mask the real frequency in the noise of the measurement.

These two immediate features mentioned above call for further experiments, which will be discussed in the remainder of this chapter. First, additional data would provide insight into the prolonged coherence and help build a theoretical framework to explain it. Second, further experiments are needed to verify the assumption of coupling to an MSQ on the surface.

I will first focus on the gain of coherence observed after the sensor's typical decoherence time, T_2. The coherence gain somewhat resembles coherence times longer than T_2^*, even though the sensing period is based on a Ramsey sequence. In a Ramsey correlation, the phase accumulated due to noise during the first sensing period is refocused

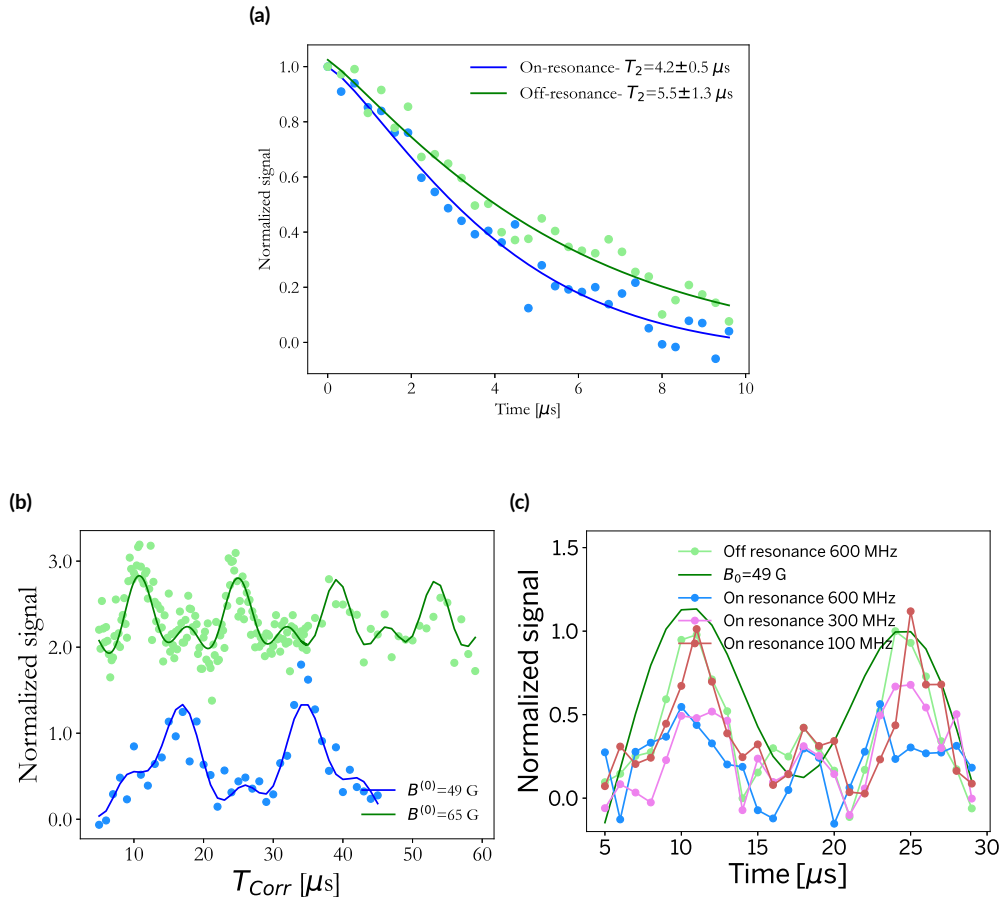

Figure 2.10: Ramsey correlation measurements taken from a single NV center with T_2 =3.6 μs (a) Ramsey correlation signals taken with a correlation time of 10 μs and chirp pulse span of 600 MHz applied on-resonance (blue) and off-resonance (green) the CuPc resonance spectrum. (b) Ramsey correlation signals with fixed sensing time τ=6 μs, changing correlation time, and no chirp pulse taken with a 64.3±0.1 G field (green) and 49.5±0.3 G field. Both show oscillations at the frequency of the carbon nuclear spin Larmor frequency. (c) Ramsey correlation signal with a fixed sensing time, changing correlation time, and a chirp pulse with difference spans. Each plot of a different span is plotted with a vertical shift for a clearer view. The signal detected with a narrow span of 100 MHz (red) shows a similar signal as detected with an off-resonance (green) pulse of strong oscillations at the frequency of the carbon nuclear spin Larmor frequency. The signal detected with a broad on-resonance 600 MHz and 300 MHz show a reduction of the contrast of the oscillations.

in the second period, provided that the noise's typical fluctuation time is comparable to a dingle iteration timescale. This suggests that there may be a noise source that is refocused in the correlation timescale but not during the sensor's T_2 time. To test this, I measured the sensor's signal with a fixed sensing time $\frac{\tau}{2} = 3\,\mu s$ and varying correlation time (T_{Corr}), starting from a correlation time longer than the sensor's T_2 to avoid residual signals remaining on the equator after the correlation period, with no pulse applied to the target electron spin during the correlation period.

The results of this measurement are shown in Figure 2.10b. The green curve corresponds to scans taken under a magnetic field of $64.3 \pm 0.1\,G$, and the blue curve corresponds to scans taken under a magnetic field of $49.5 \pm 0.2\,G$. The green curve shows revivals of the signal at four correlation times. A fit to the function in Equation 2.5 reveals oscillations at frequencies of $\frac{\omega_1}{2\pi} = 71.4 \pm 1.1\,kHz$ and $\frac{\omega_2}{2\pi} = 140.5 \pm 1.3\,kHz$. The lower frequency, ω_1, is similar to the expected Larmor frequency of ^{13}C nuclear spins in the lattice: $\omega_{^{13}C}(B^{(0)} = 64.3\,G) = 68.8 \pm 0.1\,kHz$.

$$S = \text{amp} \cdot \exp(-(^{T_{Corr}}/_{\Gamma})^{\beta}) \cdot (c_1 \cdot \cos(\omega_1 T_{Corr} + \theta_1) + c_2 \cdot \cos(\omega_2 T_{Corr} + \theta_2)) \qquad (2.5)$$

The carbon nuclear spins precess at their Larmor frequency, f_C, and this precession is detected by the NV center as an AC magnetic field with a period T_C. Typically, the Larmor period T_C is slower than the typical time of a single measurement iteration, meaning that the AC signal does not complete a full cycle during one iteration. Since the iterations are not synchronized with the Larmor frequency, the phase accumulated from Larmor precession differs for each iteration and adds noise to the averaged signal.

In a Ramsey sequence, these AC fields introduce noise through averaging, and in dynamical decoupling sequences such as Hahn echo, the AC fields can be detected at specific interaction times of $\frac{\tau}{2} = nT_C$, which are correlated with the Larmor period, leading to coherent phase accumulation[41,97]. If the sensor's T_2 is shorter than the carbon nuclear spin's Larmor period, this AC precession is uncorrelated with the sensing period, adding noise to the averaged signal.

However, the AC field from carbon nuclear spins acts as correlated noise in the Ramsey correlation sequence when the correlation time equals the carbon nuclear spin Larmor period ($T_{Corr} = nT_C$)[97]. Following the theoretical framework outlined in Section 2.2, we can treat f_C as a correlated magnetic noise, δB_{Corr}. By removing some noise sources, we can narrow the noise distribution and prolong the decay constant. This insight helps explain the revival of the signal observed at correlation times fitted

to the carbon's nuclear spin Larmor frequency.

To understand the signal shape and the function fitted to it in Equation 2.5, we use the same derivation of the pulse sequence (Appendix B.3) and treat T_{Corr} as the changing variable instead of τ. The signal measured during the first interaction period, due to the carbon nuclear spins' Larmor frequency, is $\cos\left(f_{\mathrm{C}}\frac{\tau}{2}\right)$ when τ is fixed, ignoring any other DC magnetic field (which has been treated separately). The signal during the second interaction period would be $\cos\left(f_{\mathrm{C}}\frac{\tau}{2}+f_{\mathrm{C}}T_{\mathrm{Corr}}\right)$ when T_{Corr} changes, effectively adding a relative phase to the signal. Subtracting the two signals ($\varphi = x/y$) results in oscillations at the frequency of f_{C} in T_{Corr} (see Appendix B.4)[95].

The detected signal oscillates at two frequencies, with the first matching the Larmor frequency of the carbon nuclear spins. To further support the idea that coherence gain arises from correlation with the carbon nuclear spins' Larmor frequency, I scanned the same NV center under a lower magnetic field, expecting to detect revivals at a frequency corresponding to the relevant Larmor frequency. In Figure 2.10b, the blue curve shows the signal and fit for measurements taken under a field of $B^{(0)} = 49.5 \pm 0.2\,\mathrm{G}$, with revivals at a frequency of $\omega_1 = 53.2 \pm 1.6\,\mathrm{kHz}$, which matches the expected Larmor frequency of the carbon nuclear spin, $\omega_{^{13}C}(B^{(0)} = 49\,\mathrm{G}) = 52.9 \pm 0.2\,\mathrm{kHz}$. The second frequency detected at this field was $\omega_2 = 116.8 \pm 2.9\,\mathrm{kHz}$.

The second frequency I detected with both bias magnetic fields is approximately twice as fast as the ^{13}C Larmor frequency. We attribute this to an inherent spurious effect of the correlation sequence, allowing for correlation also with half the Larmor frequency period[98]. We note that detection of the carbon nuclear spin Larmor frequency was reported before with a Hahn echo correlation sensing sequence. However, it was reported that the signal can not be detected when the bias magnetic field is smaller than 110 G while this regime is detected with the Ramsey correlation sequence[99].

Finally, I leveraged the prolonged coherence time of the sensor at correlation times matching the ^{13}C Larmor frequency period to widen the observation window for dipolar coupling to external electron fields. Figure 2.10c presents data collected from the same sensor under a magnetic field of 64.3 G, with a chirp pulse applied during the correlation time. The figure shows four cases all fitted to Equation 2.5. All four signals were taken with an adiabaticity factor of 2 and varying pulse frequency spans. The Q factor and span determine the pulse duration; thus, for pulses shorter than the correlation time, the pulse was applied in the middle of the correlation period, leaving the rest without external intervention.

The green and blue curves in Figure 2.10c show signals taken with a chirp pulse of 600 MHz width. The green curve was taken off-resonance from the molecular mag-

netic spectrum, while the blue curve was on-resonance. The green curve shows a full revival of coherence at the correlation times of the carbon nuclear spins' Larmor frequency with a fitted oscillation amplitude of $c_1 = 0.28 \pm 0.03$ for the fitted frequency $\omega_1 = 70.8 \pm 2.5\,\text{kHz}$, while the blue curve shows minimal revival with a fitted oscillation amplitude of $c_1 = 0.16 \pm 0.05$ for the fitted frequency $\omega_1 = 72.1 \pm 6.8\,\text{kHz}$. This suggests that the chirp pulse flipped the CuPc electron spin state, as expected. However, further measurements are needed to confirm or disprove this theory.

I also measured the Ramsey correlation sequence with different chirped pulse spans, expecting a gradual recovery of the signal at the carbon correlation times as the span narrows. A narrower chirped span would address less of the molecule's resonance frequency spectrum and reduce the probability of flipping the state. Figure 2.10c presents two additional curves: a red curve for a 100 MHz span showing almost a full signal recovery with fitted oscillation amplitude of $c_1 = 0.23 \pm 0.05$ for the fitted frequency $\omega_1 = 68.7 \pm 4.5\,\text{kHz}$, and a pink curve for a 300 MHz span showing a reduced signal fitted oscillation amplitude of $c_1 = 0.20 \pm 0.04$ for the fitted frequency $\omega_1 = 73.4 \pm 5.3\,\text{kHz}$. The gradual change in amplitude confirms the assumption that the signal rises from the driving of the MSQ electron spin.

Further work can be done to add insight into the technique's capabilities. For instance, measurements at higher magnetic fields could be conducted where the CuPc electron spin eigenstates are no longer at superposition states, allowing better control. The main challenge of scanning at higher fields is that the carbon nuclear spin Larmor frequency becomes too high, and the correlation time would be too short. Another possibility is scanning at lower magnetic fields, where the eigenstates would align with the molecule's $\hat{z}$ axis, and the correlation time would be sufficiently long to apply the chirp pulse.

2.4 Discussion

Molecular spin qubits are promising candidates for quantum technologies. Due to the diversity that the chemical playground offers, these molecules can be engineered and modified to the needs of the system [56,55]. Still, this field has a variety of challenges to overcome and a wide spectrum of unanswered questions. One challenge is to be able to control the MSQ as a single qubit and, even before that, the ability to examine and investigate a single MSQ's properties. In this research, we set a target to tackle this challenge using the NV center while pushing the NV center's abilities as a magnetic sensor to its limits.

We established a set of requirements from the MSQ, considering the surface of the diamond as the substrate holding the molecules and the Hamiltonian of the MSQ electron spin, which defines its magnetic spectrum - all of this while considering the possibility of using the MSQ and the NV center in a hybrid quantum system. The chosen MSQ was copper phthalocyanine, which answered most of the requirements related to the diamond surface and some related to the spin Hamiltonian. Theoretical analysis based on published literature [62] and numerical analysis revealed the challenges of sensing these molecules and the obstacles in making it part of a hybrid system with the NV center.

Nevertheless, we used the molecule as a target for quantum magnetic sensing, with the NV center focusing on utilizing techniques that can offer sensing of complex systems such as MSQs. I proposed a pulse sequence, Ramsey correlation, that can offer sensitivity to electron spins with a broad magnetic spectrum. Theoretical analysis of the pulse sequence showed the benefit it can offer in gaining longer coherence time, overcoming the T_2^* limit of a Ramsey pulse sequence and even the T_2 limit of Hahn echo at specific correlation times while still offering sensitivity to DC magnetic fields.

In addition to the prolonged coherence, the pulse sequence offers a wide time window for applying a driving pulse addressed to the target electron spin. I utilized this window to apply a long adiabatic MW pulse addressing a large part of the electron magnetic resonance spectrum. Numerical simulations of the NV center with a strong dipolar coupling to a system mimicking a CuPc electron spin showed the success of the pulse sequence and the effect of the chirped pulse width on the resulting signal.

I have successfully shown the detection of dipolar coupling to an electron spin using the Ramsey correlation pulse sequence and compared the Ramsey correlation to the well-known and used DEER-time sequence, thereby showing the superiority of the pulse sequence in detecting the dipolar coupling. Finally, I used the pulse sequence on a sample with a thin and diluted layer of CuPc molecules on the surface of the diamond. I showed the use of the pulse sequence to prolong the coherence time of the NV center by refocusing the noise caused by the carbon nuclear spins and then utilized this phenomenon to show the first indication of dipolar coupling between the NV center and a CuPc electron spins.

The results presented in this chapter are the first step toward quantum magnetic sensing of a single MSQ. Promising as they may be, there are still a number of experiments required to prove convincingly that the signal detected is coming from an MSQ. On top of the experiments suggested in the results section, we also suggest considering other MSQs with a lower hyperfine coupling to the metal atom nuclear spin, such as

metallodithiolene[100].

Finally, considering the motivation of this research, building a hybrid quantum system of the NV center and a single MSQ, even overcoming the challenges or utilizing the suggested pulse sequence, would not suffice. To establish a quantum communication channel between the NV center and the MSQ, the MSQ spin state should be first initialized. This work began with the proposal of using the high-fidelity initialization of the NV center to initialize the MSQ spin with polarization transfer[101]. However, considering the spectral limitations, this approach is not relevant.

Not relinquishing the end goal, another method to initialize the spin is using a low temperature and high magnetic field. A simple calculation based on Boltzmann distribution should estimate the target temperature and field to achieve any polarization. The probability ratio between two states of a spin according to the Boltzmann distribution is $\frac{p_i}{p_j} = \exp\left(\frac{\varepsilon_j - \varepsilon_i}{kT}\right)$, where p_i and p_j are the probabilities of the states to be occupied, $\varepsilon_i - \varepsilon_j$ is the energy gap between the states and kT is the temperature and the Boltzmann factor. For an electron spin to be 90% polarized to one state at 5 K, an eight-Tesla magnetic field is needed. If using a 0.1 K cryogenic system, the magnetic field can be around 0.1 T.

"Nature is pleased with simplicity. And nature is no dummy."

Sir Issac Newton

3

Sensitivity enhancement with chirped pulses

Adiabatic pulses offer a robust control over spin states and open the possibility to operate a realistic system when theory meets the noise and inhomogeneity of the real world [102,103,104]. As the primary goal of this research is to push the NV center magnetic sensor to its limits, allowing the sensing of complex molecules, we look to exploit any method that might offer more sensing possibilities. This chapter examines the benefit of using adiabatic pulses in a simple DEER pulse sequence. I present an experimental setup where adiabatic pulses could benefit dipolar coupling sensing. I discuss the theoretical background and working mechanism of an adiabatic pulse on a quantum system, and I showcase results of DEER measurements on NV centers comparing the adiabatic pulse effectiveness to that of a π pulse.

3.1 Background

Classical magnetic resonance worlds such as NMR and EPR use adiabatic pulses to overcome the inhomogeneity of the magnetic field [102,105,106]. Adiabatic pulses create a slow change in the driving frequency or the driving amplitude from one side of the resonance frequency to the other such that the rotation of the spin state is insensitive to

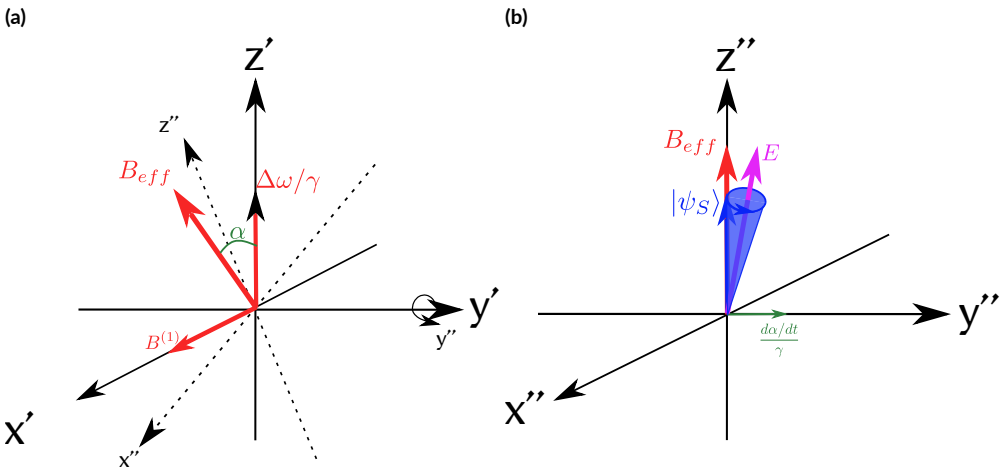

Figure 3.1: (a) Axis system of the rotating frame, which rotates around $\hat{z}$ axis in the lab frame and with the NV center at its resonance frequency. The driving magnetic field $B^{(1)}$ of the chirp pulse is along $\hat{x}'$ axis with an element of $\frac{\Delta\omega}{\gamma}$ along $\hat{z}'$ axis due to the off-resonance driving of the chirp. The effective field is the sum of both fields. (b) Double rotating frame, which rotates around the B_{eff} field. The spin state rotates around the effective E field as it is rotating with the B_{eff} field towards the $-\hat{z}''$ axis [102].

changes in the driving field $B^{(1)}$. Similarly, spins detuned from the resonance frequency due to $B^{(0)}$ inhomogeneity but still within the frequency sweep are rotating with high robustness against magnetic field imperfections. For NV centers, the detuning from the resonance frequency can result from hyperfine coupling to carbon nuclear spins in the lattice, dipolar coupling to strongly coupled electrons, or from strain in the lattice in nanodiamonds [107]. However, the adiabatic driving method can still hold, no matter the source of detuning.

Understanding the adiabatic pulse mechanism requires us to look at the rotating frame. The on-resonance driving field introduced in Equation 1.3b is stationary in the rotating frame pointing on the $\hat{x}'$ axis. When this field includes a time-varying frequency $F(t) = \omega_0 + \delta\omega(t)$ the detuning from resonance - $\Delta\omega(t = \tau) = \delta\omega(\tau)$ is effectively adding a magnetic field in the $\hat{z}'$ axis in the rotating frame with magnitude proportional to $\Delta\omega/\gamma$ (see Figure 3.1a). These two fields add up to an effective magnetic field in the rotating frame B_{eff} with an angle α that is changing as $\Delta\omega$ is changing in time.

To understand what happens to the spin, we move to a rotating frame that is rotating with B_{eff} as illustrated in Figure 3.1b. The effective magnetic field in this picture is always along $\hat{z}''$ axis, and a small field of the frequency change rate $d\alpha/dt$ is added along

the $\hat{y}''$ axis. Together, the magnetic field in the double-rotating frame is E. Any spin component that is starting the pulse pointing along $\hat{z}''$ will rotate around E. If the pulse is adiabatic, the rate of frequency change $d\alpha/dt$ is small, creating a small cone shape of rotation of the spin state around E. In the rotating picture, it will present itself as a spin state that is rotating in small circles tangent to B_{eff} that keep rotating from $\hat{z}'$ to $\hat{x}'$. B_{eff} will point in $\hat{x}'$ axis once $\Delta\omega = 0$ and keep rotating towards $-\hat{z}'$, taking with it the spin state.

Adiabatic pulses, also known as chirp pulses, can be quantified by the adiabaticity factor Q (Equation 3.1a). A high adiabaticity factor indicates that the rate of change $d\alpha/dt$ is small enough compared to the effective field $\omega_{\text{eff}} = B_{\text{eff}}/\gamma$, therefore, the change is slow. The minimal adiabaticity factor can be found when the driving frequency approaches resonance, the effective field is minimal, and the rate of frequency change is maximal. At this point, it is also possible to relate the adiabaticity factor to the system parameters of Rabi frequency (ν), frequency span of the sweep (ΔF), and the pulse time (t_p), which results in the term written in Equation 3.1b (for a full derivation see Appendix D.1).

$$Q = \frac{\omega_{\text{eff}}(t)}{d\alpha/dt} \tag{3.1a}$$

$$Q_{min} = \frac{2\pi\nu^2 t_p}{\Delta F} \gg 1 \tag{3.1b}$$

For simplicity, in most cases, the spin states will be along the $\hat{z}$ axis in the lab frame, which is aligned with the $\hat{z}'$ axis in the rotating frame. Therefore, under an adiabatic pulse, the spin will rotate together with B_{eff}. The degree of rotation depends on the frequency change across the adiabatic pulse. A full-passage will have a similar frequency change before and after achieving resonance, whereas a half-passage will stop once reaching resonance. The full-passage can create a π rotation, while the half-passage will cause a $\pi/2$ rotation [102].

Adiabatic pulses, also known as chirp pulses, are used in the NV center sensing community mostly with nano-diamonds [107] and NV ensembles [108] where NV centers can deviate from the main resonance frequency due to some interaction with the environment. The chirp pulses in these cases allow us to work with a number of NVs without the effect of some NVs' imperfect driving. When working with single NV centers in a bulk diamond, a working frequency can be perfectly fitted to the NV center in focus. Therefore, a chirp pulse might not add to the final result for better control of the sensor driving.

Nevertheless, even with a single resonance frequency, MW interaction with the NV center may be suboptimal, leading to incomplete driving, especially when the MW source is distant or attenuated at certain frequencies. This reduces the driving frequency or Rabi power, resulting in a long, narrowband pulse.

For instance, a π pulse, defined as $B^{(1)} = \cos(\omega_{\mathrm{MW}} t)\mathrm{Rect}(t - t_p)$), transforms into a sinc function in the Fourier domain with a width of $1/t_p$. A low Rabi frequency lengthens the π pulse duration, $t_p = 1/2\nu$, narrowing the bandwidth and making the system more sensitive to noise.

This issue is more pronounced in electron spin driving. When using the NV center as a magnetic sensor, uncertainties in spin resonance frequency and weak MW coupling reduce electron spin driving efficiency. The DEER pulse sequence requires full spin flipping, but low efficiency causes partial flipping and weakens the DEER signal. The signal of a DEER pulse sequence has many parameters affecting it; some are controllable, such as the interaction time, and some are system-dependent, such as the dipolar coupling. Consequently, utilizing an MW pulse that can eliminate the uncertainty in the flipping efficiency of the electron spins can improve the possible result of the signal.

In the rest of this chapter, I will showcase the benefits of using adiabatic pulses. I will start with a proof of concept on the NV center contrast and then showcase the results of an experiment comparing the DEER results between π pulse driving and adiabatic driving of electron spins.

3.2 Signal enhancement with chirp pulses

Before utilizing the chirp pulses on a complex pulse sequence like the DEER, I tested the chirp pulse on an NV center with the purpose of confirming the pulse function and efficiency. An ODMR pulse sequence was applied to an NV center situated in a bulk diamond with an average implantation depth of 10 nm. The Rabi frequency of the target NV center was 1 MHz. Therefore, a π pulse on the NV center had a width of ~ 2 MHz. A "regular" ODMR sequence with a π pulse on the NV center (blue curve on the left figure of Figure 3.2a) showed a clear resonance frequency in 1.508 GHz with a width of 2.1 ± 0.1 MHz, broadening caused by the short T_2^* of the NV center. The contrast of the signal was $17.2 \pm 0.6\%$.

To confirm the functionality of the chirp pulse, I applied the ODMR pulse sequence with a chirp pulse with a span of ~ 10 MHz instead of the π pulse with three different Q factors of 0.5, 1, 2 (purple red and green curves respectively in the left plot

in Figure 3.2a). The results of all ODMR measurements showed a signal of two Gaussian functions, separated by $\sim$ 5 MHz and with a width of $\sim$ 5 MHz each, resulting in a total of $\sim$ 10 MHz width around 1.508 GHz, and confirming the pulse does function as expected.

The efficiency of the pulses can be scaled by the signal contrast of the measurements, which was $25.6 \pm 0.6\%$ for $Q = 2$, $20.3 \pm 0.5\%$ for $Q = 1$, and $14.1 \pm 0.4\%$ for $Q = 0.5$ (left plot in Figure 3.2a). It is clear that a pulse with a higher Q factor enhances the contrast of the signal. However, increasing the adiabaticity factor of the pulse is not enough; the pulse's width also has to be wide enough to address the energy transition, especially if the transition is broadened due to the decoherence of the sensor.

The middle plot in Figure 3.2a shows the signal of three chirp pulses with a fixed duration of 1 µs and different Q factors. The highest Q factor of 2 (green curve) has a narrow span of 2.4 MHz and, therefore, shows a reduction in contrast to $16.7 \pm 0.5\%$ compared to the $Q = 1$ curve (red) with a span of 4.8 MHz and contrast $21.7 \pm 0.4\%$. As expected, the $Q = 0.5$ signal (purple) shows the lowest contrast with the broadest signal.

To complete the picture of the efficiency of chirped pulses, I plotted the ODMR signals of three measurements taken with different adiabaticity factors but with a constant span (Figure 3.2a). The span of all pulses was 2.4 MHz, the contrast is improving as the adiabaticity factor is higher, and the best contrast with a span of 2.4 MHz was detected with the $Q = 3$ curve (green). Nevertheless, the best contrast overall was with a broad pulse of $\Delta f \simeq 10$ MHz and $Q = 2$. We attributed this to the pulse addressing both resonance transitions of the nitrogen nuclear spin (separated by $\sim$ 3 MHz, see Section 1.2.3), therefore enhancing the contrast by driving both at the same time and strength, as expected from the chirp pulse.

After I established the chirp pulse functionality and contrast enhancement with the NV center, I used it to check the possible advantage it can bring in electron spin sensing. I have examined four NV centers in a bulk diamond with nitrogen atoms implanted at an average depth of 10 nm. To remove organic residues, the diamond was cleaned with a tri-acid boiling (see Appendix A.3). All examined NVs had a T_2 longer than 10 µs to ensure surface sensitivity (see sensing volume analysis in Appendix B.2).

Each of the NV centers was scanned four times. First, I applied a DEER-frequency and a DEER-time with a π pulse addressing the electron spins, where the pulse duration was estimated from the NV center Rabi frequency. Second, I applied again the DEER-frequency and DEER-time changing the π pulse to a chirped pulse addressing the electron spins. To make the signals comparable, I have used a chirp pulse with a

Q factor of five and duration of 1.6 µs that resulted in a chirp span of 2.5 MHz where the spectral width of the π pulse was 2.2 MHz.

Results of the DEER-frequency scans are plotted in Figure 3.2b. All scanned data were fitted to a single Gaussian function to estimate the contrast of the DEER signal. The contrast of each scan is written next to the data and fit plotted in Figure 3.2b.

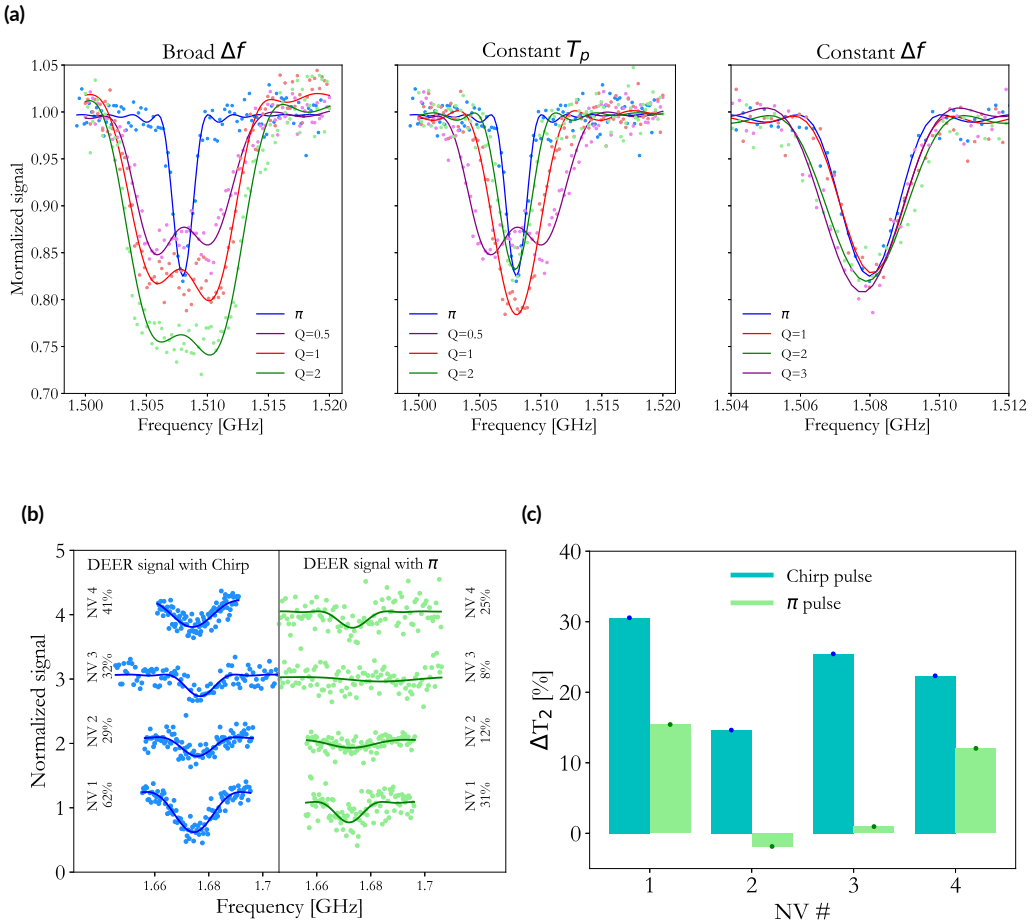

Figure 3.2: (a) ODMR signals from an NV center with a chirp MW pulse with different parameters. The left plot shows the signal for a broad span chirp of ∼10 MHz with Q=0.5/1/2 (purple, red, and green, respectively) compared to a π pulse (blue). The middle plot shows the signal for chirp pulses with a constant duration of 1 µs and different adiabaticity of Q=0.5/1/2 (purple, red, and green, respectively). The right plot shows the signal for chirp pulses with a fixed narrow span of 2.4 MHz and different adiabaticity of Q=1/2/3 (red, green, and purple, respectively). (b) DEER-frequency signal from four NV centers taken with a chirp pulse (left curves in blue) and with a π pulse (right curves in green). For clarity, the curves are separated by one unit of normalized signal. (c) Percent change of decay time extracted from four NV centers DEER-time signals taken with a chirp pulse (blue) and a π pulse (green).

The left column (blue curves) are all scans taken with a chirp pulse on the electron spin, while the right column (green curves) are all taken with a π pulse. It is clear from the fit that the contrast with a chirp pulse was higher for all scanned NVs. The fitted width of the Gaussian was, on average, 15 MHz, indicating that the broadening is not solely rising from the pulse span and is still narrower than the linewidth reported for similar experiments[51,54].

I scanned all four NV centers with a DEER-time sequence. To make the comparison between a chirp and π pulses, I took each scan twice, once with a pulse on the electron spin resonance frequency and second with a pulse 15 MHz detuned from the electron spin resonance frequency, making it completely off-resonance from the detected signal at the DEER frequency. The π pulse was again with a length of 440 ns, resulting in a width of $\sim$ 2.2 MHz. The chirp pulses were all with $Q = 5$ and length of 2 µs, resulting in a span of $\sim$ 3 MHz. All scans were fitted to a stretched decay exponent of the form $S(\tau) = Ae^{-(\tau/\Gamma)^{\beta}} + c$ since no oscillations of strong dipolar coupling were detected in the data[51].

We expect to see a shorter decay time (Γ) if the pulse flipped the spins compared to when it did not, where the decay time will be the intrinsic coherence time of the NV center ($\Gamma = T_2$). To estimate the pulse effect on the electron spins, I calculated the percent change of Γ between the on-resonance and off-resonance pulses for the chirp and π pulse cases as follows: $\Delta\% = \frac{\Gamma_{\text{off}} - \Gamma_{\text{on}}}{\Gamma_{\text{off}}} 100$. The results are plotted in Figure 3.2c where it is clear from the green bars that the change was more pronounced when I used the chirp pulse compared to the π pulse. Similar to the effect observed with the NV centers, we see that the chirp pulse is more robust in driving the electron spins.

The better performance of the chirp pulse in the DEER sequences can first be due to the robustness of the pulse, which is also witnessed when used for driving the NV center. In addition, the duration of the π pulse used to address the electron spins is estimated from the NV center coupling to the MW field. The interaction of the electron spins with the MW is not necessarily the same as with the NV center, and still, if it is similar, the duration in this experiment was long ($t_\pi > 500$ ns) resulting with a very narrow bandwidth pulse, which is highly sensitive to noise and therefore, has lower efficiency in addressing the spins.

3.3 Discussion

We explored the advantages of using chirp pulses over traditional π pulses for electron spin sensing with NV centers in diamond. Our results clearly demonstrate that chirp

pulses enhance both contrast and sensitivity, particularly in DEER sequences, offering notable improvements in spin sensing performance.

We first used the chirp pulses on the NV center to characterize its performance. We then used DEER-frequency and DEER-time experiments to show the enhancement that adiabatic pulses can bring to electron spin magnetic sensing. We showed that chirp pulses yield higher contrast compared to π pulses when detecting electron spins with DEER frequency. We discussed the contrast enhancement's connection to the chirp pulse's broader spectral bandwidth, which facilitates more efficient spin interaction. We also showed that the electron spin signals had a narrower linewidth compared to previously reported studies despite the chirp pulse's broad bandwidth, indicating that an optimal chirp pulse can enhance contrast without excessive spectral broadening. Finally, we measured DEER-time and found that chirp pulses also cause a faster decay time of the sensor compared to the π pulses, which is an indication of coupling to electron spins [51].

The improvements we observed with chirp pulses suggest that they could significantly enhance the performance of NV center-based quantum sensors. By improving contrast and spin sensitivity, chirp pulses have the potential to increase precision in detecting weak magnetic fields and spin interactions, which is crucial for various quantum applications such as quantum computing and bioimaging.

To make this technique more applicable, we suggest additional experiments. First, a thorough mapping of the chirp pulse enhancement on the NV center driving, with respect to chirp parameters and NV center coupling to the MW source. We also suggest other experiments showing the use of chirp pulses in electron spin initialization through polarization transfer. The robust spin driving can also assist in applying quantum gates with higher efficiency and enhance the polarization transfer of NV center to electron spin using CNOT and SWAP gates [108].

In conclusion, we have demonstrated that chirp pulses outperform traditional π pulses in terms of contrast and spin sensitivity for electron spin sensing with NV centers. These findings suggest that chirp pulses are a promising tool for enhancing the performance of quantum sensors and could have broad applications in quantum technologies.

"Intelligence is the ability to adapt to change."

Stephen Hawking

4

Sensitivity enhancement with machine learning

One of the advantages of quantum sensing is the possibility to use quantum properties such as entanglement to gain enhancement in the sensor sensitivity and overcome the standard quantum limit. Quantum entanglement opens the door to utilizing quantum algorithms that can accelerate processes. However, not all quantum systems can easily establish a good entangled system; for example, the NV center has to be in high proximity to another spin system in order to establish a high-fidelity entangled system [109]. To this end, quantum machine-learning algorithms can utilize machine-learning techniques and employ principles of quantum algorithms to form an algorithm benefiting from some of the quantum advantages but not depending on entanglement.

In this chapter, I present the use of machine learning algorithms as a tool to improve quantum sensing with a non-single-shot read-out sensor such as the NV center. I cover the theoretical background of an adaptive Bayesian estimation approach based on the quantum phase estimation algorithm in Section 4.1. I present the experimental system and the real-time measured results of a non-adaptive scheme in Sections 4.1.2 and 4.2.

I discuss the possible improvement of the algorithm once a full adaptive algorithm is applied using numerical simulations in Section 4.3.

This chapter's results were published in the manuscript titled "Real-time frequency estimation of a qubit without single-shot-readout" in the journal Quantum Science and Technology published by the Institute of Physics (IOP)[110].

4.1 Background

One very useful quantum algorithm for quantum sensing is the quantum phase estimation algorithm (QPE) suggested by Kitaev[111]. This algorithm aims to estimate a phase accumulated by a quantum sensor due to an interaction manifested in the sensor's Hamiltonian $\mathcal{H}(f)$ with an external field f. The QPE algorithm is based on a system of K ancilla qubits that interact with the sensor for $k = [0, K]$ discrete sensing times exponentially growing, $\tau_k = 2^k\tau_0$, and later undergo a quantum Fourier transform to estimate the phase of the sensor. The shortest sensing time, τ_0, is also the limit for the dynamic range (DR) of the sensor $[-1/2\tau_0, 1/2\tau_0]$.

For the NV center case, the algorithm was performed with a system of three ancilla qubits, which is a system that is not easily accessible[112]. Nevertheless, systems with K number of ancilla qubits are also not trivial for other sensing systems where other requirements are crucial, like the environment of the sensing or the proximity to the target specimen. Therefore, an algorithm based solely on the sensor that applies an adaptive scheme can be an alternative.

One example of these algorithms is the adaptive phase estimation (APE) algorithm, which operates on a single qubit while employing some of the QPE algorithm basics and utilizing an adaptive algorithm based on Bayesian estimation. Figure 4.1a presents a schematic illustration of the APE algorithm consisting of four main steps. Like the QPE algorithm, also in the APE, K sensing times are measured (step ①) where $\tau_k = 2^k\tau_0$. The sensing times are limited by the length of the gate; the shortest time τ_0 should be on the order of the π pulse length, and the longest should not be longer than the coherence time of the sensor, that is, for DC sensing with Ramsey - $\tau_K \leq T_2^*$[113]. However, in the APE, the K sensing times cannot be applied simultaneously; therefore, each is applied for $M_k = G + (K - k)F$ times where G and F are parameters that need to be optimized, and the total number of iterations grows as the sensing time gets shorter[114].

After each sensing step (step ①), we estimate the likelihood function of the sensor's frequency (step ②). The frequency of the sensor translates to the target field

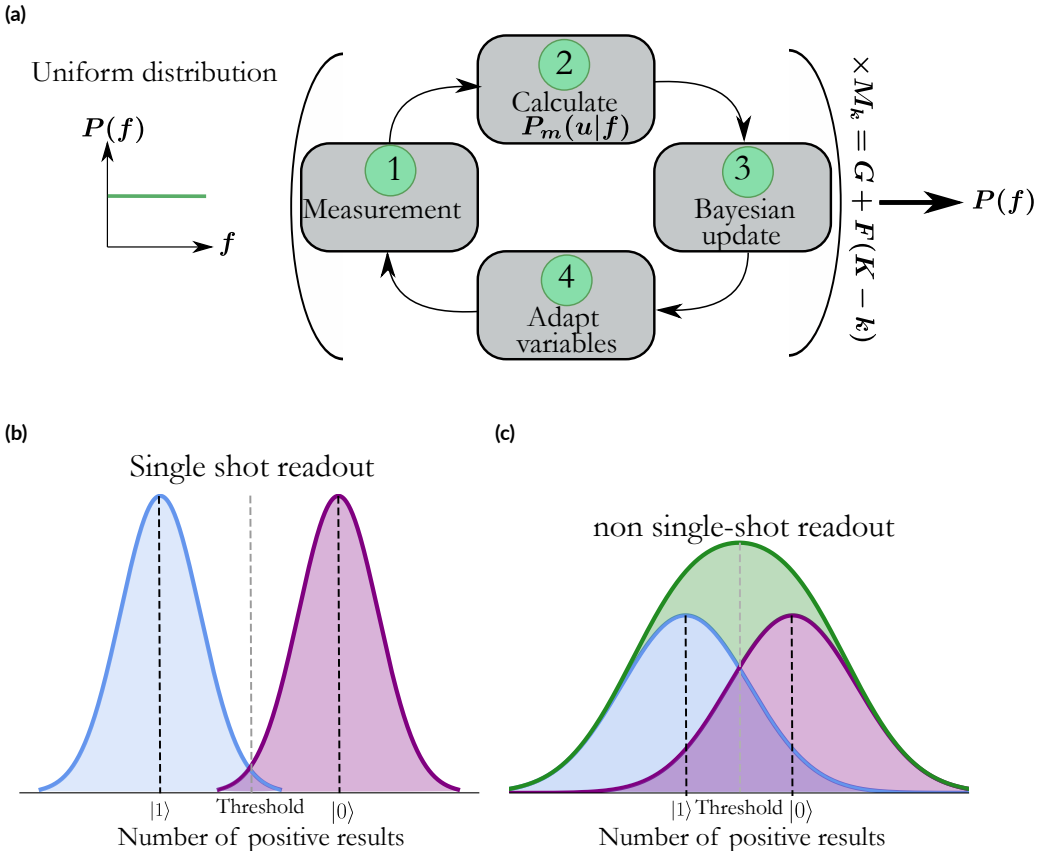

Figure 4.1: (a) Graphical illustration of the adaptive phase estimation algorithm comprising four steps: (1) A pulse sequence suitable for the estimation of the unknown parameter, given the nature of the interaction between the sensor and the parameter. This pulse sequence will be applied with exponentially growing sensing times. The state of the sensor is measured after every sensing time. (b-c) Schematic illustration of the measurement outcome of a single-shot (B) or averaged (C) sensor.

f depending on the interaction of the sensor and the target field. Then, we use the Bayesian estimation protocol to update the full probability function of the frequency (step ③), Equation 4.1, where $P(f)$ is the probability function of f, u is the state of the sensor after the measurement. The adaptive part is embodied in step ④, where the parameters of the measurement are changed to gain maximal information from the next iteration. The parameters are extracted from the updated probability function in step ③ using a machine-learning algorithm for maximizing entropy and information, as will be discussed in Section 4.3.

$$P_{\text{new}}(f|u) \propto P_m(u|f)P_{\text{old}}(f|u) \tag{4.1}$$

We aim to use the APE algorithm to accelerate DC magnetic field sensing. The target magnetic fields can be external fields interacting through Zeeman interaction, the simplest case will be of a small magnetic field parallel to the NV center axis $\hat{z}$ (fifth term in Equation 1.6), or fields rising from dipolar or hyper-fine interaction of external spins with the sensor (third and fourth terms in Equation 1.6). For simplicity, we choose to show a proof of concept of the APE on a Zeeman interacting field, as will be elaborated in the section of the experimental methods and results (Section 4.2).

Concentrating on a target field of DC magnetic field, we can establish the interaction of the field with the sensor through the relevant Hamiltonian- $\mathcal{H}(f) = \gamma_{\mathrm{NV}} \Delta B = 2\pi f$ where f is the frequency of the field that we aim to detect. Figure 4.2a shows the sensor energy levels with a biased magnetic field $B^{(0)}$ and the change that the unknown field ΔB is concealed in a shift of the eigenvalues of the sensor. Sensing the DC magnetic field can be easily done with a Ramsey pulse sequence as long as the target field is $\Delta B > \frac{1}{\gamma_{\mathrm{NV}} T_2^*}$. Adapting the general APE scheme to a DC sensing scheme, we can insert the Ramsey sensing scheme in step (1) as illustrated in Figure 4.2c.

During a Ramsey sequence, the phase accumulated on the sensor superposition state (Equation 1.8b) is proportional to the magnetic field $\varphi = \gamma_{\mathrm{NV}} \Delta B \tau = 2\pi f_{\Delta B} \tau$, and it will be presented as an oscillating signal in time decaying with T_2^* decay time, as illustrated in a simulation in Figure 4.2b. Therefore, the likelihood function, used in step (2), is based on this theoretical model of the sensor under the Ramsey pulse sequence [39] where the oscillatory nature is found in the cosine function of the likelihood function (Equation 4.2). The outcome of each measurement, which is the state of the sensor- $u = |0\rangle \,/\, |1\rangle$, will modify accordingly the likelihood function.

$$P_m(u|\Delta B) = \frac{1}{2}\left[1 + (-1)^u e^{-(t/T_2^*)^2} \cos(2\pi f_{\Delta B} t - \varphi)\right] \tag{4.2}$$

As this is an APE protocol and not a simple Ramsey sensing, the sensing times will not be equally distributed in time but will be exponentially distributed with only K sensing times (illustrated as the blue dots in Figure 4.2b). Also, the sensing phase, θ, which is the phase of the second $\pi/2$ projection pulse, will not be equally distributed but will be determined from iteration to iteration to find the optimal phase for maximal information (step (4)) [115,116,117].

4.1.2 Bayesian estimation algorithm with non-single-shot read-out sensor

The DC magnetometry APE algorithm has been proven in the past to enhance the sensitivity of the NV center at low temperatures with single-shot read-out (SSR) abilities (Figure 4.1b)[118]. However, when using the NV center under ambient conditions, it can no longer be a single-shot read-out sensor and has to be treated with averaged

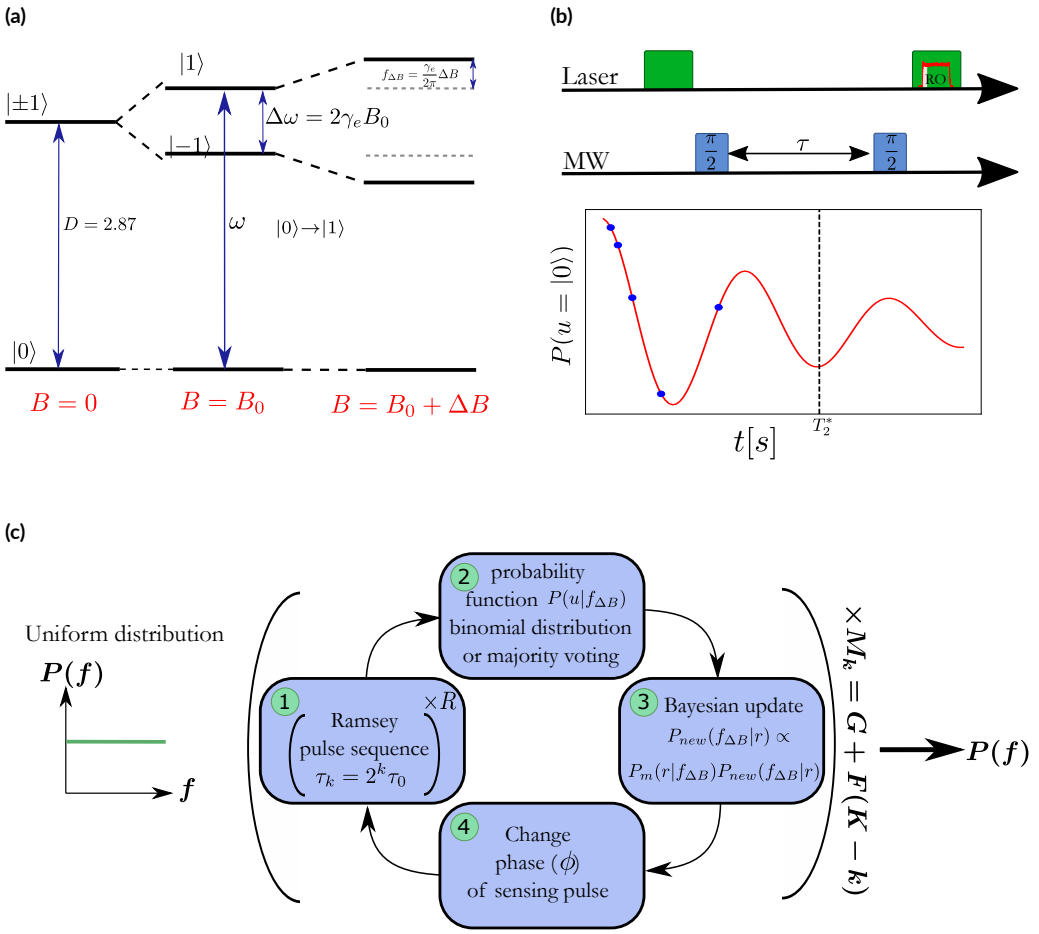

Figure 4.2: (a) Illustration of the energy levels of the NV center under a static magnetic field with a small detuning. The errors indicate the microwave field resonant with the $|0\rangle \rightarrow |1\rangle$ transition. (b)The top panel is a Ramsey pulse sequence applied on an NV center to sense a DC magnetic field. The red curve is a simulated result for a Ramsey sequence with linearly changed sensing times between zero and T_2^*. The blue points indicate the K sensing times used in the PEA scheme. (c) Graphical illustration of adaptive phase estimation algorithm for DC magnetometry with a non-SSR sensor.

read-out (Figure 4.1c). In this case, we should update the likelihood function to consider the number of positive results r out of R averaged repetitions. The naive method to deal with this is to use a "majority voting" method where each measurement outcome r is assigned with a state $|0\rangle$ or $|1\rangle$ compared to a threshold determined between the states and thus Equation 4.2 can be used[119]. However, this approach is prone to mistakes due to noise and does not exploit the large amount of data collected from R repetitions. A different approach suggested in 2019[120] is based on a "binomial distribution" method where the likelihood function has R different outcomes for R repetitions, as presented in Equation 4.3a.

$$P(f|r) = \begin{pmatrix} R \\ r \end{pmatrix} P_d(1|f)^r [1 - P_d(1|f)]^{R-r} \tag{4.3a}$$

$$P_d(1|f) = \alpha \left[1 - Ve^{-(t/T_2^*)^2} \cos(f_{\Delta B} t 2\pi - \varphi)\right] \tag{4.3b}$$

The likelihood function uses the probability to detect a positive outcome given the target field frequency f - $P_d(1|f)$ as the probability for r positive outcomes for the binomial distribution. The Ramsey oscillatory behavior is noted in the probability for a single outcome $P_d(1|f)$ in Equation 4.3b, where α is the sensor's threshold, and V is the visibility of the sensor (see Appendix E.1). Since this approach considers the full range of R possible outcomes, a noisy measurement will not result in a mistake but with an error within the range of the measurement's noise. So far, The binomial distribution has been shown to achieve better sensitivity in simulations but has never been demonstrated in an experiment. In this work, we show for the first time a successful implementation of the scheme in a real-time measurement with a non-adaptive scheme in Section 4.2 and a simulation of an adaptive case based on the real experiment parameters in Section 4.3.

4.2 Real-time non-adaptive scheme - methods and results

The experimental setup that offers a real-time experiment was built with a Quantum Machines Operator-X (OPX), which is a control hardware aimed at quantum system controlling, based on a Field Programmable Gate Array (FPGA) (detailed description of the setup is in Appendix A.1). The pulse program, including the inherent calculations, was programmed to the OPX with a dedicated programming language named Quantum Universal Assembly (QUA) (elaborated description of the programming adaptation with QUA see Appendix A.2).

Using the real-time platform, we compared the experimental results between the "majority voting" approach and the "binomial distribution" approach. We collected data from a single NV center with a dephasing time of $T_2^* = 3.5\,\mu s$. We used five sensing times ($K = 4$) with $\tau_0 = 100\,ns$ in the Ramsey measurement pulse sequence (step ①). The probability function estimating the external magnetic field was constructed with a resolution (binning) of 25 kHz. For each external magnetic field, we applied the scheme twice, once with the "majority voting" probability function (Equation 4.2) in step ② and once with the "binomial distribution" probability function (Equation 4.3a). After the Bayesian update (step ③), we change the phase of the second $\frac{\pi}{2}$ pulse linearly between zero and π in a non-adaptive manner following a predetermined measurement sequence[114] (step ④).

Figure 4.3a presents the probability function of the frequency as it is updated with the iterations of a measurement of a random magnetic field using the approach described above (Bayesian, binomial distribution, non-adaptive). The probability function starts as a uniform distribution. The first iterations apply the shortest sensing time, guiding the probability function to a rough frequency estimation. As the iterations advance, the sensing time gets longer, and the estimated frequency gets focused and narrower to a more precise estimate. After the last iteration, the most probable frequency is set as the final estimation for this measurement.

We applied the two approaches for a non-SSR sensor in a non-adaptive scheme on 500 randomly chosen magnetic fields $f_{\Delta B}$ in the DR of $[-2, 2]$ MHz. This DR is narrower than the potential DR allowed by a $\tau_0 = 100\,ns$ due to a dramatic increase in the level of noise once employing the Bayesian update. The increase in noise for larger detunings is still unclear. We applied each detuning with seven different repetition numbers $R = (100, 250, 500, 750, 1000, 2500, 5000)$ for both methods, the order of repetition number and methods was randomly switched between detunings.

To compare the two sensing methods, we calculated the mean square error (MSE) based on the estimated frequency $\tilde{f}_B$ calculated from the probability $P(f|r)$ after every iteration (Equation 4.4). We note that the MSE for larger R does not improve by much (Figure 4.3c), and we attribute this to the slight improvement of the contrast defined in Equation 4.5 where $\alpha_{0/1}$ are the number of photons per measurement for states $m_s = 0/1$ of the sensor, as defined in Chapter 1. The superiority of the binomial distribution approach is also evident for shorter sensing times, starting from $R = 250$ with $T = 0.34\,s$.

$$\mathrm{MSE} = \sqrt{V_B} = \sqrt{\left\langle \left(\tilde{f}_B - f_B\right)^2 \right\rangle} \tag{4.4}$$

$$C = \left[1 + \frac{2(\alpha_0 + \alpha_1)}{(\alpha_0 - \alpha_1)^2 R}\right]^{-1/2} \tag{4.5}$$

To see the improvement in MSE, we plot it as a function of the iteration number

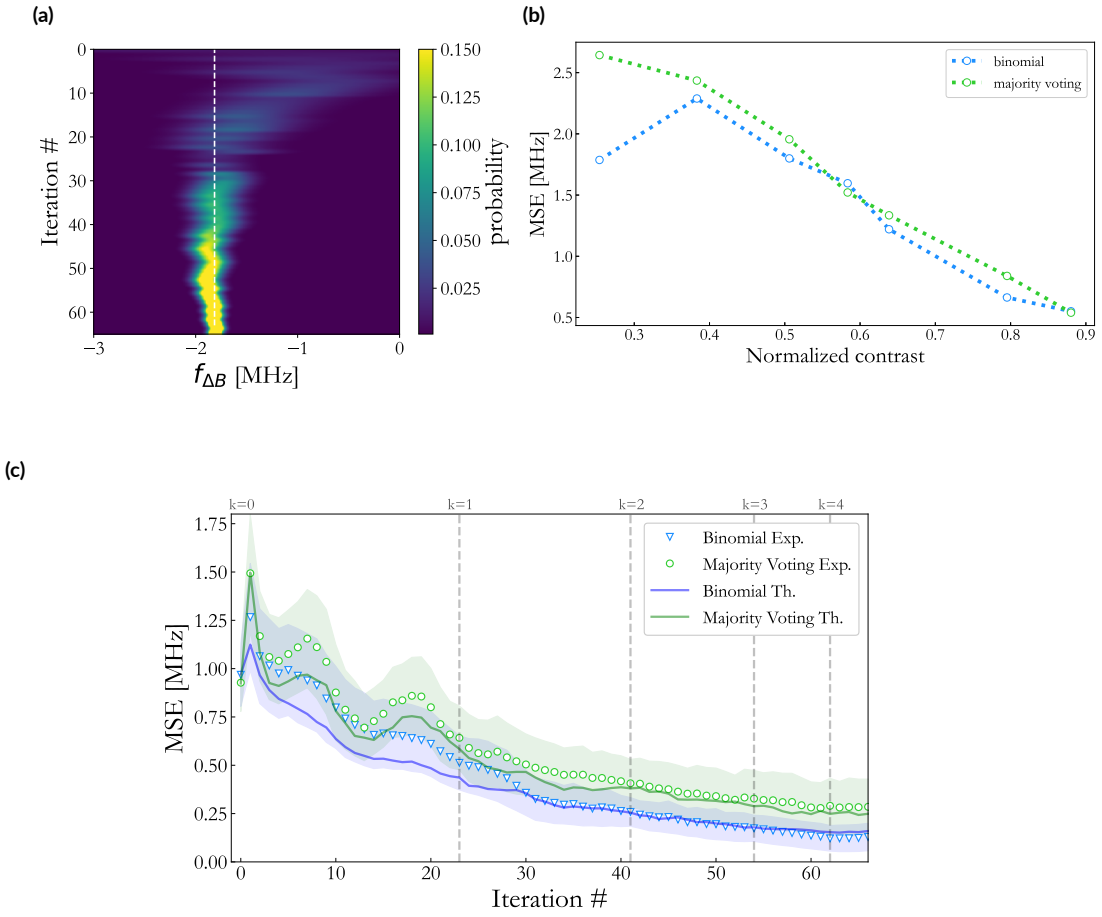

Figure 4.3: (a) The probability function of a single magnetic field detuning as it is updated with the iterations of the scheme. The detuning here was 1.895 MHz. (b) MSE as function of contrast. For typical values of α_0 and α_1 from our experiment and our choice of different R in the range of [100,5000], this translates to a contrast range from nearly zero to 0.9. (c) Error (square root of variance) as a function of total measurement time (number of iterations) with binomial distribution approach (blue) and majority voting approach (green) for a repetition number R=2500. The data presented here is for 500 random chosen detunings. The vertical lines (different values of k) represent the move to the next τ in the algorithm.

for the $R = 2500$ case in Figure 4.3c. The data presented in Figure 4.3c was taken on a similar setup built by our collaborators from the group of Cristian Bonato in Heriot-Watt University as described by Arshad et al. [121]. The experiment parameters were the same while the NV center used had a decoherence time of $T_2^* = 5.5\,\mu s$. The results show improvement in precision as the iterations progress, and a reduction of the MSE with the same measurement time when using the binomial distribution approach. The best MSE achieved was ≈ 0.12 MHz for $R = 2500$ with a total sensing time of $T = 1.07$ s when using the binomial distribution method. The majority voting method reached a MSE of ≈ 0.28 MHz within the same time, more than twice as large. The lowest possible MSE is limited by the decoherence time of the sensor where MSE $\geq \sqrt{\frac{1}{T_2^*}}$. Finally, we see a good agreement between the experiment and a simulation based on the experimental parameters used in the experiment. The small discrepancy between experiment and simulation can be explained by a little uncertainty in the detection probability for the 0 and 1 state, i.e., $P_d(1|m_0)$ and $P_d(1|m_1)$.

4.3 Simulations of the adaptive protocol

To fully exploit the benefits and advantages of the APE algorithm it should be implemented with the adaptive component of the scheme in step (4). In the last section, I described the results from a non-adaptive experiment where the phase of the Ramsey measurement, the control parameter that can maximize the information in the measurement, was predetermined and changed linearly between each M_k iteration. To apply the adaptive scheme, the optimal phase should be calculated based on the last probability function calculated. The Fisher information, as the inverse of the Cramér-Rao lower bound (CRLB), that represents the minimum reachable variance for any (unbiased) estimator, can estimate the phase φ that will maximize the information obtained in a measurement. Therefore, in step (4), the phase can be adaptively changed based on the maximized Fisher information (Equation 4.6). Where $A = \frac{r^2}{R^2} + \left(1 - 2\frac{r}{R}\right)\alpha$ and $B = \left(1 - 2\frac{r}{R}\right)\alpha V$ (full derivation can be found in Appendix E.1).

$$\mathcal{I}(f_{\Delta B}) = E\left[\left(\frac{\partial}{\partial f_{\Delta B}} log\left(P(r|f_{\Delta B})\right)\right)^2\right] \tag{4.6a}$$

$$\frac{\partial}{\partial \varphi}\mathcal{I}(f_{\Delta B}) = 0 \tag{4.6b}$$

$$\varphi_{opt} = 2\pi E\left[f_{\Delta B}\right] t - cos^{-1}\left(\frac{\sqrt{A^2 - B^2} - A}{B}\right), \tag{4.6c}$$

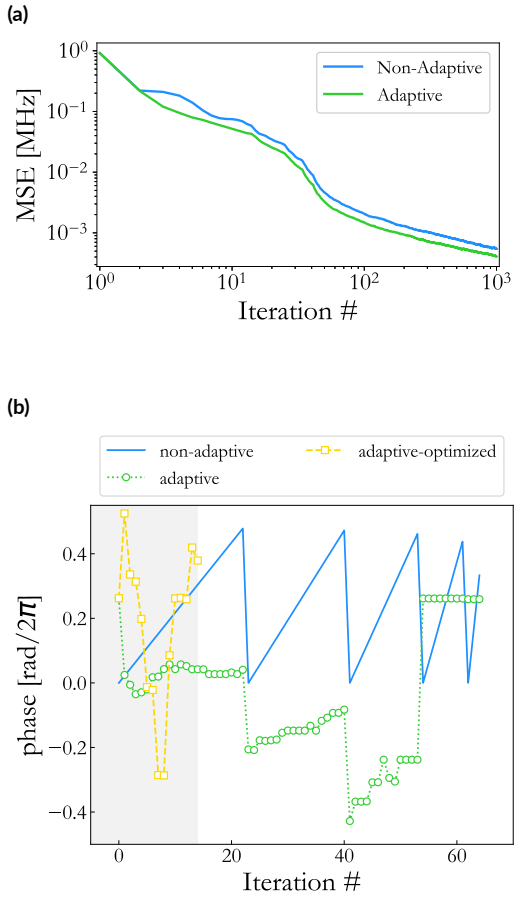

Figure 4.4: (a) Simulated experiment with the calculated phases for the different methods: non-adaptive (blue) and our adaptive protocol (orange). After reaching the end of the settings determined by the PEA scheme, measurement times $\tau = T_2^*$, and phases are chosen at random (non-adaptive) or via adaptive algorithm. (b) Comparison between three different phase calculations for a single experiment with detuning of $f_{\Delta B}$=-1.3 MHz: non-adaptive (blue), our adaptive (green) and the adaptive-optimized (yellow), the latter showing an improvement in the number of iterations (=time) needed to attain the correct phase. The vertical lines (different values of k) represent the move to the next τ in the algorithm.

The benefit of the adaptive scheme was evaluated based on a numeric simulation comparing the MSE of non-adaptive and adaptive scheme with the binomial distribution approach. We simulated the experiments based on the dephasing time (T_2^*) and threshold (α) of the NV used in the real-time experiment, and the experimental parameter $R = 10^5$, $G = 3$, $F = 2$. Simulations were performed by numerically reproducing the experiment, randomly generating a simulated photon number r from a binomial

distribution as in Equation 4.3a.

The simulation shown in Figure 4.4a included two regimes. The first one, where we increase the τ exponentially, is the 'high dynamic range' regime, and the second, where we reach T_2^* and continue measuring from that iteration number at $\tau = T_2^*$, hence the clear change in slope at iteration number (approximately) 30 in Figure 4.4a. In both cases (non-adaptive and adaptive), the probability function was calculated based on the binomial distribution approach. In the simulation of the adaptive scheme, the phase of the Ramsey readout pulse in the next iteration was calculated based on the probability function (step (4) in Figure 4.2a) and Equation 4.6c, whereas in the non-adaptive scheme the phase was linearly ramped between zero and π (see Figure 4.4b).

The phases calculated for the adaptive simulated experiment show convergence of the phase in a small number of iterations, smaller than M_k iterations determined theoretically for each sensing time (Figure 4.4b, green circles). This convergence raises the possibility of reducing the number of iterations for each sensing time by moving to the next sensing phase once the phase remains steady for three iterations with an error of $\frac{0.1}{\pi}$ (Figure 4.4b, yellow squares). We denote this method as adaptive-optimized. It has the potential to reduce the total measurement time significantly, which will also improve the sensitivity.

4.4 Discussion

We performed a real-time Bayesian update with an NV center, a non-SSR sensor at ambient conditions. We compared the MSE of the sensor between two calculation methods - majority voting and binomial distribution, and showed that the latter approach has better sensitivity than the former. We showed by simulation that an adaptive scheme could further improve the MSE and suggested using it to also reduce the total number of iterations and, therefore, the total sensing time and offer an extra improvement on the sensitivity. Our simulations suggest that these schemes can achieve a sensitivity four times better than the non-adaptive approach.

This work demonstrates how one can use non-SSR sensors as practical tools in the APE algorithm and serves as a proof of concept for a specific non-SSR sensor, the NV center in diamond. Nevertheless, it could also be implemented in other sensing systems, as the approach is general, and for other sensing schemes, such as AC magnetometry using dynamical decoupling or electron spin sensing with DEER.

"The only thing you can do easily is be wrong, and that's hardly worth the effort"

Norton Juster

5 Discussion

The overarching goal of this thesis was to advance the use of the nitrogen-vacancy (NV) center in diamond as an atomic-scale magnetic sensor [17] for detecting electron spins [52,51,53] in molecular systems, particularly molecular spin qubits (MSQs) [55,56]. This represents a significant step toward realizing a hybrid quantum system combining the NV center with MSQs. Despite the substantial progress in NV-based sensing, challenges persist in adapting these sensors to the molecular complexity and coupling nuances of MSQs. This work addressed these challenges by enhancing the NV center's sensitivity and coherence through a series of innovative techniques. Below, I summarize and synthesize the findings from each chapter, placing them in the broader context of the research objectives and future directions.

Sensing molecular spin qubits with NV centers

The first objective was to demonstrate the potential of the NV center for sensing the dipolar coupling to an electron spin in a molecular spin qubit (MSQ). I chose copper phthalocyanine (CuPc) as a target molecule due to its compatibility with diamond surfaces and spin properties [62]. To overcome some challenges, I introduced a novel pulse sequence, "Ramsey correlation", designed to allow adiabatic pulses (chirp pulses) [102,105,107,108] to address the broad magnetic spectrum of the molecule electron spins.

Theoretical derivation of the Ramsey correlation showed the potential of isolating dipolar interaction from other DC interactions. In addition, I demonstrated how the correlation of the sequence breaks decoherence limitations and can stretch the coherence of the NV center beyond the Ramsey T_2^*. With the assistance of numerical simulations, I was able to show how the dipolar coupling is isolated from other DC fields and vice versa. I also used the simulations to show the effect of the chirp pulse on a complex magnetic spectrum, such as the electron spin in the CuPc molecule.

An experimental effort was put into two aspects: first, Ramsey correlation proof of concept at room temperature measurements, and second, MSQ sensing under cryogenic and ultra-high vacuum environment. Using the room temperature setup, I showed the dipolar coupling of the NV center to an electron spin in the diamond lattice. I compared the efficiency of the Ramsey correlation sequence to the well-known and used DEER sequence and showed better contrast for the Ramsey correlation. I tested the effect of the chirp pulse parameters on the signal detection with Ramsey correlation.

The results from the low-temperature experiments on a diamond with 10% CuPc molecules in a thin layer of H_2Pc highlight critical findings and point toward future improvements in NV-based quantum sensing.

- **Prolonged coherence beyond** T_2: The Ramsey correlation measurements revealed coherence times exceeding the sensor's T_2. With further experiments controlling the correlation time, I showed a periodic occurrence of prolonged coherence, likely due to the refocusing of correlated magnetic noise from the Larmor precession of carbon nuclear spins. In addition, a second frequency was detected, which is most likely a spurious harmonic frequency inherent in the pulse sequence. This insight underscores the utility of correlation-based techniques for noise mitigation.

- **Dipolar coupling to CuPc spins**: Due to the prolonged T_2, I could detect a signal rising from the chirp pulse centered around the CuPc magnetic spectrum. A short decay time of $T_2 = 4.2 \pm 0.5$ µs was detected, shorter than the off-resonance decay time, which was $T_2 = 5.5 \pm 1.3$ µs, indicating interaction with the MSQ electron spin. In addition, further experiments with different spans of the adiabatic pulse showed a gradual change in signal, supporting the assumption that the chirp pulse was driving the MSQ's electron spins.

These findings are promising and place the Ramsey correlation sequence as a promising method for electron spin detection and DC field sensitivity with prolonged coherence in general. Future work should focus on improving the spectral addressing of

MSQs with optimized chirp pulses to unveil more information on the target electron spin system. In addition, experiments with high and low magnetic field regimes can assist in accounting for other noise sources refocused by the correlation. These advancements will bring NV-based sensing closer to practical applications, such as nanoscale magnetic imaging and hybrid quantum technologies.

Enhancing sensitivity with adiabatic pulses

The second objective was to explore the advantages of using adiabatic pulses [102,105,107,108] over traditional π pulses in enhancing electron spin sensing with NV centers. I showed experimental results where the chirp pulses significantly improved sensitivity and contrast, particularly in DEER measurements. The broader spectral bandwidth of the chirp pulses enabled more efficient spin interaction with the MW. In addition, the broader spectral driving of the chirp pulse did not broaden the spectral signal detected from the electron, making it a viable pulse for future experiments.

These findings suggest that chirp pulses could play a pivotal role in improving NV center-based quantum sensors. Beyond sensing, the robust spin-driving capabilities the adiabatic pulse offers could facilitate spin polarization transfer and efficient quantum gate operations, further bridging the gap toward hybrid quantum systems. Future work should focus on optimizing chirp pulse parameters, exploring their application in spin initialization, and integrating them into more complex quantum sensing protocols.

Bayesian inference for real-time adaptive sensing

The third objective addressed enhancing the NV center's sensitivity to DC magnetic fields by employing machine learning techniques, specifically Bayesian inference for adaptive phase estimation (APE) [118,120]. By implementing a real-time Bayesian update scheme with the NV center as a non-single-shot read-out sensor, I demonstrated improved sensitivity and reduced measurement times of DC magnetic sensing. I showed with simulations that an adaptive scheme could further enhance sensitivity compared to non-adaptive methods.

This proof of concept underscores the feasibility of using machine learning to optimize NV-based sensing strategies, particularly in applications requiring rapid and precise magnetic field measurements. The adaptive Bayesian framework is general and could be extended to other sensing modalities, such as AC magnetometry and electron spin sensing, broadening its applicability to diverse quantum sensing scenarios.

Outlook

Together, the methods developed in this thesis represent significant advancements in NV center-based quantum sensing. The Ramsey correlation sequence, chirp pulses, and real-time Bayesian inference address key limitations in sensitivity, coherence, and adaptability, laying the groundwork for more complex sensing applications. While the immediate focus was on detecting and characterizing molecular spin qubits, these techniques have broader implications for quantum technologies, including bioimaging, quantum computing, and hybrid quantum systems.

Looking forward, several directions emerge:

- **Refinement of Target Systems**: Expanding the study to MSQs with lower hyperfine coupling and better spectral compatibility with NV centers will enhance the reliability of sensing experiments.
- **Low-Temperature, High-Field Experiments**: Implementing the methods developed here in cryogenic setups and stronger magnetic fields will enable better initialization and polarization of MSQ spin states, a critical step for hybrid quantum systems.
- **Integration of Techniques**: Combining Ramsey correlation with chirp pulses and Bayesian adaptive sensing could yield unprecedented sensitivity and coherence, pushing the boundaries of NV-based sensing.
- **Application to Quantum Communication**: Beyond sensing, these advancements could enable quantum state transfer and entanglement generation between the NV center and MSQs, opening the door to scalable hybrid quantum networks.

In conclusion, this thesis has taken important steps toward realizing the potential of the NV center as a versatile tool for molecular spin qubit sensing and quantum technology integration. The methodologies developed herein pave the way for future research aimed at bridging the gap between theoretical promise and experimental realization in hybrid quantum systems.

A

Experimental methods

A.1 Experimental set up

All magnetic sensing experiments reported in this research work were done on confocal optical setups. All setups are based on a generic confocal microscope suited for NV center sensing with slight changes and differences between them, as will be clarified in this section. I designed and constructed a room temperature setup, which was used in the majority of the reported experiments, and its main components are illustrated in Figure A.1 and explained in detail below.

A confocal microscope for NV centers has three main parts, separated by the dichroic mirror element. The first, the excitation part, includes the diode laser of green wavelength (Swabian Instruments GmbH DL nSec PE 520), 532 nm, a single-mode fiber, and collimators for coupling the laser in the fiber and collimating the beam going out of the fiber. The second, the detection path, includes the detection box and its elements. Finally, the third part, the sample part, includes the objective and stage holding the diamond sample.

The purpose of the excitation part is to prepare and control the excitation laser. We use a band-pass filter to remove possible sub-harmonics and couple the laser beam in a single-mode fiber with a fiber coupler. The single-mode fiber converts the laser beam

spatial profile to a Gaussian, and together with a fiber collimator, the beam is collimated with a waist diameter of $\sim 2.4\,\mathrm{mm}$ and a maximal waist distance of $> 5\,\mathrm{m}$ (the distance on the propagation axis of the beam from the narrower point of the waist to the place where the beam waist is doubled) before entering the objective in the sample part of the setup. This apparatus ensures that the Gaussian-shaped laser beam enters the objective aligned and is not cut to reduce the convolution effects of the Fourier image of the beam on the sample.

Before the beam enters the objective, it passes the dichroic mirror. Depending on

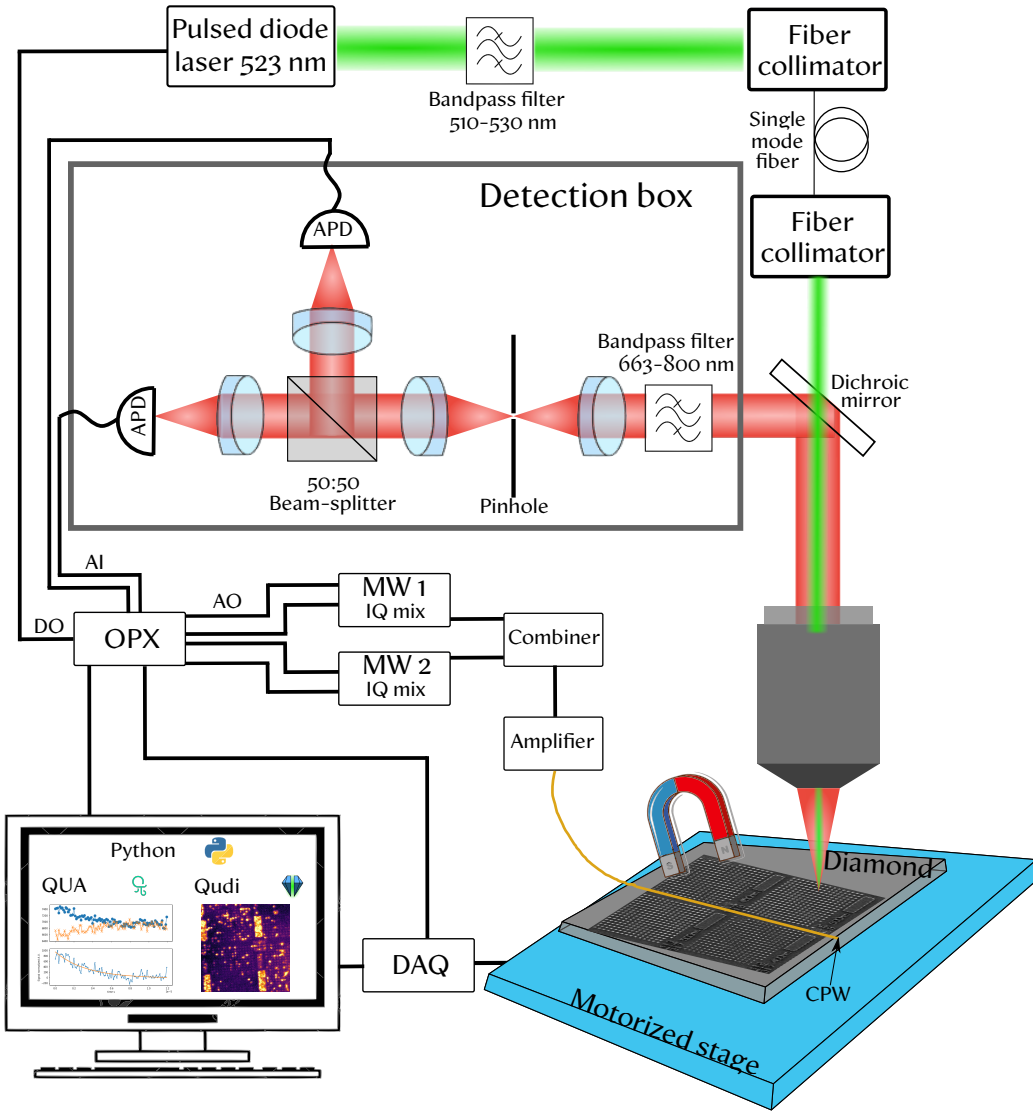

Figure A.1: Schematic of NV center confocal set-up

the physical assembly of the setup, the dichroic mirror can be a high-pass or low-pass, usually with a cut-off around ~ 560 nm. The purpose of the dichroic mirror is to separate the excitation and detection paths of the setup; the only part of the setup where both wavelength regimes are together is at the sample stage and objective. The objective used in the room temperature setup is an Olympus MPLFLN100x objective with a numerical aperture of 0.9 and a working distance of 1 mm. The objective is situated inside a manual vertical positioner, allowing a manual approach of the objective to the sample.

For focus fine-tuning, the sample is located on a closed-loop piezoelectric stage, offering sub-nanometer movement resolution (Piezosystem Jena GmbH, TRITOR 102 SG). The stage has three movement axes offering a scanning range of 80 µm, which is controlled by a data acquisition card (DAQ). The Jena Piezosystem is located on a motorized coarse stage (Newport M-406 XY linear stage), enabling movement in a range of millimeters. The green laser reflected by the sample, along with the red photons emitted from the NV centers and any other light source, is collected by the objective and returned to the dichroic mirror.

The dichroic mirror separates the reflected green light from the red-emitted photons and the read-out part of the system. The read-out part is located inside a black box, reducing any optical environment noise. A band-pass filter (Semrock 731/137 nm BrightLine) is placed at the entrance window of the box, filtering out any residual green laser or noise. The collected beam then goes through a pinhole of 50 µm located between two lenses and exactly in their focal point. The pinhole is a crucial element in the confocal microscope; it blocks any light source not coming from the focus point of the objective, reducing noise from a deep or shallow focal plane. After the pinhole, a 50 : 50 beam splitter and two single photon detectors (avalanche photodiode - APD, Excelitas SPCM-AQRH-12) are placed in a Hanbury Brown and Twiss configuration [122] to determine with autocorrelation if the detected fluorescence is from a single quantum emitter.

A permanent magnet and an MW antenna are situated close to the diamond for magnetic control of the NV center. The antenna is a coplanar waveguide (CPW) printed on a glass or sapphire slide connected with coaxial cables to an MW source, and the diamond is placed on top of the antenna for the maximal field. The permanent magnet is placed on a motorized stage, enabling the search for magnetic field alignment with any spatial orientation of the NV center.

The setup is controlled and synchronized with a Quantum Machines Operator-X (OPX). The OPX is programmed with a dedicated Python-based programming lan-

guage (Quantum Universal Assembly); it is field-programmable gate array (FPGA) based, offering real-time calculations and pulse modification. The OPX is connected with analog outputs (AO) to two MW synthesizers (Rohde-Schwarz SGT100A and Windfreak technologies SynthNVpro), digital outputs (DO) to the pulsed laser diode, and the DAQ, and analog inputs (AI) to the two APDs. The analog outputs provide arbitrarily shaped pulses with frequencies ranging up to 400 MHz, the simplest configuration is two cosine waves with an intermediate frequency (IF) and a relative phase of $\pi/2$. These two waves are the input to the MW synthesizer where the local oscillator (LO) frequency is set to a frequency up to 6 GHz and IQ mixed together to allow frequency control of the driving magnetic field. The output radio frequency (RF) is amplified (Elite-RF) and transmitted to the CPW.

The analog inputs receive signals from the two APDs. Each signal input indicates a photon detected, and it is measured with a time tag with 1 ns resolution, offering a time indication of photon arrival. In addition, for time tagging the signal, each photon detection can be "copied" and transmitted with a DO to the DAQ for synchronized spatial scan (will be elaborated in Section A.2). Finally, a DO signal is used for gating the laser diode synchronized with the driving AO pulses and the photon read-out with the AI.

The setup described above is the frame and basics of all three setups I used in this research. All room temperature experiments reported in this work were performed on this setup. The low-temperature experiments were performed on two cryogenic setups. The results discussed in Section 2.3.3 under Chapter 2 were performed in a cryogenic setup in the lab built by Dan Yudilevich and Jitender Kumar, former lab members, using a liquid helium cryostat made by Cryovac and thermally anchored to a stage situated in an ultra-high vacuum chamber. The low-temperature experiments reported in Appendix C.1 were performed in a cryogenic setup in the lab of Prof. Amir Yacoby at Harvard University built by Ruolan Xue and Dr. Nikola Maksimovic, using the apparatus of a Montana Instruments cryostat.

Both cryogenic setups have a few important differences from the room temperature setup. The first important difference is the scanning mechanism. Both do not use a scanning stage such as the Piezosystem, but a Galvo system which offers scanning of the laser on the sample surface. This system is more suitable for low-temperature setups, as the scanning stage does not work at cryogenic temperatures. However, this approach has limitations in the full image range it can offer.

The second difference is the possible DC magnetic field each has to offer. The lab cryogenic system has a vector magnet built of three superconducting coils and offer-

ing a magnetic field up to $\sim$ 85 G, whereas the magnetic field in the Harvard setup uses a permanent magnet on a motorized stage allowing magnetic fields up to 1300 G. The final difference is the synchronizing unit; the OPX unit used in the room temperature setup is also used in the Harvard cryogenic setup. However, the lab cryogenic setup uses an arbitrary wave generator (AWG, Spectrum Instrumentation GmbH, DN2.663-04; four analog channels, six digital channels, 1.25 GSa/s) which synchronizes all elements of a magnetic measurement apart from time tagging the photon detection, done with a time tagging card (Swabian Instruments GmbH, TimeTagger 20).

A.2 Code adaptation

Controlling the setup is done with an open-source program suitable for NV center setups named Qudi [123]. The software is a Python-based code, offering flexibility in the electronic instruments operated and connecting them all in a user-friendly graphical user interface. For example, spatial scanning with the Jena Piezosystem or the Galvo system is possible through the software, and for both, the scan is synchronized with the photon collection through the DAQ. The system described above collects the photons with the OPX therefore the collected signal is transferred to the DAQ for synchronization with the Jena stage.

Unfortunately, the Qudi software was originally not designed to control the OPX. The OPX is programmed with QUA, a Python-based language, but it was not implemented in Qudi's source code. Since the Qudi platform is highly versatile and meant to be flexible with other elements, I was able to implement the QUA code inside the Qudi platform, including a graphical user interface that allows real-time plots of the detected signals.

A.3 Diamond samples

Prior to sample preparation, a number of calibration and optimization steps were done to ensure the samples met the criteria detailed above: shallow NV centers, long coherence time of the sensor, controlled concentration of CuPc molecules on the surface, and a single orientation of the molecules on the surface.

The NVs within nanopillar waveguides used for all experiments reported in this work were fabricated at the University of Stuttgart by Drs. Rainer Stöhr and Andrej Denisenko. All diamonds have NV centers implanted at an energy of 5/9.8 keV, resulting in NV centers in 5/10 nm depth, respectively. All diamonds have a natural abundance of ^{13}C. To prolong the coherence time, I calibrated an oxygen annealing

process based on the reported results of Sangatawesin et al. [16], showing an increase in coherence time of shallow NV centers resulting in the elimination of carboxylic groups on the surface of the diamond.

Prior to the annealing process, I cleaned the diamonds using a tri-acid boiling cleaning process [124]. For the tri-acid boiling, the diamond is placed in a solution of 1:1:1 mixture of 65% nitric acid, 95% sulfuric acid, and 70% perchloric acid. The acids are heated up in a reflux apparatus overnight. Following the process, the diamond is washed several times with triple distilled water.

The cleaning process was also optimized to avoid any contamination that might damage the diamond during the annealing process. During the optimization, I cleaned the diamond with tri-acid boiling, and the surface was scanned using X-ray photoelectron spectroscopy (XPS) by Dr. Tatyana Bendikov from the Department of Chemical Research Support. During the optimization process, some of the XPS measurements revealed silicon, lead and other contaminations, suggesting contamination from the glass dishes and tweezers used in the process. Finally, after four rounds of tri-acid boiling and clean working tools, including plastic dishes (polypropylene) to avoid glass, we showed the optimal result of a diamond with minimum contamination on the surface (Figure A.2a).

The oxygen annealing process was under 450 degrees Celsius for four hours with a 35 SCCM (standard cubic centimeters per minute) flow rate with 99.999% oxygen purity. To prove a successful implementation of the process, I measured the Hahn-echo signal of nine NV centers in two diamond samples with 9.8 keV implanted NV centers before and after the annealing process. I compared the decay times for each NV center extracted from a fit to an exponential decay of the form- $S(\tau) = \exp(-(\tau/T_2)^2)$. The results plotted in Figure A.2b showed longer coherence times for seven out of the nine NV centers, confirming that the process can prolong NV center coherence.

The measurements reported in Section 2.3.3 in Chapter 2 were on NV centers in diamond treated as described above and with a thin layer of CuPc and H_2Pc evaporated on the diamond surface. The molecules were evaporated using a Knudsen cell [125] with two separate crucibles for the H_2Pc and the CuPc (MBE Komponenten OEZ).

To control the ratio between the two molecules, I calibrated the evaporation rate for each molecule using a thickness quartz sensor (Prevac Quartz Balance QO 40A1) and AFM scans. I evaporated both materials on mica substrates, monitoring the thickness rate as it is detected by the quartz sensor. The mica samples were then measured with an AFM to estimate the real thickness of the layer. To estimate the thickness, I used a scratching method with the AFM tip, where the tip is in contact with the sample,

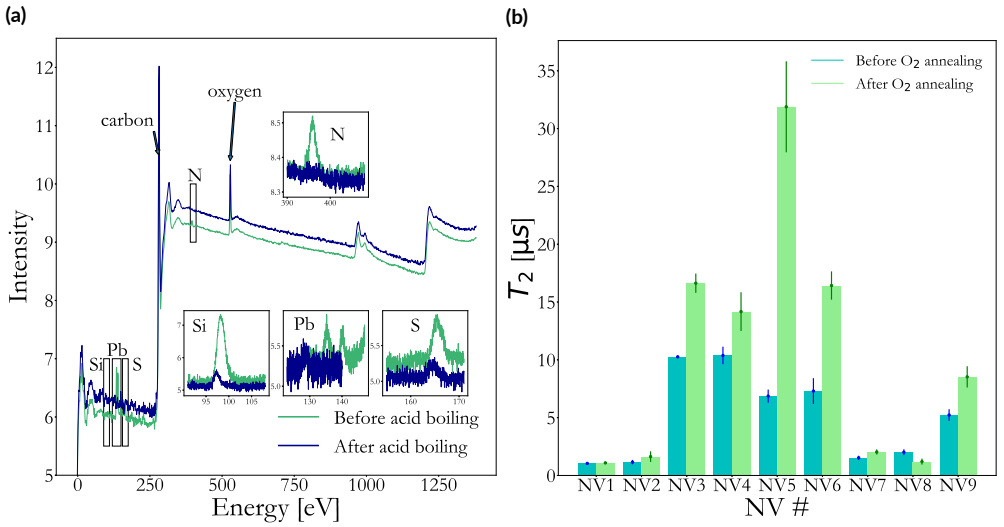

Figure A.2: (a) A wide spectrum of XPS from a diamond cleaned once with acid boiling (green) and a diamond cleaned seven times with acid boiling (blue). Carbon and oxygen are noted with arrows. Silicon, nitrogen, sulfur, and lead are evident in the inset spectra. (b) Decoherence time (T_2) as fitted to the data for nine NV centers before (blue) oxygen annealing and after (green).

and a small force is applied to the sample so any material not strongly connected will be moved with the tip. With this method, I exposed a small rectangle of the substrate mica, and with a tapping mode, I measured the step's height between the mica and the material (Figure A.3a is an example of AFM scratch image).

Figure A.3b shows the reported thickness of the sensor and the scanned thickness with AFM for a set of mica samples. The points were fitted to a linear function to find a factor of 6.6 between the two thicknesses. During calibration, we observed that for high rates of evaporation, a capping process occurs, obstructing the molecule crucible[87] and making the evaporation rate unstable and unreliable. This effect restricts the evaporation rate to be under $5\frac{\text{Å}}{s}$.

For the $\sim$ 30 nm layer of 10 % CuPc reported in Section 2.3.3 in Chapter 2 I evaporated the H_2Pc with a rate of $3\frac{\text{Å}}{\text{s}}$ and CuPc with rate of 0.3, $\frac{\text{Å}}{\text{s}}$ for 10 seconds. However, for a 10 nm thick layer of 1 % CuPc as reported in Appendix C.1 this was more challenging. To achieve this concentration, I needed to use the maximal rate of $5\ \frac{\text{Å}}{\text{s}}$ for the H_2Pc and therefore a rate of $0.05\ \frac{\text{Å}}{\text{s}}$ for the CuPc was needed. However, the quartz sensor is not reliable and highly fluctuating under a rate of $0.2\ \frac{\text{Å}}{\text{s}}$.

The low concentration of $0.05\ \frac{\text{Å}}{\text{s}}$ was extrapolated from the exponential rate behavior under different temperatures as described in the Bachelor Thesis of Felix Weid-

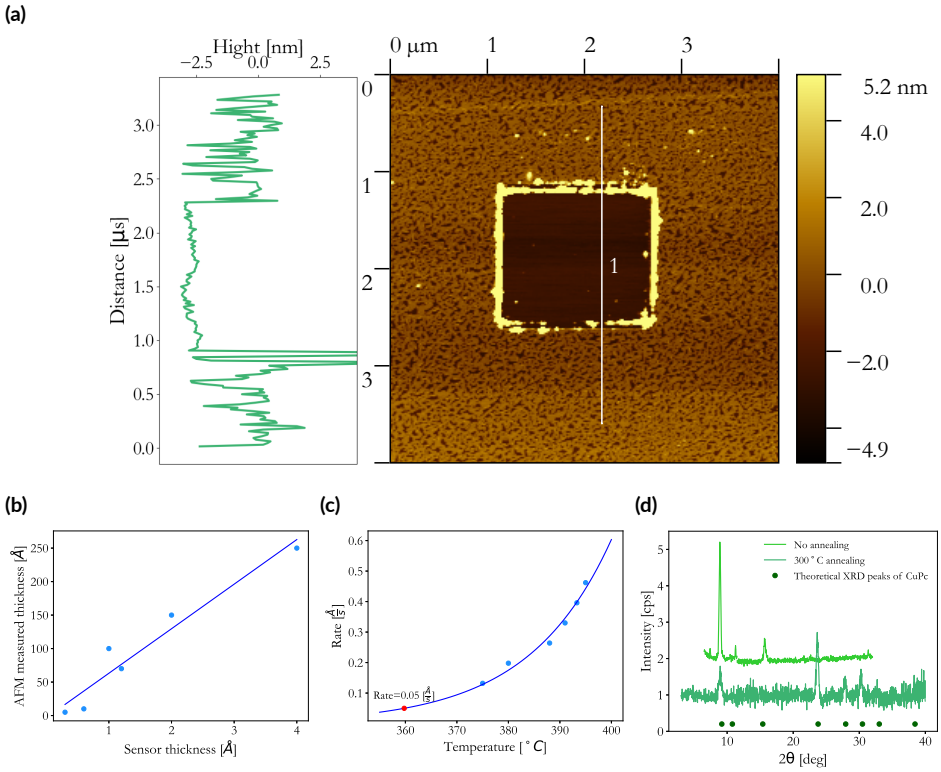

Figure A.3: (a) AFM image of a scratched evaporated CuPc layer on top of mica substrate and a cross-section of height (green curve) showing the height difference between the layer and the substrate. (b) Calibration of evaporated layer thickness between scanned thickness with AFM and reported thickness of the quartz sensor. (c) Evaporation rate detected with the quartz sensor at different temperatures and an exponential fit extrapolating the temperature needed for 0.05 $\frac{\text{Å}}{\text{s}}$. (d) XRD scans of not annealed and 300°C annealing of a CuPc layer.

ner[87]. The rate was measured by the sensor at temperatures of 375°C − 395°C. An exponential function was fitted to the results, and the temperature for a rate of 0.05 $\frac{\text{Å}}{\text{s}}$ was extracted. To verify the success of the process, I evaporated CuPc molecules under the extrapolated 0.05 $\frac{\text{Å}}{\text{s}}$ rate for 15 minutes on a mica sample and then measured the thickness with AFM. Two samples were prepared and showed a thickness of 2 nm which is a rate of 0.02 $\frac{\text{Å}}{\text{s}}$. Finally, the 1% sample was prepared with H_2Pc evaporated at a rate of 3 $\frac{\text{Å}}{\text{s}}$ and the CuPc with the extrapolation method at an estimated rate of 0.02 $\frac{\text{Å}}{\text{s}}$ resulting with 0.6%.

Finally, we scanned the crystals' formation and orientation on the diamond surface with and without annealing to determine if an annealing process of the layer is necessary. The XRD scans were taken by Dr. Anna Eden Kossoy and are plotted in

Figure A.3d. The results are consistent with previously reported XRD scans[82,89] and show different crystal order of α crystals and β crystals; however, both showed alignment of the crystals to the diamond surface.

B

Analytical derivations for MSQ sensing

B.1 Dipolar coupling under the RWA

The rotating wave approximation is a tool we use to grasp an intuitive understanding of a complex time-dependent system and enable analytical derivations of the pulse sequences on the NV center. To invoke it, we apply the derivation in Equation B.1 where $T = e^{-\omega_d t \sigma_z}$ is a unitary transformation of rotation at the frequency of the rotating frame (ω_d) and around the axis it rotates (σ_z). We use this when we apply a pulsed oscillating magnetic field with a frequency matching the resonance frequency of one of the spin transitions of the NV center or any other spin in question.

$$\mathcal{H}_{\text{rot}} = THT^{\dagger} - iT\frac{\partial T^{\dagger}}{\partial t} \tag{B.1}$$

When we apply it to the NV center's lab frame Hamiltonian (Equation B.2), we approximate the three-level system of the NV center to a two-level system of the two states on-resonance with the rotating frequency. By doing so, we are neglecting any interaction between the chosen states and the third state under the assumption that these interactions are off-resonance with the rotating picture and the driving field and, therefore, almost unaffected by it. Using this approach, we treated the NV center as a two-level system under the rotating frame (Equation 1.4).

To get a better intuition of the MSQ electron spin dipolar interaction with the NV center under driving fields on-resonance with the NV center and the target electron spin, we also invoke the RWA. For a simple case of an electron under a Zeeman interaction, the lab frame Hamiltonian would include the dipolar interaction term on top of each spin Zeeman and zero-field splitting Hamiltonians (Equation B.2). The interaction term in the lab frame includes all possible axes of the spins where the $\hat{r}$ vector is the vector connecting the spins' locations, and it can be expressed in the NV center's axes system (with φ and θ being the polar angles of $\hat{r}$). When invoking the RWA for both driving fields, any operator not commuting with σ_z^{NV} of the NV center and σ_z^e of the electron spin will result in a fast rotating term and can be neglected, resulting in the Hamiltonian in Equation B.3.

$$\begin{aligned}
\mathcal{H}_{\mathrm{Lab}}^{\mathrm{NV-e}} &= \underbrace{DS_z^2 + \gamma_{NV} B_z^{(0)} S_z + \gamma_e B_z^{(0)} \sigma_z^e}_{\mathcal{H}_0} \\
&+ \underbrace{\omega_{dd} \left[3\left(\mathbf{S}\cdot\hat{\mathbf{r}}\right)\left(\boldsymbol{\sigma}^{\mathbf{e}}\cdot\hat{\mathbf{r}}\right) - \mathbf{S}\cdot\boldsymbol{\sigma}^{\mathbf{e}}\right]}_{\mathcal{H}_{\mathrm{dd}}} \\
\rightarrow \mathcal{H}_{\mathrm{dd}} &= \omega_{dd} \begin{pmatrix} 3S_x\sigma_x\cos(\varphi)\sin(\theta) + 3S_y\sigma_y\sin(\varphi)\sin(\theta) \\ +3S_z\sigma_z\cos(\theta) - S_x\sigma_x - S_y\sigma_y - S_z\sigma_z \end{pmatrix}
\end{aligned} \tag{B.2}$$

$$\begin{aligned}
\mathcal{H}_{\mathrm{Rot}}^{\mathrm{NV-e}} &= \underbrace{\Delta\sigma_z^{\mathrm{NV}} + \gamma_e B_z^{(0)} \sigma_z^e}_{\mathcal{H}_0} \\
&+ \underbrace{\omega_{dd}\left[3\cos^2(\theta) - 1\right]\sigma_z^e S_z}_{\mathcal{H}_{int}}
\end{aligned} \tag{B.3}$$

Under this picture, we can revisit the full system of an electron with a dipolar interaction to the NV center and a strong hyperfine coupling to a nuclear spin like the case for the CuPc electron spin as written in the full Hamiltonian of the system in Equation B.4a. For the full system, we need to consider the hyperfine coupling, as it might change the quantization axis of the target electron spin depending on its strength compared to the bias magnetic field. We can now invoke the RWA with a double drive, one on the NV center resonance frequency and one on the CuPc electron spin. For simplicity, we will assume we know the state of the CuPc electron spin, which permits us to treat it as a two-level system with a single resonance frequency.

$$\begin{aligned}\mathcal{H}_{\text{Lab}}^{\text{NV-CuPc}} &= DS_z^2 + \gamma_{NV} B_z^{(0)} S_z + \gamma_e B_z^{(0)} \sigma^e + \gamma_n B_z^{(0)} I_z^n \\ &+ \mathbf{I^{Cu}} A^{Cu} \boldsymbol{\sigma^e} + \sum_{i=1}^{4} \mathbf{I^{N_i}} A^{N_i} \boldsymbol{\sigma^e} \\ &+ \omega_{dd} \left[3 \left(\mathbf{S} \cdot \hat{\mathbf{r}} \right) \left(\boldsymbol{\sigma^e} \cdot \hat{\mathbf{r}} \right) - \mathbf{S} \cdot \boldsymbol{\sigma^e} \right]\end{aligned} \tag{B.4a}$$

$$\begin{aligned}\mathcal{H}_{\text{rot}}^{\text{NV-CuPc}} \left(B_z^{(0)} \gg A_{zz} \right) &= \Delta_{\text{NV}} \sigma_z^{\text{NV}} + \Delta_e \sigma_z^e \\ &+ I_z^{Cu} A_{zz}^{Cu} \cos(\theta_A) \sigma_z^e + I_x^{Cu} A_{xx}^{Cu} \sin(\theta_A) \sigma_z^e + \sum_{i=1}^{4} I_z^{N_i} A_{zz}^{N_i} \sigma_z^e \\ &+ \omega_{dd} \left[3(\cos^2(\theta_r) - 1 \right] \sigma_z^e \sigma_z^{\text{NV}}\end{aligned} \tag{B.4b}$$

$$\begin{aligned}\mathcal{H}_{\text{rot}}^{\text{NV-CuPc}} \left(A_{zz} \gg B_z^{(0)} \right) &= \Delta_{\text{NV}} \sigma_z^{\text{NV}} + \gamma_e B_z^{(0)} cos(\theta_a) \sigma_{z_{\text{CuPc}}}^e \\ &+ I_{z_{\text{CuPc}}}^{Cu} A_{zz}^{Cu} \sigma_{z_{\text{CuPc}}}^e + \sum_{i=1}^{4} I_{z_{\text{CuPc}}}^{N_i} A_{zz}^{N_i} \sigma_{z_{\text{CuPc}}}^e \\ &+ \omega_{dd} \left[3 \cos(\theta_A) \cos^2(\theta_r) + 3 \sin(\theta_A) \sin(2\theta_r) - 1 \right] \sigma_{z_{\text{CuPc}}}^e \sigma_z^{\text{NV}}\end{aligned} \tag{B.4c}$$

As discussed, the strength of the bias field will determine the quantization axis of the CuPc electron spin. Two main regimes can be considered. The first is where the bias field is much larger than the hyperfine coupling $B_z^{(0)} \gg A_{zz}$. In this case, the quantization axis will be parallel to the NV center axis, and the Hamiltonian under the RWA will be similar to the free electron dipolar Hamiltonian from Equation B.3 with the addition of the projection of the hyperfine coupling on the $\hat{z}$ axis as written in Equation B.4b with θ_A the angle between the hyperfine $\hat{z}$ term and the NV $\hat{z}$ axis, and θ_r the angle between the $\hat{r}$ vector and the NV $\hat{z}$ axis.

The other regime is when the hyperfine coupling is stronger than the magnetic field, $A_{zz} \gg B_z^{(0)}$. In this case, the driving field of the target electron spin would be on the $\hat{x}_{\text{CuPc}}$ axis in the CuPc axes system. Therefore, under the RWA, the hyperfine $\hat{z}_{\text{CuPc}}$ term would remain while the other terms would be rotating fast and neglected. However, the dipolar coupling term would not transform in the same manner as the NV operators and electron operators no longer share the same axis system. To apply the RWA we projected the electron spin operators on the NV center axis system, resulting in terms of $\sigma_{z/x}^{\text{NV}}$ and $\sigma_{x/z}^e$. Still, only $\hat{z}$ terms are left in the RWA, resulting in Equation B.4c.

B.2 Estimation of the number of molecules in the sensing volume

The sensing volume of a sensor is dictated by the sensor's decoherence time. To detect a target spin with dipolar coupling to the sensor, the dipolar interaction has to be faster than the decoherence time $T_2 > \frac{1}{2\omega_{\min}}$ where $\omega_{\min}$ is the minimal effective dipolar coupling also considering the angle between the $\hat{r}$ vector and the NV $\hat{z}$ axis (θ_r) (Equation B.5a). The maximal distance between the sensor and a target spin, where the dipolar coupling is still detectable, would be for a case where $\theta_r = 0$ (as considered in Figure 2.4a in Chapter 2).

To find the sensing volume of a sensor, we consider the depth of the sensor (h) in the diamond lattice and its decoherence time. To simplify the calculation, we will calculate the volume of an NV pointing toward the diamond surface, i.e., an NV inside a $\langle 111 \rangle$ crystal plane of the diamond and in the [111] direction. The coherence time of the sensor dictates a distance r_i for every angle θ_{r_i} (Equation B.5a), while the depth h will determine which of these distances are above the surface of the diamond, indicating the volume of detectable molecules. Based on these distances, we can draw an arc above the diamond surface for any NV center and calculate the volume of a disk for each distance, as illustrated in Figure B.1. Adding together the volumes of all disks, according to Equation B.5b, would result in the sensing volume of the NV center.

$$r_i = \left[\frac{\mu_0 \gamma_e \gamma_{\mathrm{NV}} \hbar}{2\omega_{\min}} (3\cos^2(\theta_{r_i}) - 1) \right]^{1/3} \tag{B.5a}$$

$$V = \sum_{i \in \{i | r_i > h/\cos\theta_r, \theta_{r_i} \in [0, \frac{\pi}{2}]\}} (r_{i+1}\cos(\theta_{r_{i+1}}) - r_i \cos(\theta_{r_i}))\pi(r_i \sin(\theta_{r_i}))^2 \tag{B.5b}$$

As the NV center is deeper in the lattice or the coherence time is shorter ($T_{2_1} < T_{2_2}$

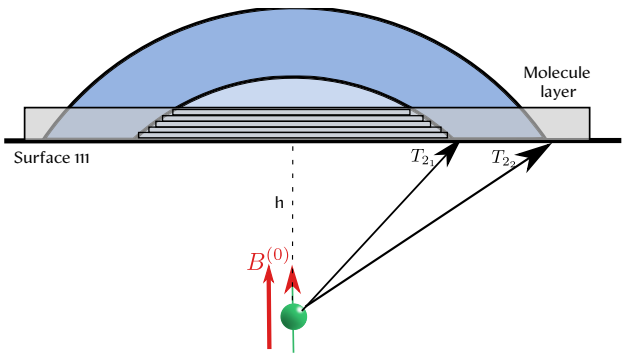

Figure B.1: Illustration of the sensing sphere of an NV center at depth h and with decoherence times $T_{2_1} < T_{2_2}$

in Figure B.1), the volume on the surface would be smaller (see Figure B.1 for illustration). Based on the calculated volume on the surface, the density and thickness of the molecular layer, and the concentration of spins within that layer, we can determine how many spins are in the sensor's sensing volume (Figure 2.4c). The NV centers used in the described experiments in Chapter 2 are in a diamond with a crystal plane of [001], adding an angle of 54.7° between the NV axis and the axis perpendicular to the surface. This angle would cause a small change in the size of the sensing volume and, therefore, also in the number of molecules in this sensing volume.

B.3 Isolating dipolar decoupling with Ramsey correlation

The Ramsey correlation sequence suggested in Section 2.2 consists of four $\frac{\pi}{2}$ pulses applied on the NV center. To understand the final outcome of the pulse sequence, we will describe the state of the sensor at the RWA after every pulse, and we will use the NV Hamiltonian in the RWA as written in equation B.6, where ΔB is any DC magnetic field or detuning from the rotating frame frequency, σ_z^{NV} and σ_z^e are the angular momentum matrices along $\hat{z}$ for the NV electron spin and molecule electron spin, respectively, and ω_{dd} is the dipolar coupling given by- $\omega_{dd} = \frac{\gamma_{NV}\gamma_{CuPc}\mu_B\hbar}{4\pi|r|^3}\left[3(\cos^2(\theta_r)-1\right]$.

$$\mathcal{H}_{\mathrm{rot}} = \Delta B\sigma_z^{\mathrm{NV}} + \Delta_e\sigma_z^e + \omega_{dd}\sigma_z^e\sigma_z^{\mathrm{NV}} \tag{B.6}$$

After the first pulse, the NV center is at a superposition state $|\psi_{\mathrm{NV}}\rangle = |0\rangle + |1\rangle$. During the first free evolution time $\tau/2$, the state of the NV center accumulates a phase according to the Hamiltonian of the system, and the NV center state gains a phase- $|\psi_{\mathrm{NV}}\rangle = |0\rangle + e^{i\varphi_1}|1\rangle$, where $\varphi_1 = \frac{\tau}{2}\left(\gamma\Delta B + A_n + \gamma\delta B + \omega_{dd}\,|\sigma_z^e|\right)$. The operator $|\sigma_z^e|$ will result in one of the eigenstates of the target electron spin- $\pm\frac{1}{2}$ reflecting the state of the electron during this evolution time. We take the absolute value of the eigenstate because of the symmetry of the measurement, where we will show that the interaction flips a sign in the second part of the pulse sequence.

Pulse number two (pulse illustration is in Figure 2.6b) projects the state to the readout axis. The state just before projection has the accumulated phase during the interaction time (Equation B.7a). After the second pulse, the spin is projected to one of the eigenstates of the sensor, and the phase translates to a change in the amplitude of the state (Equation B.7b). The phase θ is the phase of the second $\pi/2$ pulse (for phase $\hat{x} \to \theta = 0$ and for phase $\hat{y} \to \theta = \pi/2$). The "leftover" state on the equator will keep accumulating phase during the mixing time φ_m; however, as the mixing time is longer than the decoherence time (T_2), it will disappear. The relaxation time T_1 of the sensor

is typically two orders of magnitude longer than the mixing time. Therefore, we can neglect its effect. Considering all these effects, the state during the mixing time will be as written in Equation B.7b.

$$|\psi_{\mathrm{NV}}\rangle = \begin{array}{c} \cos(\theta)\left[e^{\tau_m/T_2}\sin\left(\varphi_1\right)\left(|0\rangle + e^{i\varphi_m}|1\rangle\right) + e^{\tau_m/T_1}\cos\left(\varphi_1\right)|1\rangle\right] \\ +\sin(\theta)\left[e^{\tau_m/T_2}\cos\left(\varphi_1\right)\left(|1\rangle + e^{i\varphi_m}|0\rangle\right) + e^{\tau_m/T_1}\sin\left(\varphi_1\right)|0\rangle\right] \end{array} \tag{B.7a}$$

$$|\psi_{\mathrm{NV}}\rangle = \cos(\theta)\cos\left(\varphi_1\right)|1\rangle + \sin(\theta)\sin\left(\varphi_1\right)|0\rangle \tag{B.7b}$$

The chirp pulse addressing the target electron spin is applied during the mix time, between pulses two and three. The pulse flips the state of the electron spin, which will simply change the sign of the interaction to minus the interaction from the first evolution time. The third pulse drives the sensor again to superposition but with a smaller amplitude and different phase -

$$|\psi_{\mathrm{NV}}\rangle = \left[\cos\left(\varphi_1\right)\cos(\theta) + \sin\left(\varphi_1\right)\sin(\theta)\right]\left(|0\rangle - e^{-i\theta}|1\rangle\right)$$

In this state, the sensor again accumulates a phase-

$$|\psi_{\mathrm{NV}}\rangle = \left[\cos\left(\varphi_1\right)\cos(\theta) + \sin\left(\varphi_1\right)\sin(\theta)\right]\left(|0\rangle - e^{i\varphi_2}e^{-i\theta}|1\rangle\right)$$

Where the second phase is - $\varphi_2 = \frac{\tau}{2}\left(\gamma\Delta B + A_n + \gamma\delta B - \omega_{dd}\left|\sigma_z^e\right|\right)$ with an opposite sign to the dipolar interaction due to the chirp pulse that flipped the electron state.

Finally, the fourth pulse is applied to project the state back to the read-out axis using an $\hat{x}$ phase pulse. To see the outcome of the measurement, we should consider the phase of the pulses used in the second and third pulses. The purpose of this measurement is to isolate the dipolar coupling of the sensor and the target spin. We will show that by applying this measurement scheme twice with the second and third pulses having the $\hat{x}$ phase one time and the $\hat{y}$ phase the second, we can add the outcomes to isolate only the dipolar coupling. The state for each of the cases before projecting it to the read-out axis is presented in Equation B.8a.

$$\begin{aligned} |\psi_{NV_{\hat{x}\hat{x}}}\rangle &= \cos\left(\varphi_1\right)\left(|0\rangle - e^{i\varphi_2}|1\rangle\right) \\ |\psi_{NV_{\hat{y}\hat{y}}}\rangle &= \sin\left(\varphi_1\right)\left(|0\rangle + ie^{i\varphi_2}|1\rangle\right) \end{aligned} \tag{B.8a}$$

$$
\begin{aligned}
|\psi_{NV_{\hat{x}\hat{x}}}\rangle &= \cos\left(\varphi_1\right)\cos\left(\varphi_2\right)|0\rangle \\
|\psi_{NV_{\hat{y}\hat{y}}}\rangle &= \sin\left(\varphi_1\right)\sin\left(\varphi_2\right)|1\rangle
\end{aligned}
\tag{B.8b}
$$

Projecting these states to the read-out axis will result in one of the eigenstates of the NV center (Equation B.8b). After read-out, it will result with the cosine or sine signals of the accumulated phase (Equation B.9a). Subtracting the two outcomes and using a trigonometric identity will give the desired result of the isolated dipolar coupling (Equation B.9b).

$$
\begin{aligned}
\langle 0|\psi_{NV_{\hat{x}\hat{x}}}\rangle &= S(\varphi = x) = \frac{\cos\left(\varphi_1-\varphi_2\right)+\cos\left(\varphi_1+\varphi_2\right)}{2} \\
\langle 1|\psi_{NV_{\hat{y}\hat{y}}}\rangle &= S(\varphi = y) = -\frac{\cos\left(\varphi_1-\varphi_2\right)-\cos\left(\varphi_1+\varphi_2\right)}{2}
\end{aligned}
\tag{B.9a}
$$

$$
\langle 0|\psi_{NV_{\hat{x}\hat{x}}}\rangle - \langle 1|\psi_{NV_{\hat{y}\hat{y}}}\rangle = S(\varphi = x) - S(\varphi = y) = \cos\left(\varphi_1 - \varphi_2\right) = \cos\left(\omega_{dd}\right) \tag{B.9b}
$$

B.4 Noise correlation

The Ramsey correlation sequence has shown a coherence time longer than T_2^*, the coherence time of a regular Ramsey sequence. In addition, it has shown a gain of coherence at specific correlation times, which we attribute to the correlation with AC magnetic fields, such as the carbon nuclear spin in the lattice. To understand the mechanism of noise correlation, we derived the expected signal of a single iteration of uncorrelated noise and correlated noise at different correlation times (correlated or uncorrelated to the noise). To account for the averaged nature of the NV sensor, we then integrate the signal with the remaining noise over a Gaussian distribution of the noise to receive the expected decaying signal.

We consider three noise sources: First, an AC field correlated noise. For this derivation, we will use the carbon nuclear spin, with $T_{\mathrm{Corr}} = nT_{\mathrm{C}}$. Second, a DC field noise fluctuates with the measurement timescale $\partial B_{\mathrm{Corr}}$. Third, an uncorrelated noise ∂b. The second noise, the fluctuating DC field $\partial B_{\mathrm{Corr}}$, is the main source for coherence gain after T_2^*. This noise has no specific time characteristics. However, if we assume that the field $\partial B_{\mathrm{Corr}}$ is constant through a single iteration, we can write the expected signal for both measurements ($\varphi = x/y$) in Equation B.10.

$$
\begin{aligned}
S(\varphi = x) = \cos(\Phi_1 - \Phi_2) + \cos(\Phi_1 + \Phi_2) = \\
\cos((\omega_{dd} + \gamma\delta b_1)\tau) + \cos((\gamma\Delta B + A_n + \gamma\delta B_{\text{Corr1}})\tau) \\
S(\varphi = y) = -\sin(\Phi_1 - \Phi_2) + \sin(\Phi_1 + \Phi_2) = \\
-\cos((\omega_{dd} + \gamma\delta b_2)\tau) + \cos((\gamma\Delta B + A_n + \gamma\delta B_{\text{Corr2}})\tau)
\end{aligned}
\tag{B.10}
$$

The noise correlated with the measurement times cycle is canceled when the phases of the two interaction periods are subtracted. However, it remains when they are added together with any other DC magnetic field. In contrast to the other DC fields, this noise is not the same between iterations and even between both measurements of $\varphi = x/y$. Therefore, when adding the measurements of different phases $\varphi = x/y$ and adding all repetitions, we can treat the noise δB_{Corr} as a Gaussian distributed noise and integrate over the noise to result with an exponential decay with a decay constant of $\Gamma_{B_{\text{Corr}}}$ (similar to Equation 2.4b with $\alpha_2 = 1/\Gamma_{B_{\text{DC}}}$).

The subtracted phases still have noise from any uncorrelated magnetic fluctuations δb. Therefore, the subtracted phase component after subtracting the measurements of different phases $\varphi = x/y$ and adding all repetitions will result in exponential decay. However, this signal would be integrated over a different Gaussian distribution of the noise where the correlated noise is factored out and, thus, the expected decay constant will be higher Γ_b (similar to Equation 2.4a with $\alpha_1 = 1/\Gamma_b$).

Finally, the AC field correlated noise has a similar mechanism to the δB_{Corr} noise, with one exception. The coherence gain has time reoccurrence for any integer multiplication of the correlated time $T_{\text{Corr}} = nT_{\text{C}}$[97]. Figure B.2 illustrates the difference between a correlated noise that is gaining the same phase at both interaction periods for each single iteration (upper) compared to an uncorrelated noise (lower); this picture helps to gain intuition on the effect.

To derive the expected phase of a single iteration, we consider the phase accumulated due to the AC-correlated noise at the first and second interaction periods. For now, we will ignore other phase sources for simplicity. The phase in the first period will be $\Phi_1 = 2\pi(f_{\text{C}}\frac{\tau}{2})$ and the phase of the second period would be $\Phi_2 = 2\pi(f_{\text{C}}\frac{\tau}{2} + f_{\text{C}}T_{\text{Corr}})$. Together, we can write the outcome of a single iteration as the addition and subtracted phases (Equation B.11a).

$$
\begin{aligned}
S(\varphi = x, \tau = \tau_{\mathrm{fix},T_{\mathrm{Corr}}}) = \\
\cos(-2\pi f_{\mathrm{C}} T_{\mathrm{Corr}}) + \cos(2\pi(\sum f_{\mathrm{C}}^{1} \tfrac{\tau}{2} + f_{\mathrm{C}} T_{\mathrm{Corr}})) \\
S(\varphi = y, \tau = \tau_{\mathrm{fix},T_{\mathrm{Corr}}}) = \\
-\cos(-2\pi f_{\mathrm{C}} T_{\mathrm{Corr}}) + \cos(2\pi(\sum f_{\mathrm{C}}^{2} \tfrac{\tau}{2} + + f_{\mathrm{C}} T_{\mathrm{Corr}}))
\end{aligned}
\tag{B.11a}
$$

$$
\begin{aligned}
S(\varphi = x/y, T_{\mathrm{Corr}}) &= \pm \cos(-2\pi f_{\mathrm{C}} T_{\mathrm{Corr}}) \\
&\quad + \int e^{-\Gamma \sum f_{\mathrm{C}} (\sum f_{\mathrm{C}})^2} \left[\cos(2\pi(\sum f_{\mathrm{C}} \frac{\tau}{2} + f_{\mathrm{C}} T_{\mathrm{Corr}}))\right] d \sum f_{\mathrm{C}} \\
&= \pm \cos(f_{\mathrm{C}} T_{\mathrm{Corr}}) + e^{\frac{\tau^2}{4\Gamma \sum f_{\mathrm{C}}}} \cos(f_{\mathrm{C}} T_{\mathrm{Corr}})
\end{aligned}
\tag{B.11b}
$$

$$
S(T_{\mathrm{Corr}}) = S(\varphi = x) - S(\varphi = y) = \cos(f_{\mathrm{C}} T_{\mathrm{Corr}}) \tag{B.11c}
$$

Both terms have the phase of the AC signal from the correlation time, resulting in an oscillation function in T_{Corr} with a frequency of f_{C}. However, the second term also has a residual phase $\sum f_{\mathrm{C}}$, which is changing between iterations. The final signal of the measurement is given after subtracting or adding the separate phase iterations and averaging over all repetitions. The order of these operations can be switched. Starting with averaging over all repetitions for each phase measurement $\varphi = x/y$, we are adding up all coherent signals and averaging the noise signal by integrating over the signal with

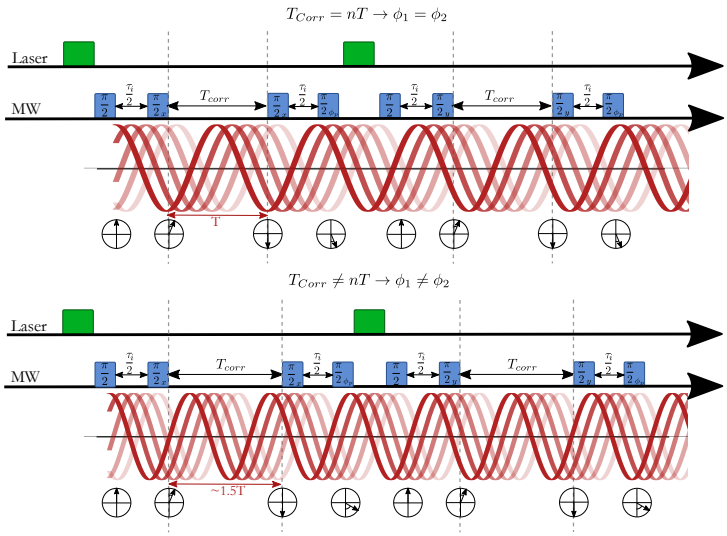

Figure B.2: Illustration of an AC field correlated (upper with $T_{\mathrm{Corr}} = T$) and uncorrelated (lower with $T_{\mathrm{Corr}} \simeq 1.5T$) with the Ramsey correlation sequence

a Gaussian distribution of the noise (Equation B.11b).

The result is a coherent oscillating function and an oscillating function exponentially decaying. Now, subtracting the $\varphi = x/y$ measurement will result only in the oscillating function (Equation B.11c). The result in Equation B.11c is incomplete. Other noise sources, such as relaxation and fast fluctuating magnetic noise, are still causing a decay of the averaged signal and are not included in this derivation.

C

Experimental effort toward single MSQ sensing

C.1 Preliminary results of CuPc samples

The first studied sample of CuPc molecule layer consisted of a highly dense MSQ layer, where 100% of the material evaporated onto the surface comprised CuPc molecules. Beginning with such a dense sample aimed to amplify the impact of the chirp pulse. Notably, the electron spin state of the molecule will only flip when occupying one of the frequencies addressed by the chirp pulse. Therefore, with a greater number of molecules present on the surface, the likelihood of more molecules being flipped and contributing to the signal increases. These measurements were conducted within the cryogenic confocal setup located in the laboratory of Prof. Amir Yacoby at the Applied Physics Department, Harvard University. This setup was a temporary alternative due to technical issues with the cryogenic setup in the lab, and has a high magnetic field of up to 1300 G at an average temperature of 5 K and pressure on the order of $1 \cdot 10^{-6}$ bar.

A total of five NV centers were scanned. A notable observation was the change in decay time when the chirp pulse was applied to the free electron resonance frequency. This phenomenon was observed in four out of the five NVs, while the fifth NV was not measured with the chirp pulse applied to the electron spin resonance frequency.

The enhanced effect observed at 5 K can be attributed to the longer relaxation time (T_1) of the free electrons, thereby reducing noise and negating the absence of an effect when the electron spin is flipped due to relaxation during the measurement, rather than actively by the chirp pulse. Figure C.1a illustrates the percent change in decoherence time depicted in blue bars. Additionally, Figure C.1b showcases an example of chirp DEER on and off applied to the free electron resonance frequency for NV 1.

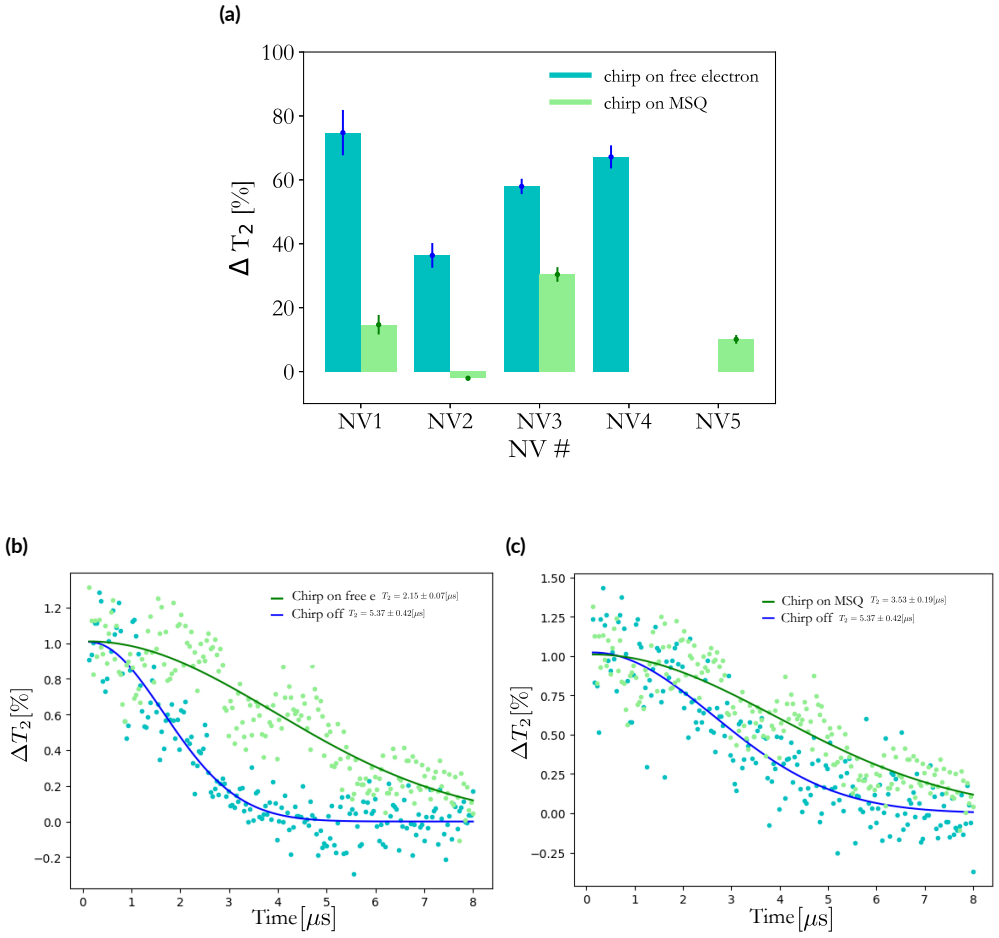

Figure C.1: (a) Change in the decay time between chirp DEER on and off where the chirp pulse was applied on the free electron spin resonance frequency (blue bars) and where the chirp pulse was applied only on the MSQ resonance frequencies (green bars). The measurements were done in a 700 Gauss magnetic field and with a chirp pulse width of 600 MHz. (b) Example data from NV1 of chirp DEER on (blue) off (green) as the chirp was applied on the free electron resonance frequency. (c) Example data from NV1 of chirp DEER on (blue) off (green) as the chirp was applied on the MSQ resonance frequency.

Furthermore, a change in decay time between chirp DEER on and off, specifically when the chirp is solely applied to the molecule resonance frequencies, excluding the free electron resonance frequency, would signify interaction between the NV center and the MSQs on the surface. Figure C.1a illustrates the change in decoherence time for this scenario depicted in green bars. Moreover, Figure C.1c presents an example of chirp DEER on and off applied to the molecule electron resonance frequencies for NV 1. It is evident that the effect from the chirp pulse, when solely applied to the MSQ, is considerably smaller. This diminished effect can be attributed to the shorter relaxation time of the concentrated molecules' spins[62]. Additionally, the partial spectrum addressed by the chirp further diminishes the signal.

The second sample analyzed featured the lowest concentration achievable under the evaporation limitations to attain the longest relaxation time for the MSQ electron spin[62]. This sample comprised of 1% CuPc evaporated simultaneously with H_2Pc molecules on a diamond with nitrogen atoms implanted to an average depth of 10 nm. Six NVs were systematically scanned within the cryogenic confocal setup in our lab under a magnetic field of $65 - 68$ G. No oscillations or change in decay was evident in any of the scanned NV centers. An analysis of the expected number of molecules within the sensing volume of the sensor revealed that for a 1% concentration and an average depth of 10 nm almost no molecules with electron spins are expected to be in the sensor's sensing volume (see Figure 2.4c for the expected number of molecules in 10% of electron spin molecules).

These two experiments and the analysis done afterward led us to the parameters of 10% CuPc and 5 nm deep NV centers as used in the sample scanned in Section 2.3.3.

C.2 Vanadium based MSQs

As part of the search for an MSQ to study, we have also considered vanadium-based molecules synthesized and studied in the group of Danna Freedman at MIT. These molecules were reported to achieve very long coherence times also at relatively high temperatures[60] and in a spin-free solution. The molecules we examined are $V(C_3S_4O)_3^{2-}$ molecules (illustration in Figure C.2a) with vanadium nuclear spin of $I = 7/2$ and hyperfine couplings of $A_{xx} = A_{yy} = -258$ MHz and $A_{zz} = 6$ MHz with no other nuclear spins in the molecule.

To place these molecules on the surface of the diamond, we had to use drop-casting of the molecules inside a toluene:dimethylformamide (DMF) mixture of 1:1. After drop-casting, the solvent evaporates, leaving the molecules on the surface. To check

the molecules on the surface, we used XPS scans with the help of Dr. Hagai Cohen.

First, we dropcasted two solutions of $V(C_3S_4O)_3^{2-}$ molecules in toluene/DMF at

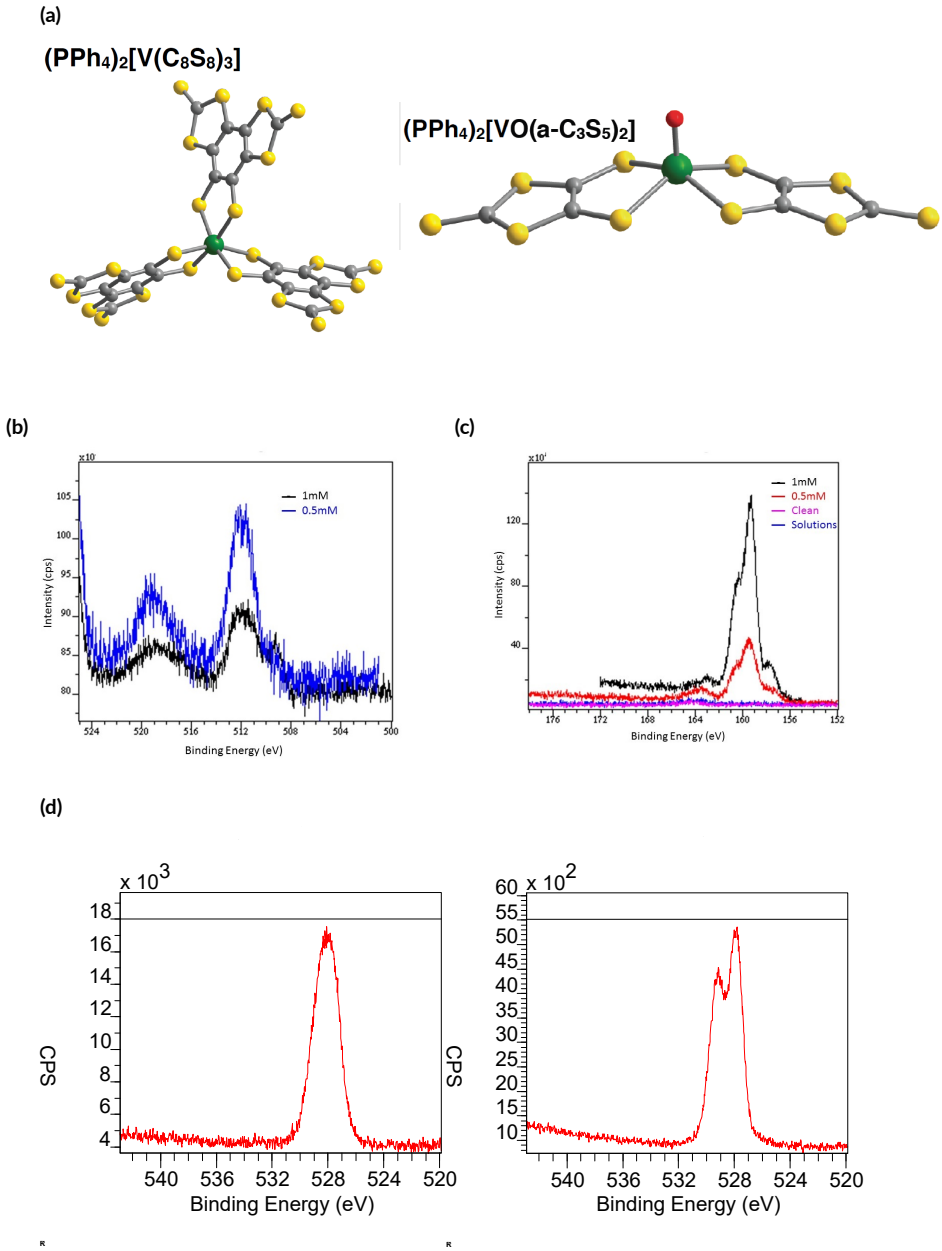

Figure C.2: (a) Illustration of $V(C_3S_4O)_3^{2-}$ (left) and $VO(\alpha - C_3S_5)_2^{2-}$ (right) (b-c) XPS spectra of diamond samples "1 mM", "0.5 mM", "solution" and "clean" of vanadium (b) and sulfor (c) (d) Oxygen XPS spectrum of $V(C_3S_4O)_3^{2-}$ (left) and $VO(\alpha - C_3S_5)_2^{2-}$ (right).

concentrations of 1 mM and 0.5 mM on two diamonds, and left to dry in air conditions inside a chemical hood overnight (samples referred to as "1 mM" and "0.5 mM"). The samples were analyzed with XPS and compared to an XPS measurement of a clean diamond and a diamond with only a toluene/DMF solution (control samples referred to as "clean" and "solution"). The XPS spectra of vanadium and sulfur of all four samples are shown in Figures C.2b and C.2c respectively.

The sulfur spectra (Figure C.2c) are a clear proof that the molecules are on the surface of samples "1 mM" and "0.5 mM", since the "clean" and "solution" samples showed almost no sulfur. The vanadium spectra (Figure C.2b) showed higher amounts of vanadium on the "0.5 mM" sample compared to the "1 mM" sample. This result might suggest that with high concentrations a large amounts of the molecules are washed from the diamond with the solution. Further analysis of the vanadium spectra showed two main oxidation states of the vanadium. A possible explanation for this result is that some of the molecules go through a chemical transformation, for example, "losing" one ligand once formed a bond with the surface.

To avoid the problem of a broken molecule, we considered using similar molecules with two ligands instead of three and a planar shape, which should also be more compatible with the diamond's flat surface. The two ligand molecules we considered are $VO\left(\alpha - C_3S_5\right)_2^{2-}$. We used XPS to compare the $V\left(C_3S_4O\right)_3^{2-}$ (molecule 2) and $VO\left(\alpha - C_3S_5\right)_2^{2-}$ (molecule 1). The major difference between the two species was in the oxygen spectrum in Figure C.2d. The oxygen spectrum of the planar molecules (molecule 1) had two peaks, which indicated a carboxylic acid group (COOH) and alcoholic group (COH), whereas the spectrum of the other molecule (2) had one peak, only the alcohol group. Alcohol groups can also be found on a clean diamond, therefore expected to be found. However, the carboxyl group indicates a reaction caused on the surface of the diamond with the oxygen atom connected to the vanadium atom in the planar molecule.

Apart from the difference in the oxygen spectrum, we analyzed the spectrum of the sulfur and vanadium atoms. We examined the ratio between the atoms (vanadium/sulfur) on the surface, which should be the same ratio as in the molecule- 0.1 and 0.12 for molecules 1 and 2, respectively. The ratio calculated for both molecules was higher than expected- 0.2 and 0.21 for molecules 1 and 2, respectively. This finding indicates that the molecules break from the ligand groups, which leaves the vanadium atoms unconnected. The molecules are known to be very stable in crystal form and in solution form when the solution is clean from water. Therefore, we hypothesize that the ligand braking is due to the interaction of the molecule with water vapor in the air.

Because of the unknown state of the molecules on the surface after drop-casting, we chose not to use them in NV sensing experiments.

D

Analytical derivations of adiabaticity

D.1 Chirp adiabaticity factor for linearly changing frequency pulse

To get a numerical representation of the adiabaticity of the pulse, we use the Q factor describing the ratio between the rate of change $d\alpha/dt$ of frequencies compared to the effective field $\omega_{eff} = B_{eff}/\gamma$ of the chirp pulse. To calculate the Q factor term in Equation 3.1b for a linearly changing frequency pulse, we will estimate $d\alpha/dt$ and ω_{eff}.

The magnetic field applied to the system is

$$B_{total}(t) = \begin{bmatrix} B^{(1)}\cos(\omega(t)) \\ B^{(1)}\sin(\omega(t)) \\ B^{(0)} \end{bmatrix}$$

Where $\omega(t) = kt$ for a linearly changing frequency and $k = \Delta\Omega/\Delta T$ is the rate of the frequency change, so $\Delta\Omega$ is the total span of frequencies applied in the pulse and $\Delta T = T_p$ is the total time that the pulse is applied. Invoking the doubly rotating frame that rotates with the applied driving field, we can write the effective magnetic field in

the system-

$$B_{total}(t) = \begin{bmatrix} B^{(1)} \\ B^{(1)} \\ B^{(0)} - \frac{\omega(t)}{\gamma} \end{bmatrix}$$

This picture shows the rate of change in the $B^{(1)}$ field, denoted as $d\alpha/dt$. The changing angle (α) can also be described by the inverse tangent of the magnetic fields - $\alpha = \tan^{-1}\left(\frac{B^{(1)}}{B^{(0)}-\omega(t)/\gamma}\right)$. Now, we can calculate the adiabaticity factor of a linearly changing frequency pulse.

$$\begin{aligned} Q &= \frac{\omega_{eff}}{d\alpha/dt} \\ &= \frac{\sqrt{(\gamma B^{(0)} - \omega(t))^2 + (\gamma B^{(1)})^2}}{d/dt\left(\tan^{-1}\left(\frac{B^{(1)}}{B^{(0)}-\omega(t)/\gamma}\right)\right)} \\ &= \frac{\sqrt{(\gamma B^{(0)} - \omega(t))^2 + (\gamma B^{(1)})^2}}{\frac{d/dt(\omega(t))\gamma B^{(1)}}{(\gamma B^{(0)}-\omega(t))^2+(\gamma B^{(1)})^2}} \\ &= \frac{\sqrt{(\gamma B^{(0)} - \omega(t))^2 + (\gamma B^{(1)})^2}}{\frac{k\gamma B^{(1)}}{(\gamma B^{(0)}-kt)^2+(\gamma B^{(1)})^2}} \end{aligned}$$

The minimal adiabaticity can be found when the frequency $\omega(t)$ gets to resonance. In that case, the effective field is minimal, and the change angle is maximal. Therefore we will determine a high adiabaticity when this term is larger than 1. For full passage we reach resonance at $T_p/2$ where $B^{(0)} - \omega(T_p/2) = 0$ and resulting with the Q adiabaticity in Equation D.1. Where we used the Rabi frequency of the system, that is $2\pi\nu = \gamma B^{(1)}$ and $\Delta\Omega = 2\pi\Delta F$.

$$\begin{aligned} Q &= \frac{\gamma B^{(1)}}{\frac{k\gamma B^{(1)}}{(\gamma B^{(1)})^2}} = \frac{\gamma B^{(1)}}{\frac{\Delta\Omega/T_p}{\gamma B^{(1)}}} = \frac{(2\pi\nu)^2}{\Delta\Omega/T_p} \\ &= \frac{(2\pi\nu)^2}{2\pi\Delta F/T_p} = \frac{2\pi\nu^2 T_p}{\Delta F} \end{aligned} \tag{D.1}$$

E

Adaptive phase estimation full adaptive scheme

E.1 Adaptive phase calculation

Taking Eq. 4.3a and the Ramsey model (Eq. 4.3b), we derive in this appendix the optimal phase in the adaptive case. To this end, we define here the sensor's threshold (α) and visibility (V) as follows-

$$\begin{aligned} \alpha &= \tfrac{1}{2}\left[P_d(1|m_0) + P_d(1|m_1)\right] \\ V &= \tfrac{P_d(1|m_0) - P_d(1|m_1)}{P_d(1|m_0) + P_d(1|m_1)} e^{(\tau/T_2^*)^2} \end{aligned}$$

For the optimal phase, we use the Fisher information as discussed in Section 4.3. To calculate this we use the model - $L(f_B, \theta) = \alpha\left[1 + V\cos\left(2\pi f_B \tau - \theta\right)\right]$ and calculate its derivative

$$L'(f_B, \theta) = \frac{\partial}{\partial f_B} L(f_B, \theta) = -2\alpha V \pi \tau \sin(2\pi f_B \tau - \theta).$$

Next, we use the binomial probability distribution to write down the mean and vari-

ance,

$$\mu_r = E[r|f_B] = R \cdot L(f_B, \theta)$$
$$\sigma_r^2 = E\left[\left(r - \mu_r\right)^2 |f_B\right] = R \cdot L(f_B, \theta)\left[1 - L(f_B, \theta)\right].$$

We can approximate $L(f_B, \theta) \equiv L \simeq \frac{r}{R} + \Delta$ if $\Delta \ll 1$, and then get an expression for the variance in leading orders of $\frac{r}{R}$:

$$\begin{aligned}\sigma_r^2 &= R \cdot L(f_B, \theta)\left[1 - L(f_B, \theta)\right] = RL - RL^2 = R\left[\left(\frac{r}{R} + \Delta\right) - \left(\frac{r}{R} + \Delta\right)^2\right] = \\ &= R\left[\left(\frac{r}{R} + \Delta\right) - \left(\frac{r^2}{R^2} + 2\Delta\frac{r}{R} + \Delta^2\right)\right] \approx R\left[\left(\frac{r}{R} + \Delta\right) - \frac{r^2}{R^2} - 2\Delta\frac{r}{R}\right] = \\ &= R\left[L - \frac{r^2}{R^2} - 2\left(L - \frac{r}{R}\right)\frac{r}{R}\right] = R\left[L + \frac{r^2}{R^2} - 2\frac{r}{R}L\right] = R\left[L\left(1 - 2\frac{r}{R}\right) + \frac{r^2}{R^2}\right]\end{aligned}$$

Now, we define the logarithm of the model (likelihood) function:

$$K(r, f_B) \equiv \log P(r|f_B) = \log\begin{pmatrix} R \\ r \end{pmatrix} + r\log L(f_B, \theta) + (R - r)\log\left(1 - L(f_B, \theta)\right)$$

and so

$$\frac{\partial}{\partial f_B}K(r, f_B) = \frac{rL'}{L} - \frac{(R - r)L'}{1 - L} = \left[\frac{r}{L} - \frac{R - r}{1 - L}\right]L' = \left[\frac{r - RL}{L(1 - L)}L'\right] = \frac{R}{\sigma_r^2}(r - \mu_r)L'(f_B, \theta).$$

As we wrote in Section 4.3, the Fisher information can now be explicitly calculated,

$$\begin{aligned}I(f_B) &= E\left[\left(\frac{\partial}{\partial f_B}K(r, f_B)\right)^2\right] = E\left[(r - \mu_r)^2\right]\frac{R^2}{\sigma_r^4}\left(L'(f_B, \theta)\right)^2 = \frac{R^2}{\sigma_r^2}\left(L'(f_B, \theta)\right)^2 \\ &\approx \frac{R\left(L'(f_B, \theta)\right)^2}{\frac{r^2}{R^2} + \left(1 - 2\frac{r}{R}\right)L(f_B, \theta)} = 4R\alpha^2V^2\pi^2\tau^2\frac{\sin^2\left(2\pi f_B\tau - \theta\right)}{\frac{r^2}{R^2} + \left(1 - 2\frac{r}{R}\right)\alpha\left[1 + V\cos\left(2\pi f_B\tau - \theta\right)\right]}\end{aligned}$$

The last term can be written in a more compact form by denoting

$$A = \frac{r^2}{R^2} + \left(1 - 2\frac{r}{R}\right)\alpha$$
$$B = \left(1 - 2\frac{r}{R}\right)\alpha V$$
$$C = 4R\alpha^2V^2\pi^2\tau^2,$$

such that,

$$I(f_B) = C\frac{\sin^2(2\pi f_B\tau - \theta)}{A + B\cos(2\pi f_B\tau - \theta)}$$

We maximize the Fisher information (or minimize the Cramér-Rao bound):

$$\frac{\partial}{\partial\theta}I(f_B) = 0$$

with two solutions. The first one is a minimum with $\theta = 2\pi f_B\tau$ and the second solution is $A\cos(2\pi f_B\tau - \theta) + B = 0$. Using $\hat{f}_B = E[f_B]$, gives:

$$\theta_{\text{opt}} = 2\pi\hat{f}_B\tau - \cos^{-1}\left(\frac{-B}{A}\right),$$

F

Strong magnetic gradient for individual molecule driving

F.1 Superconducting micro-coils for local magnetic field gradients

For the ambitious goal of sensing a single MSQ with the NV center, we planned to create a spectral separation between close MSQs. To this end, we can use a magnetic field gradient, as was shown in the past, to allow spatial separation of electron spins[65,64]. In this work, we aimed to achieve a stronger gradient that will provide spatial separation of two-electron spins 10 nm apart. This gradient can separate spectrally free electrons; however, due to the broad spectrum of the MSQs studied, it is not relevant to this molecular qubit system but rather to a narrowband one.

The magnetic gradient I designed was a structure of small micro-coils in an anti-Helmholtz configuration, fabricated from a superconducting material. The use of superconducting material allows for a high current without heating the sample under the cryogenic environment. On top of it, a small structure of the micro-coils will also increase the local gradient due to the larger magnetic field close to the coils.

A prototype of the micro-coil structure was printed on a silicon substrate from a Molybdenum Rhenium alloy (50:50) (Figure F.1a). A four-wire configuration was connected to the coils to estimate the critical current allowed with the micro-coils. The

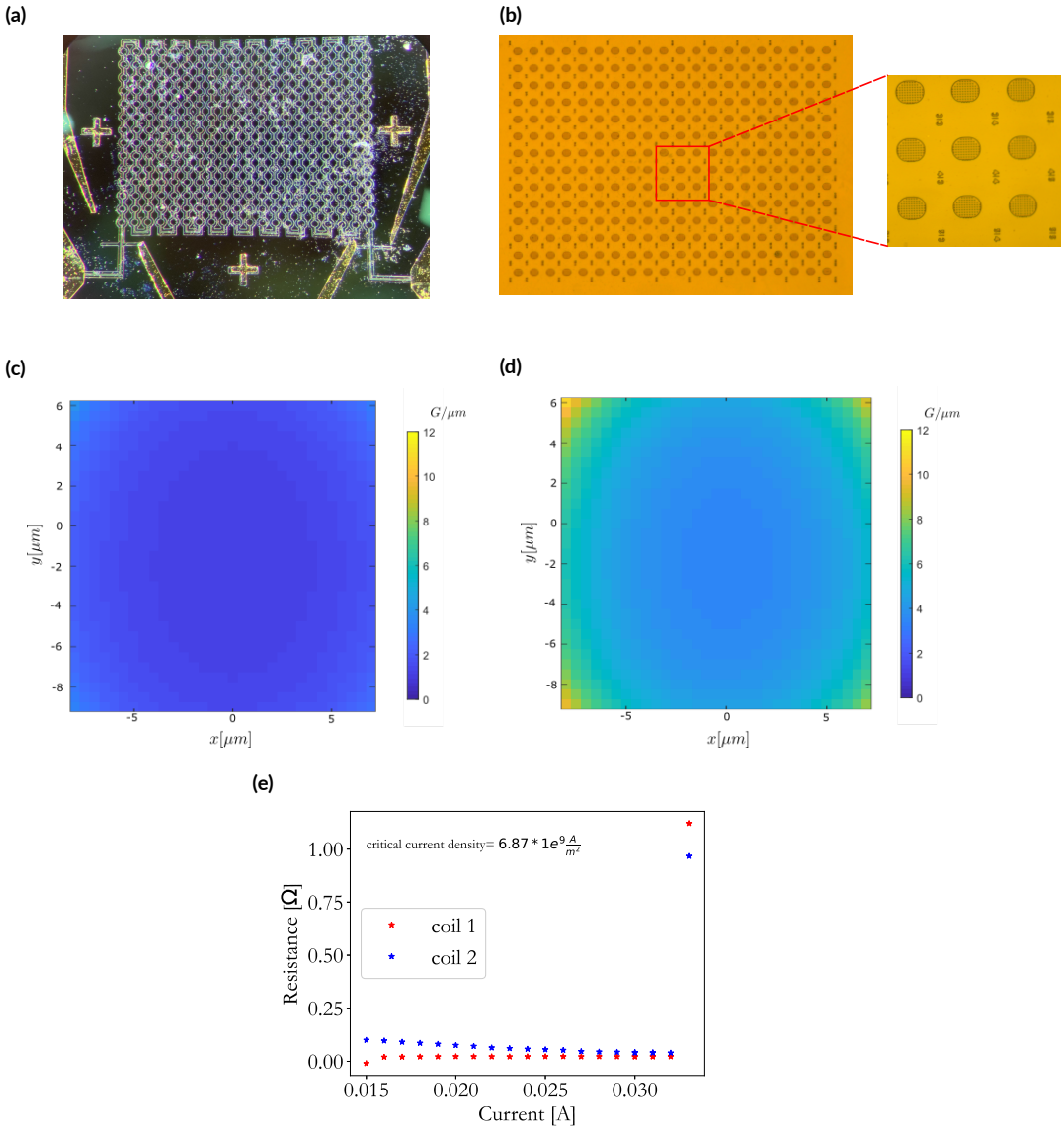

Figure F.1: (a) Image of a micro-coil design printed on a silicon wafer with Mo-Re aolly spatered on it. (b) Image of a specially designed diamond with pillars located in small circles to fit the micro-coils design. (c-d) Simulation of a micro-coil with a low current of $0.03\,\mathrm{mA}$ (c) and high current of $0.1\,\mathrm{mA}$ (d). (e) Resistance measurement of the micro-coil imaged in (a) at low temperature of $4.2\,\mathrm{K}$ and rising amplitude of current.

prototype was then cooled down in a liquid helium Dewar to a temperature of $4.2\,\mathrm{K}$. The transition of the coils to the superconducting phase was clear from the resistance measurement of the coils (Figure F.1e).

The critical current achieved was $30\,\mathrm{mA}$, a current density of $6.87 \cdot 10^9\,\frac{\mathrm{A}}{\mathrm{m}^2}$ for wire

thickness of 0.3 μm and width 8 μm, better than what was reported in the literature [126]. A simulation of the expected gradient under such a critical current resulted in a maximal magnetic field gradient of 4 $\frac{G}{\mu m}$ (Figure F.1c). By linear extrapolation increasing the height of the deposited layer to 1 μm will result in a maximal magnetic gradient field of 12 $\frac{G}{\mu m}$ (Figure F.1d)).

To assess the actual magnetic field gradient, the micro-coils are planned to be printed on the surface of a diamond membrane with pre-etched pillars in arrays of 80 pillars arranged in a circular structure (Figure F.1b). The diamond with the printed superconducting micro-coils will be measured in the cryogenic confocal set-up. We will use the NV centers in the diamond to measure the actual magnetic field gradient we created with the micro-coils.

Bibliography

[1] O. E. Dictionary, *Sensing* (Oxford University Press, 2023).

[2] C. L. Degen, F. Reinhard, and P. Cappellaro, "Quantum sensing," Rev. Mod. Phys. **89**, 035002 (2017).

[3] J. P. Dowling and G. J. Milburn, "Quantum technology: the second quantum revolution," Philosophical Transactions of the Royal Society A **361**, 1655 (2003).

[4] N. Aslam, H. Zhou, E. K. Urbach, M. J. Turner, R. L. Walsworth, M. D. Lukin, and H. Park, "Quantum sensors for biomedical applications," Nature Reviews Physics **5**, 157 (2023).

[5] R. Rizzato, N. R. von Grafenstein, and D. B. Bucher, "Quantum sensors in diamonds for magnetic resonance spectroscopy: Current applications and future prospects," Applied Physics Letters **123**, 260502 (2023).

[6] Y. Xu, W. Zhang, and C. Tian, "Recent advances on applications of NV- magnetometry in condensed matter physics," Photonics Research **11**, 393 (2023).

[7] Z. Zhang, H. F. Wen, L. Li, B. Cao, Y. Liu, H. Guo, Z. hao Li, Z. Ma, X. Li, J. Tang, *et al.*, "Temperature dependence of magnetic sensitivity in ensemble NV centers," Japanese Journal of Applied Physics **63**, 062001 (2024).

[8] S. Lin, C. Weng, Y. Yang, J. Zhao, Y. Guo, J. Zhang, L. Lou, W. Zhu, and G. Wang, "Temperature-dependent coherence properties of NV ensemble in diamond up to 600 K," Physical Review B **104**, 155430 (2021).

[9] J. Happacher, J. Bocquel, H. T. Dinani, M. A. Tschudin, P. Reiser, D. A. Broadway, J. R. Maze, and P. Maletinsky, "Temperature-dependent photophysics of single NV centers in diamond," Physical Review Letters **131**, 086904 (2023).

[10] J.-H. Dai, Y.-X. Shang, Y.-H. Yu, Y. Xu, H. Yu, F. Hong, X.-H. Yu, X.-Y. Pan, and G.-Q. Liu, "Quantum sensing with diamond NV centers under megabar pressures," Chinese Physics Letters **39**, 117601 (2022).

[11] V. Ivady, T. Simon, J. R. Maze, I. Abrikosov, and A. Gali, "Pressure and temperature dependence of the zero-field splitting in the ground state of NV centers in diamond: A first-principles study," Physical Review B **90**, 235205 (2014).

[12] A. Hilberer, L. Toraille, C. Dailledouze, M.-P. Adam, L. Hanlon, G. Weck, M. Schmidt, P. Loubeyre, and J.-F. Roch, "Enabling quantum sensing under extreme pressure: Nitrogen-vacancy magnetometry up to 130 Gpa," Physical Review B **107**, L220102 (2023).

[13] W. Zhang, J. Zhang, J. Wang, F. Feng, S. Lin, L. Lou, W. Zhu, and G. Wang, "Depth-dependent decoherence caused by surface and external spins for NV centers in diamond," Physical Review B **96**, 235443 (2017).

[14] K. Ohno, F. Joseph Heremans, L. C. Bassett, B. A. Myers, D. M. Toyli, A. C. Bleszynski Jayich, C. J. Palmstrøm, and D. D. Awschalom, "Engineering shallow spins in diamond with nitrogen delta-doping," Applied Physics Letters **101**, 082413 (2012).

[15] H. Yamano, S. Kawai, K. Kato, T. Kageura, M. Inaba, T. Okada, I. Higashimata, M. Haruyama, T. Tanii, K. Yamada, *et al.*, "Charge state stabilization of shallow nitrogen vacancy centers in diamond by oxygen surface modification," Japanese Journal of Applied Physics **56**, 04CK08 (2017).

[16] S. Sangtawesin, B. L. Dwyer, S. Srinivasan, J. J. Allred, L. V. Rodgers, K. De Greve, A. Stacey, N. Dontschuk, K. M. O'Donnell, D. Hu, *et al.*, "Origins of diamond surface noise probed by correlating single-spin measurements with surface spectroscopy," Physical Review X **9**, 031052 (2019).

[17] M. Doherty, F. Dolde, H. Fedder, F. Jelezko, J. Wrachtrup, N. Manson, and L. Hollenberg, "Theory of the ground-state spin of the NV^- center in diamond," Physical Review B **85**, 205203 (2012).

[18] M. W. Doherty, N. B. Manson, P. Delaney, and L. C. Hollenberg, "The negatively charged nitrogen-vacancy centre in diamond: the electronic solution," New Journal of Physics **13**, 025019 (2011).

[19] J. Larsson and P. Delaney, "Electronic structure of the nitrogen-vacancy center in diamond from first-principles theory," Physical Review B **77**, 165201 (2008).

[20] M. S. Barson, E. Krausz, N. B. Manson, and M. W. Doherty, "The fine structure of the neutral nitrogen-vacancy center in diamond," Nanophotonics **8**, 1985 (2019).

[21] M. W. Doherty, N. B. Manson, P. Delaney, F. Jelezko, J. Wrachtrup, and L. C. Hollenberg, "The nitrogen-vacancy colour centre in diamond," Physics Reports **528**, 1 (2013).

[22] G. Thiering and A. Gali, "Ab initio calculation of spin-orbit coupling for an NV center in diamond exhibiting dynamic Jahn-Teller effect," Physical Review B **96**, 081115 (2017).

[23] J. R. Maze, A. Gali, E. Togan, Y. Chu, A. Trifonov, E. Kaxiras, and M. D. Lukin, "Properties of nitrogen-vacancy centers in diamond: the group theoretic approach," New Journal of Physics **13**, 025025 (2011).

[24] N. Manson and J. Harrison, "Photo-ionization of the nitrogen-vacancy center in diamond," Diamond and Related Materials **14**, 1705 (2005).

[25] N. Aslam, G. Waldherr, P. Neumann, F. Jelezko, and J. Wrachtrup, "Photo-induced ionization dynamics of the nitrogen vacancy defect in diamond investigated by single-shot charge state detection," New Journal of Physics **15**, 013064 (2013).

[26] V. Acosta, A. Jarmola, E. Bauch, and D. Budker, "Optical properties of the nitrogen-vacancy singlet levels in diamond," Physical Review B **82**, 201202 (2010).

[27] M. L. Goldman, A. Sipahigil, M. Doherty, N. Y. Yao, S. Bennett, M. Markham, D. Twitchen, N. Manson, A. Kubanek, and M. D. Lukin, "Phonon-induced population dynamics and intersystem crossing in nitrogen-vacancy centers," Physical Review Letters **114**, 145502 (2015).

[28] M. L. Goldman, M. Doherty, A. Sipahigil, N. Y. Yao, S. Bennett, N. Manson, A. Kubanek, and M. D. Lukin, "State-selective intersystem crossing in nitrogen-vacancy centers," Physical Review B **91**, 165201 (2015).

[29] J. P. Tetienne, L. Rondin, P. Spinicelli, M. Chipaux, T. Debuisschert, J.-F. Roch, and V. Jacques, "Magnetic-field-dependent photodynamics of single NV defects in diamond: an application to qualitative all-optical magnetic imaging," New Journal of Physics **14**, 103033 (2012).

[30] D. A. Hopper, H. J. Shulevitz, and L. C. Bassett, "Spin readout techniques of the nitrogen-vacancy center in diamond," Micromachines **9**, 437 (2018).

[31] D. M. Irber, F. Poggiali, F. Kong, M. Kieschnick, T. Lühmann, D. Kwiatkowski, J. Meijer, J. Du, F. Shi, and F. Reinhard, "Robust all-optical single-shot readout of nitrogen-vacancy centers in diamond," Nature Communications **12**, 532 (2021).

[32] I. I. Rabi, "Space quantization in a gyrating magnetic field," Physical Review **51**, 652 (1937).

[33] J. F. Barry, M. J. Turner, J. M. Schloss, D. R. Glenn, Y. Song, M. D. Lukin, H. Park, and R. L. Walsworth, "Optical magnetic detection of single-neuron action potentials using quantum defects in diamond," Proceedings of the National Academy of Sciences **113**, 14133 (2016).

[34] P. Neumann, I. Jakobi, F. Dolde, C. Burk, R. Reuter, G. Waldherr, J. Honert, T. Wolf, A. Brunner, J. H. Shim, D. Suter, H. Sumiya, J. Isoya, and

J. Wrachtrup, "High-precision nanoscale temperature sensing using single defects in diamond," Nano Letters **13**, 2738 (2013).

[35] K. O. Ho, K. C. Wong, M. Y. Leung, Y. Y. Pang, W. K. Leung, K. Y. Yip, W. Zhang, J. Xie, S. K. Goh, and S. Yang, "Recent developments of quantum sensing under pressurized environment using the nitrogen vacancy (NV) center in diamond," Journal of Applied Physics **129**, 241101 (2021).

[36] M. E. Trusheim and D. Englund, "Wide-field strain imaging with preferentially-aligned nitrogen-vacancy centers in polycrystalline diamond," New Journal of Physics **18**, 123023 (2016).

[37] S. Felton, A. Edmonds, M. E. Newton, P. Martineau, D. Fisher, D. Twitchen, and J. Baker, "Hyperfine interaction in the ground state of the negatively charged nitrogen vacancy center in diamond," Physical Review B **79**, 075203 (2009).

[38] B. Smeltzer, L. Childress, and A. Gali, "^{13}c hyperfine interactions in the nitrogen-vacancy centre in diamond," New Journal of Physics **13**, 025021 (2011).

[39] L. Rondin, J.-P. Tetienne, T. Hingant, J.-F. Roch, P. Maletinsky, and V. Jacques, "Magnetometry with nitrogen-vacancy defects in diamond," Reports on Progress in Physics **77**, 056503 (2014).

[40] E. L. Hahn, "Spin echoes," Physical Review **80**, 580 (1950).

[41] L. Childress, M. Gurudev Dutt, J. Taylor, A. Zibrov, F. Jelezko, J. Wrachtrup, P. Hemmer, and M. Lukin, "Coherent dynamics of coupled electron and nuclear spin qubits in diamond," Science **314**, 281 (2006).

[42] L. M. Pham, S. J. DeVience, F. Casola, I. Lovchinsky, A. O. Sushkov, E. Bersin, J. Lee, E. Urbach, P. Cappellaro, H. Park, *et al.*, "Nmr technique for determining the depth of shallow nitrogen-vacancy centers in diamond," Physical Review B **93**, 045425 (2016).

[43] T. Staudacher, F. Shi, S. Pezzagna, J. Meijer, J. Du, C. A. Meriles, F. Reinhard, and J. Wrachtrup, "Nuclear magnetic resonance spectroscopy on a (5-nanometer)^3 sample volume," Science **339**, 561 (2013).

[44] S. Schmitt, T. Gefen, F. M. Stürner, T. Unden, G. Wolff, C. Müller, J. Scheuer, B. Naydenov, M. Markham, S. Pezzagna, *et al.*, "Submillihertz magnetic spectroscopy performed with a nanoscale quantum sensor," Science **356**, 832 (2017).

[45] E. Schäfer-Nolte, L. Schlipf, M. Ternes, F. Reinhard, K. Kern, and J. Wrachtrup, "Tracking temperature-dependent relaxation times of ferritin nanomagnets with a wideband quantum spectrometer," Physical Review Letters **113**, 217204 (2014).

[46] G. Wang, Y.-X. Liu, J. M. Schloss, S. T. Alsid, D. A. Braje, and P. Cappellaro, "Sensing of arbitrary-frequency fields using a quantum mixer," Physical Review X **12**, 021061 (2022).

[47] I. D. Sahu, R. M. McCarrick, and G. A. Lorigan, "Use of electron paramagnetic resonance to solve biochemical problems," Biochemistry **52**, 5967 (2013).

[48] W. Moerner, Y. Shechtman, and Q. Wang, "Single-molecule spectroscopy and imaging over the decades," Faraday Discussions **184**, 9 (2015).

[49] S. Ishizu, K. Sasaki, D. Misonou, T. Teraji, K. M. Itoh, and E. Abe, "Spin coherence and depths of single nitrogen-vacancy centers created by ion implantation into diamond via screening masks," Journal of Applied Physics **127** (2020), 10.1063/5.0012187.

[50] Y. D. Tsvetkov, A. D. Milov, and A. G. Maryasov, "Pulsed electron–electron double resonance (PELDOR) as EPR spectroscopy in nanometre range," Russian Chemical Reviews **77**, 487 (2008).

[51] B. L. Dwyer, L. V. Rodgers, E. K. Urbach, D. Bluvstein, S. Sangtawesin, H. Zhou, Y. Nassab, M. Fitzpatrick, Z. Yuan, K. De Greve, *et al.*, "Probing spin dynamics on diamond surfaces using a single quantum sensor," PRX Quantum **3**, 040328 (2022).

[52] M. Grinolds, M. Warner, K. De Greve, Y. Dovzhenko, L. Thiel, R. L. Walsworth, S. Hong, P. Maletinsky, and A. Yacoby, "Subnanometre resolution in three-dimensional magnetic resonance imaging of individual dark spins," Nature Nanotechnology **9**, 279 (2014).

[53] L. Schlipf, T. Oeckinghaus, K. Xu, D. B. R. Dasari, A. Zappe, F. F. De Oliveira, B. Kern, M. Azarkh, M. Drescher, M. Ternes, *et al.*, "A molecular quantum spin network controlled by a single qubit," Science Advances **3**, e1701116 (2017).

[54] H. Mamin, M. Sherwood, and D. Rugar, "Detecting external electron spins using nitrogen-vacancy centers," Physical Review B **86**, 195422 (2012).

[55] M. Atzori and R. Sessoli, "The second quantum revolution: role and challenges of molecular chemistry," Journal of the American Chemical Society **141**, 11339 (2019).

[56] A. Gaita-Ariño, F. Luis, S. Hill, and E. Coronado, "Molecular spins for quantum computation," Nature Chemistry **11**, 301 (2019).

[57] A. A. Fursina and A. Sinitskii, "Toward molecular spin qubit devices: Integration of magnetic molecules into solid-state devices," ACS Applied Electronic Materials **5**, 3531 (2023).

[58] D. P. DiVincenzo, "The physical implementation of quantum computation," Fortschritte der Physik: Progress of Physics **48**, 771 (2000).

[59] T. Huang, J. Chang, L. Ma, A. J. Fisher, N. M. Harrison, T. Zou, H. Wang, and W. Wu, "Triplet-mediated spin entanglement between organic radicals: integrating first principles and open-quantum-system simulations," NPG Asia Materials **15**, 62 (2023).

[60] J. M. Zadrozny, J. Niklas, O. G. Poluektov, and D. E. Freedman, "Millisecond coherence time in a tunable molecular electronic spin qubit," ACS Central Science **1**, 488 (2015).

[61] J. M. Zadrozny, J. Niklas, O. G. Poluektov, and D. E. Freedman, "Multiple quantum coherences from hyperfine transitions in a vanadium (IV) complex," Journal of the American Chemical Society **136**, 15841 (2014).

[62] M. Warner, S. Din, I. S. Tupitsyn, G. W. Morley, A. M. Stoneham, J. A. Gardener, Z. Wu, A. J. Fisher, S. Heutz, C. W. Kay, *et al.*, "Potential for spin-based information processing in a thin-film molecular semiconductor," Nature **503**, 504 (2013).

[63] L. Schein-Lubomirsky, Y. Mazor, R. Stöhr, A. Denisenko, and A. Finkler, "Pulsed magnetic field gradient on a tip for nanoscale imaging of spins," arXiv **2409**, 17690 (2024).

[64] H. Zhang, K. Arai, C. Belthangady, J.-C. Jaskula, and R. L. Walsworth, "Selective addressing of solid-state spins at the nanoscale via magnetic resonance frequency encoding," npj Quantum Information **3**, 31 (2017).

[65] K. Arai, C. Belthangady, H. Zhang, N. Bar-Gill, S. DeVience, P. Cappellaro, A. Yacoby, and R. L. Walsworth, "Fourier magnetic imaging with nanoscale resolution and compressed sensing speed-up using electronic spins in diamond," Nature Nanotechnology **10**, 859 (2015).

[66] S. Bayliss, D. Laorenza, P. Mintun, B. Kovos, D. E. Freedman, and D. Awschalom, "Optically addressable molecular spins for quantum information processing," Science **370**, 1309 (2020).

[67] D. W. Laorenza and D. E. Freedman, "Could the quantum internet be comprised of molecular spins with tunable optical interfaces?" Journal of the American Chemical Society **144**, 21810 (2022).

[68] S. Bayliss, P. Deb, D. Laorenza, M. Onizhuk, G. Galli, D. Freedman, and D. Awschalom, "Enhancing spin coherence in optically addressable molecular qubits through host-matrix control," Physical Review X **12**, 031028 (2022).

[69] M. Shiddiq, D. Komijani, Y. Duan, A. Gaita-Ariño, E. Coronado, and S. Hill, "Enhancing coherence in molecular spin qubits via atomic clock transitions," Nature **531**, 348 (2016).

[70] S. Thiele, F. Balestro, R. Ballou, S. Klyatskaya, M. Ruben, and W. Wernsdorfer, "Electrically driven nuclear spin resonance in single-molecule magnets," Science **344**, 1135 (2014).

[71] C. Godfrin, A. Ferhat, R. Ballou, S. Klyatskaya, M. Ruben, W. Wernsdorfer, and F. Balestro, "Operating quantum states in single magnetic molecules: implementation of Grover's quantum algorithm," Physical Review Letters **119**, 187702 (2017).

[72] P. Willke, T. Bilgeri, X. Zhang, Y. Wang, C. Wolf, H. Aubin, A. Heinrich, and T. Choi, "Coherent spin control of single molecules on a surface," ACS Nano **15**, 17959 (2021).

[73] A. H. Piracha, P. Rath, K. Ganesan, S. Kühn, W. H. Pernice, and S. Prawer, "Scalable fabrication of integrated nanophotonic circuits on arrays of thin single crystal diamond membrane windows," Nano Letters **16**, 3341 (2016).

[74] T. Schröder, M. Walsh, J. Zheng, S. Mouradian, L. Li, G. Malladi, H. Bakhru, M. Lu, A. Stein, M. Heuck, *et al.*, "Scalable fabrication of coupled NV center-photonic crystal cavity systems by self-aligned N ion implantation," Optical Materials Express **7**, 1514 (2017).

[75] M. Cambria, S. Chand, and S. Kolkowitz, "Scalable parallel measurement of individual nitrogen-vacancy centers," arXiv **2408**, 11715 (2024).

[76] P. Spinicelli, A. Dreau, L. Rondin, F. Silva, J. Achard, S. Xavier, S. Bansropun, T. Debuisschert, S. Pezzagna, J. Meijer, *et al.*, "Engineered arrays of nitrogen-vacancy color centers in diamond based on implantation of CN- molecules through nanoapertures," New Journal of Physics **13**, 025014 (2011).

[77] M. Pompili, S. L. Hermans, S. Baier, H. K. Beukers, P. C. Humphreys, R. N. Schouten, R. F. Vermeulen, M. J. Tiggelman, L. dos Santos Martins, B. Dirkse, *et al.*, "Realization of a multinode quantum network of remote solid-state qubits," Science **372**, 259 (2021).

[78] F. Ghani, H. Gojzewski, and H. Riegler, "Nucleation and growth of copper phthalocyanine aggregates deposited from solution on planar surfaces," Applied Surface Science **351**, 969 (2015).

[79] T. Ichii, T. Fukuma, T. Yoda, K. Kobayashi, K. Matsushige, and H. Yamada, "Submolecular-scale investigations on metal-phthalocyanine monolayers by frequency modulation atomic force microscopy," Journal of Applied Physics **107** (2010), 10.1063/1.3284094.

[80] S. Karan and B. Mallik, "Effects of annealing on the morphology and optical property of copper (II) phthalocyanine nanostructured thin films," Solid State Communications **143**, 289 (2007).

[81] P. Popielarski, L. Mosińska, L. Skowronski, R. Szczesny, V. Figà, M. Naparty, and B. Derkowska-Zielinska, "Influence of heat treatment on surface, structural and optical properties of nickel and copper phthalocyanines thin films," International Journal of Molecular Sciences **23**, 11055 (2022).

[82] N. Padma, S. N. Sawant, and S. Sen, "Study on post-deposition annealing influenced contribution of hole and electron trapping to threshold voltage stability in organic field effect transistors," Materials Science in Semiconductor Processing **30**, 18 (2015).

[83] H. J. Wagner, R. O. Loutfy, and C.-K. Hsiao, "Purification and characterization of phthalocyanines," Journal of Materials Science **17**, 2781 (1982).

[84] A. Farag, "Optical absorption studies of copper phthalocyanine thin films," Optics & Laser Technology **39**, 728 (2007).

[85] J. Bennett and D. Ingram, "Paramagnetic resonance in copper phthalocyanine," Nature **175**, 130 (1955).

[86] W. Jiang, X. Wang, Y. Chang, S. Yu, C. Ma, K. Ye, C. Cheng, and G. Du, "Single crystal growth of copper phthalocyanine using exaltation–evaporation growth method," Journal of Crystal Growth **290**, 544 (2006).

[87] F. Weidner, *Paramagnetic electron-spin network*, Bachelor's thesis, University of Stuttgart, Pfaffenwaldring 57, 70569 Stuttgart (2016).

[88] L. M. Pham, N. Bar-Gill, D. Le Sage, C. Belthangady, A. Stacey, M. Markham, D. J. Twitchen, M. D. Lukin, and R. L. Walsworth, "Enhanced metrology using preferential orientation of nitrogen-vacancy centers in diamond," Physical Review B **86** (2012), 10.1103/physrevb.86.121202.

[89] N. Amar, R. Gould, and A. Saleh, "Structural and electrical properties of the α-form of metal-free phthalocyanine (α-H_2Pc) semiconducting thin films," Current Applied Physics **2**, 455 (2002).

[90] A. Hoshino, Y. Takenaka, and H. Miyaji, "Redetermination of the crystal structure of α-copper phthalocyanine grown on KCl," Acta Crystallographica B **59**, 393 (2003).

[91] S. Tokito, J. Sakata, and Y. Taga, "The molecular orientation in copper phthalocyanine thin films deposited on metal film surfaces," Thin Solid Films **256**, 182 (1995).

[92] J. Wang, W. Zhang, J. Zhang, J. You, Y. Li, G. Guo, F. Feng, X. Song, L. Lou, W. Zhu, *et al.*, "Coherence times of precise depth controlled NV centers in diamond," Nanoscale **8**, 5780 (2016).

[93] B. Kasumaj and S. Stoll, "5-and 6-pulse electron spin echo envelope modulation (ESEEM) of multi-nuclear spin systems," Journal of Magnetic Resonance **190**, 233 (2008).

[94] L. Kulik, Y. A. Grishin, S. Dzuba, I. Grigoryev, S. Klyatskaya, S. Vasilevsky, and Y. D. Tsvetkov, "Electron dipole–dipole ESEEM in field-step ELDOR of nitroxide biradicals," Journal of Magnetic Resonance **157**, 61 (2002).

[95] C. A. Meriles, L. Jiang, G. Goldstein, J. S. Hodges, J. Maze, M. D. Lukin, and P. Cappellaro, "Imaging mesoscopic nuclear spin noise with a diamond magnetometer," The Journal of chemical physics **133** (2010).

[96] N. Lambert, E. Giguère, P. Menczel, B. Li, P. Hopf, G. Suárez, M. Gali, J. Lishman, R. Gadhvi, R. Agarwal, *et al.*, "QuTiP 5: The quantum toolbox in python," arXiv **2412**, 04705 (2024).

[97] F. Reinhard, F. Shi, N. Zhao, F. Rempp, B. Naydenov, J. Meijer, L. T. Hall, L. Hollenberg, J. Du, R.-B. Liu, *et al.*, "Tuning a spin bath through the quantum-classical transition," Physical Review Letters **108**, 200402 (2012).

[98] M. Loretz, J. Boss, T. Rosskopf, H. Mamin, D. Rugar, and C. L. Degen, "Spurious harmonic response of multipulse quantum sensing sequences," Physical Review X **5**, 021009 (2015).

[99] A. Laraoui, F. Dolde, C. Burk, F. Reinhard, J. Wrachtrup, and C. A. Meriles, "High-resolution correlation spectroscopy of 13c spins near a nitrogen-vacancy centre in diamond," Nature communications **4**, 1651 (2013).

[100] J. McGuire, H. N. Miras, J. P. Donahue, E. Richards, and S. Sproules, "Ligand radicals as modular organic electron spin qubits," Chemistry–A European Journal **24**, 17598 (2018).

[101] H. Espinós, C. Munuera-Javaloy, I. Panadero, P. Acedo, R. Puebla, J. Casanova, and E. Torrontegui, "Enhancing polarization transfer from nitrogen-vacancy centers to external nuclear spins via dangling bond mediators," Communications Physics **7**, 42 (2024).

[102] A. Tannús and M. Garwood, "Adiabatic pulses," NMR in Biomedicine **10**, 423 (1997).

[103] I. Niemeyer, J. Shim, J. Zhang, D. Suter, T. Taniguchi, T. Teraji, H. Abe, S. Onoda, T. Yamamoto, T. Ohshima, *et al.*, "Broadband excitation by chirped pulses: application to single electron spins in diamond," New Journal of Physics **15**, 033027 (2013).

[104] A. Ramachandran, J. Fraser-Leach, S. O'Neal, D. Deppe, and K. Hall, "Experimental quantification of the robustness of adiabatic rapid passage for quantum state inversion in semiconductor quantum dots," Optics Express **29**, 41766 (2021).

[105] A. Doll, S. Pribitzer, R. Tschaggelar, and G. Jeschke, "Adiabatic and fast passage ultra-wideband inversion in pulsed epr," Journal of Magnetic Resonance **230**, 27 (2013).

[106] M. Garwood and L. DelaBarre, "The return of the frequency sweep: designing adiabatic pulses for contemporary NMR," Journal of Magnetic Resonance **153**, 155 (2001).

[107] D. E. Waddington, T. Boele, E. Rej, D. R. McCamey, N. J. King, T. Gaebel, and D. J. Reilly, "Phase-encoded hyperpolarized nanodiamond for magnetic resonance imaging," Scientific Reports **9**, 5950 (2019).

[108] G. T. Genov, Y. Ben-Shalom, F. Jelezko, A. Retzker, and N. Bar-Gill, "Efficient and robust signal sensing by sequences of adiabatic chirped pulses," Physical Review Research **2**, 033216 (2020).

[109] P. Neumann, N. Mizuochi, F. Rempp, P. Hemmer, H. Watanabe, S. Yamasaki, V. Jacques, T. Gaebel, F. Jelezko, and J. Wrachtrup, "Multipartite entanglement among single spins in diamond," Science **320**, 1326 (2008).

[110] I. Zohar, B. Haylock, Y. Romach, M. J. Arshad, N. Halay, N. Drucker, R. Stöhr, A. Denisenko, Y. Cohen, C. Bonato, *et al.*, "Real-time frequency estimation of a qubit without single-shot-readout," Quantum Science and Technology **8**, 035017 (2023).

[111] A. Y. Kitaev, "Quantum measurements and the Abelian stabilizer problem," arXiv **quant-ph**, 9511026 (1995).

[112] V. Vorobyov, S. Zaiser, N. Abt, J. Meinel, D. Dasari, P. Neumann, and J. Wrachtrup, "Quantum Fourier transform for nanoscale quantum sensing," npj Quantum Information **7**, 124 (2021).

[113] R. Said, D. Berry, and J. Twamley, "Nanoscale magnetometry using a single-spin system in diamond," Physical Review B **83**, 125410 (2011).

[114] B. Higgins, D. Berry, S. Bartlett, M. Mitchell, H. Wiseman, and G. Pryde, "Demonstrating Heisenberg-limited unambiguous phase estimation without adaptive measurements," New Journal of Physics **11**, 073023 (2009).

[115] P. Cappellaro, "Spin-bath narrowing with adaptive parameter estimation," Physical Review A **85**, 030301 (2012).

[116] N. Wiebe and C. Granade, "Efficient Bayesian phase estimation," Physical Review Letters **117**, 010503 (2016).

[117] E. Scerri, E. M. Gauger, and C. Bonato, "Extending qubit coherence by adaptive quantum environment learning," New Journal of Physics **22**, 035002 (2020).

[118] C. Bonato, M. S. Blok, H. T. Dinani, D. W. Berry, M. L. Markham, D. J. Twitchen, and R. Hanson, "Optimized quantum sensing with a single electron spin using real-time adaptive measurements," Nature Nanotechnology **11**, 247 (2016).

[119] T. Joas, S. Schmitt, R. Santagati, A. A. Gentile, C. Bonato, A. Laing, L. P. McGuinness, and F. Jelezko, "Online adaptive quantum characterization of a nuclear spin," npj Quantum Information **7**, 56 (2021).

[120] H. T. Dinani, D. W. Berry, R. Gonzalez, J. R. Maze, and C. Bonato, "Bayesian estimation for quantum sensing in the absence of single-shot detection," Physical Review B **99**, 125413 (2019).

[121] M. J. Arshad, C. Bekker, B. Haylock, K. Skrzypczak, D. White, B. Griffiths, J. Gore, G. W. Morley, P. Salter, J. Smith, *et al.*, "Real-time adaptive estimation of decoherence timescales for a single qubit," Physical Review Applied **21**, 024026 (2024).

[122] R. H. Brown and R. Q. Twiss, "Correlation between photons in two coherent beams of light," Nature **177**, 27 (1956).

[123] J. M. Binder, A. Stark, N. Tomek, J. Scheuer, F. Frank, K. D. Jahnke, C. Müller, S. Schmitt, M. H. Metsch, T. Unden, T. Gehring, A. Huck, U. L. Andersen, L. J. Rogers, and F. Jelezko, "Qudi: A modular python suite for experiment control and data processing," SoftwareX **6**, 85 (2017).

[124] K. J. Brown, E. Chartier, E. M. Sweet, D. A. Hopper, and L. C. Bassett, "Cleaning diamond surfaces using boiling acid treatment in a standard laboratory chemical hood," Journal of Chemical Health & Safety **26**, 40 (2019).

[125] R. Gutzler, W. M. Heckl, and M. Lackinger, "Combination of a Knudsen effusion cell with a quartz crystal microbalance: In situ measurement of molecular evaporation rates with a fully functional deposition source," Review of Scientific Instruments **81**, 015108 (2010).

[126] S. Sundar, L. S. Sharath Chandra, V. K. Sharma, M. K. Chattopadhyay, and S. B. Roy, in *AIP Conference Proceedings*, Vol. 1512, pp. 1092–1093

List of publications

[1] **I. Zohar**, B. Haylock, Y. Romach, M. J. Arshad, N. Halay, N. Druker, R. Stöhr, A. Denisenko, Y. Cohen, C. Bonato, and A. Finkler, "Real-time frequency estimation of a qubit without single-shot-readout," Quantum Sci. Technol. 8, 035017 (2023).

[2] A. Awadallah, **I. Zohar**, and A. Finkler, "Spin-strain coupling in nanodiamonds as a unique cluster identifier. Journal of Applied Physics," J. Appl. Phys 113, 145103 (2023).

[3] J. Kumar, D. Yudilevich, A. Smooha, **I. Zohar**, A. K. Pariari, R. Stöhr, A. Denisenko, M. Hücker, and A. Finkler, "Room temperature relaxometry of single nitrogen-vacancy centers in proximity to $\alpha - RuCl_3$ nanoflakes," Nano Lett. **24**, 4793 (2024).

[4] J. W. Rosenberg, M. Kuffer, **I. Zohar**, R. Stöhr, A. Denisenko, A. Zwick, G. A. Álvarez, and A. Finkler, "Witnessing non-stationary and non-Markovian environments with a quantum sensor," arXiv 2501.05814.

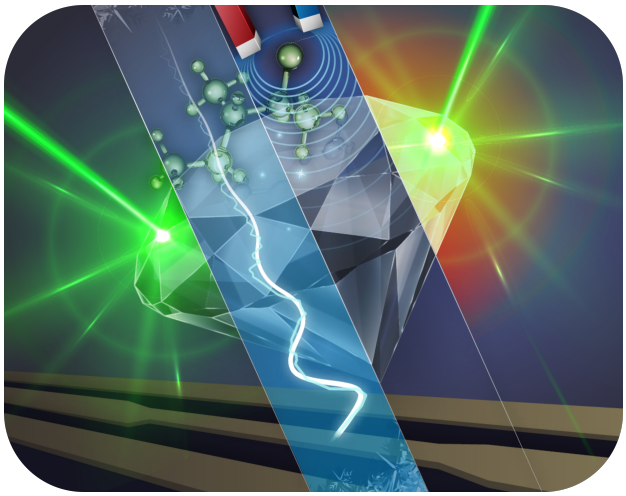

This thesis was typeset using LaTeX, originally developed by Leslie Lamport and based on Donald Knuth's TeX. The body text is set in 11 point Egenolff-Berner Garamond, a revival of Claude Garamont's humanist typeface. A template that can be used to format a PhD thesis with this look and feel has been released under the permissive MIT (X11) license and can be found online at github.com/suchow/Dissertate or from its author, Jordan Suchow, at suchow@post.harvard.edu.

תקציר

פגם ביהלום מסוג חנקן-חור התגלה כחיישן קוונטי רב עוצמה המסוגל לזהות ספינים של אלקטרונים בקנה מידה אטומי. עם זאת, ניצול הפגם כדי לחוש את התכונות המגנטיות המורכבות של סחריר אלקטרוני המצוי במולקולות נותר אתגר משמעותי. יתרה מכך, שילוב מרכזי חנקן-חור עם סחריר אלקטרוני במולקולות לכדי מערכת קוונטית היברידית יכולה להיות טכנולוגיה קוונטית מעניינת. תיזה זו שמה לה למטרה להתמודד עם האתגרים של חישה מגנטית של סחריר אלקטרוני במולקולה בודדת על ידי פיתוח שיטות חדשניות להגברת הרגישות והקוהרנטיות הקוונטית של חישה מבוססת מרכז חנקן-חור.

העבודה פותחת במאמץ המחקרי שנעשה לחישה של נחושת פתלוציאנין, מולקולה עם סחריר אלקטרוני, באמצעות מדידה מגנטית חדשה מבוססת התאמה של מחזורי חישה מסוג "ראמזי" (Ramsey). שיטת המדידה הזו מאפשרת חישה של שדות מגנטים קבועים בזמן תוך הארכת זמן הקוהרנטיות הקוונטית של החיישן מעבר לזמני הקוהרטיות הטיפוסיים שלו T_2^* וT_2, דבר המאפשר רגישות לשדה המושרה מתוך הצימוד של הסחריר האלקטרוני במולקולה והמרכז חנקן-חור.

תוצאות של ניסויים והדמיות מראות את העליונות של שיטת המדידה על פני שיטות קיימות כמו רזוננס-אלקטרון-אלקטרון (DEER), הן מניחות את הבסיס לחישה קוונטית באמצעות מרכז חנקן-חור של סחריר אלקטורני במולקולה בודדת. יתר על כן, חלק מתוצאות הניסויים מראות זמן קוהרנטיות ארוך מהמצופה המנוצל על ידי התאמת המדידה לתדר הספין גרעיני של פחמן, דבר זה מצביע על שימושים נוספים בשיטת המדידה.

העבודה עוסקת גם בשימוש בפולסים אדיאבטים, ביכולת שלהם להגביר את הרגישות והאות שנמדד בחישה של סחרירים אלקטרונים באמצעות DEER. פולסים אדיאבטים בעלי ביצועים טובים יותר מפולסים סטנדרטים בזכות השימוש ברוחב פס רחב על מנת לאפשר אינטראקציה טובה יותר עם הסחריר האלקטורני, דבר המדגיש את הפוטנציאל של הפולסים בחישה קוונטית בפרט ובמחשוב קוונטי בכלל.

לסיום, שיטה להערכת פאזה המבוססת על היסק בייסיאני (Bayesian estimation) בזמן אמת מיושמת על המרכז חנקן-חור, השיטה מאפשר שיפור של הרגישות של החיישן לשדות מגנטים קבועים בזמן תוך מיצוע מדידות חוזרות להגברת האות מהחיישן. הדמיה ממחושבת מראה כיצד יישום השיטה באופן אדפטיבי יכולה להפחית את זמני המדידה תוך שיפור הרגישות, מה שמציג את הפוטנציאל הטמון בלמידת מכונה עבור חישה קוונטית.

יחד, ההתקדמויות הללו מייצגות התקדמות משמעותית לקראת מימוש הפוטנציאל של מרכז חנקן-חור כחיישן למערכות מורכבות כמו סחריר אלקטרוני במולקולות. על ידי שיפור הרגישות והקוהרנטיות תוך התמודדות עם אתגרים מעשיים, עבודה זו סוללת את הדרך ליישומים עתידיים במערכות קוונטיות היברידיות, תקשורת קוונטית ומעבר לכך.